Optimization of a heat-driven thermoacoustic cooler in a looped tube with two stacks

2018.3

Tokyo University of Agriculture and Technology

Graduate School of Bio-Application and System Engineering

Irna Farikhah

Contents

Abstract

When an acoustic wave propagates in a narrow tube, a gas in the tube undergoes thermal interactions with the tube wall. As a result, the acoustical energy converts into thermal energy. Using the energy conversion, a heat-driven thermoacoustic cooler can be constructed. In 2002, Yazaki et. al constructed the cooler that consists of a looped tube, an engine stack, and a cooler stack. When the engine stack is differentially heated, the acoustic wave spontaneously generates. The generated acoustic wave travels along the tube and enters the cooler stack. In the stack, the acoustic power is consumed to pump heat from one side the other side of the cooler stack.

Yazaki et. al reported that the performance of it can be improved when the relative position of the stacks is varied. However, they did not measure the performance of the whole system. They also did not perform the optimization. We consider that the performance of Yazaki's cooler system can be improved by optimizing some important parameters. Therefore, in this investigation, we have optimized the system numerically. We chose five parameters to be optimized; relative position between the stacks, radius of the engine stack, radius of the cooler stack, porosity of the engine stack, and porosity of the cooler stack.

For the numerical optimization, we have used the linier thermoacoustic theory proposed by Rott. In this calculation, the momentum and continuity equations in the Rott's theory were modified into the transfer matrices. The used transfer matrices were validated using the experimental results. It was found that the transfer matrices used for the calculation has a good agreement with the experimental results. Then, we used the transfer matrices to calculate the performance of Yazaki's cooler. It was found that the optimum relative position, radius of the engine stack, radius of the cooler stack, porosity of the engine and porosity of the cooler are 0.54, 0.96, 1.06 and 1.3, respectively. In addition, it was found that the numerical optimization of the parameters makes the whole cooler system to be 0.24 of the upper limit value.

Based on the optimization of the radius, we found that the optimum radius of the stacks is 0.070 mm for engine stack and 0.078 mm for the cooler stack. In the real condition, the stacks made from stacked-screens having non-uniform flow path will be used. However, in the calculation we used the model of the stacks having uniform flow path. Therefore, re-calculation with the optimized parameter using new method which non-uniform flow path in the stacked screens can be treated. Using the new method, it was found that the whole efficiency of the cooler system is decreased from 0.24 to 0.22 of the upper limit value.

Chapter 1

Introduction

When an acoustic wave propagates in a narrow tube, a gas in the tube takes thermal interactions with the tube wall. As a result of these thermal interactions, the energy conversion between acoustical power and thermal power takes place. By using the energy conversion, we can construct a “thermoacoustic” engine and a “thermoacoustic” cooler.

1.1. The thermoacoustic history

The thermoacoustic history began last 240 years ago. In 1777, Higgins recorded that sound excitation is produced when the hot side of the tube is heated [1]. The phenomenon is called as ”singing flame”[see Fig. 1.1]. In 1859, Rijke constructed an experiment [see Fig. 1.2] [2]. The experimental device consists of an open tube, wire meshes and a burner. The wire meshes are installed inside the tube. Then, one side of the wire meshes is heated by the burner. After that, the sound is generated [3]. He found that when the tube is held at a vertical position inside the open tube and when the metal mesh is positioned in the lower half of the tube, a sound is produced. He noted that the sound is louder when the mesh is placed at the quarter position of the tube from the bottom. Many researchers reviewed Sondhauss and Rijke experimental investigations [4, 5]. Another thermoacoustic investigation was conducted by Julius Sondhauss in 1850. When a hot glass bulb is attached to the end of a tube, a sound is produced [see Fig. 1.3] [6].

The experimental observation was succeeded to be investigated by Sondhauss and Rijke. However, they could not elucidated their observations. In 1868, the derivation of equation of thermoacoustic oscillations about thermal attenuation of sound at the constant temperature was investigated quantitatively by Kirchhoff [7]. In 1887, Sondhauss observations can be explained by Rayleigh [8]. He noticed that:

''*If heat be given to the air at the moment of greatest condensation or taken from it at the moment of greatest rarefaction, the vibration is encouraged".*

Liquid helium was used as working fluid in Sondhauss tube by Taconic and Beenakker In 1949 [9]. It was found that spontaneous gas oscillations are excited when a temperature gradient is imposed along the glass tube. It called as ''Taconic oscillations''.

1.1.1. Thermoacoustic engine

There are many applications of thermoacoustic technology such as a thermoacoustic engine, a thermoacoustic cooler and a thermoacoustic-electric generator. In 1988, Swift demonstrated a thermoacoustic engine [10]. In the demonstration, he used a stainless-steel stack. The stack is installed in a straight tube having two ends. One end is closed and the other is opened. In his demonstration, the tube contains 1-atm air. The air acts as a working fluid. The result showed that the acoustic power is produced when the critical heating temperature is imposed to the hot side of the stack. He was also investigated a large thermoacoustic engine [11]. The diameter of the engine is 13 cm and the working fluid is helium at 1.38 MPa. The efficiency of the engine reaches 0.13 of Carnot efficiency. However, the heating temperature of the engine is high at 700 ℃.

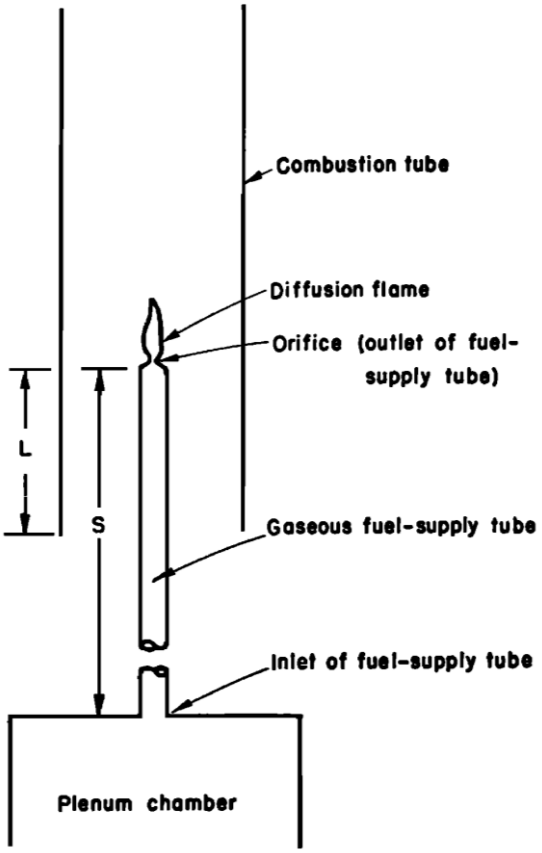

Figure 1.1 One form of singing-flame apparatus [1]

Those engines have low efficiency because irreversibility processes take place in the stack which the standing wave field is excited. Therefore, the travelling wave field is important to be employed for reversible processes excitation.

A device was designed by Caperley [12] to investigate the travelling wave principle. He realized that a travelling wave propagating through a regenerator undergoes a thermodynamic cycle similar to the Stirling cycle. However, in his investigation, he used low amplification of acoustic power due to the low acoustic impedance of the working gas, which causes large viscous loss. To increase the acoustic impedance, Backhauss and Swift [13] constructed a thermoacoustic engine which is installed in a

looped tube having a resonator.

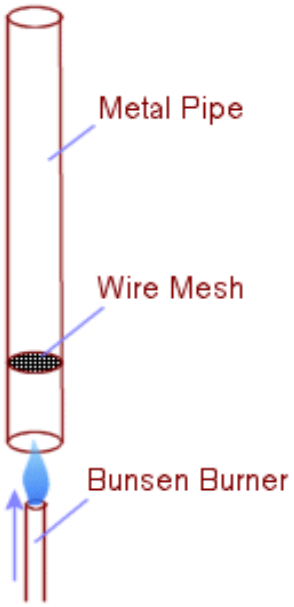

Figure 1.2. Rijke tube [2]

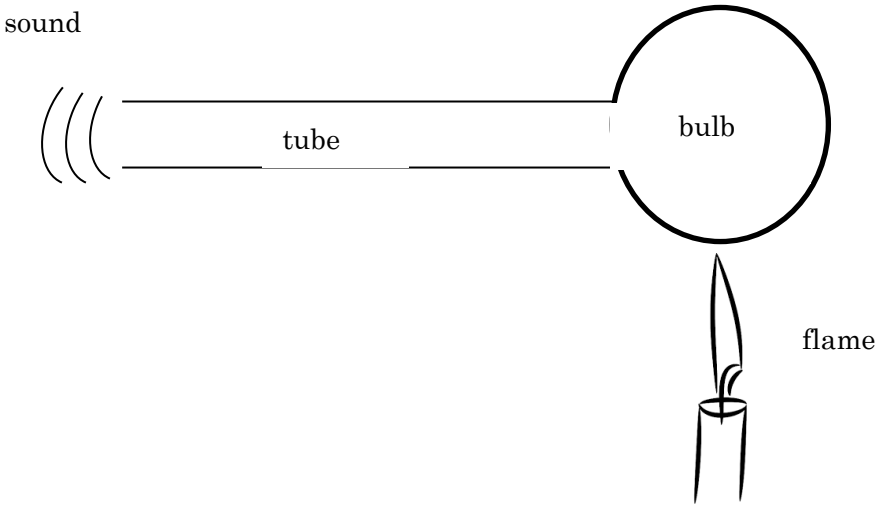

Figure 1.3. Soundhauss tube

The resonator was employed to create high impedance in the regenerator. As a result, it was found that the efficiency of the engine is 0.41 of Carnot efficiency. This

efficiency is comparable to the conventional combustion engines. However, the heating temperature is high at 725 ℃. Moreover, the acoustic power dissipation occurs in the resonator.

In 1997, Yazaki et. al [14] constructed a thermoacoustic engine. Their results showed a comparison between the travelling wave in a looped tube and the standing wave in a resonator tube. It was found that the gas undergoes excellent thermal contact in the looped tube. On the other hand, the gas undergoes imperfect thermal contact in the resonator tube. As a result, the onset temperature of the engine in the looped tube is lower than that in the resonator.

1.1.2 Thermoacoustic cooler

Another application of thermoacoustic is the cooler. In 1986, Hofler constructed a thermoacoustic cooler. He measured the efficiency of the cooler. It was found that the efficiency of the cooler is 0.12 of the upper limit value [15].

The Space Thermoacoustic Refrigerator (STAR), was designed and built by a team at the Naval Postgraduate School led by Garret [16]. This thermoacoustic refrigerator uses acoustic power to pump heat from a low temperature source to a high temperature sink. It was found that the efficiency of the cooler is 0.16 of the upper limit value.

In 2002, Tijani et. al [17] investigated a thermoacoustic cooler using a straight tube. The acoustic power produced by an electrodynamic loudspeaker. Then, the acoustic wave travels along the tube and enter the cooler stack. In the stack, there is thermal interaction between acoustic wave and the surface of the stack. As a result, heat pumping process takes place [18]. In their investigation, some parameters were optimized. They are position, length of the stack, and diameter ratio between the stack

and the tube. Tijani et. al found that the optimum position of the stack is 6 % of the tube length from the driver. The optimum length of the stack is less than 10 % of the tube length and the optimum diameter ratio is 0.5. As a result, it was found that COP reaches 1.8.

In 2004, a thermoacoustic cooler driven by loudspeaker for making ice cream was constructed by Garret et.al [19]. The cooling temperature reached about 248 K. It was found that the efficiency of the cooler is 0.18 of the upper limit value.

In 2009, an optimisation of a cooler driven by an electrical loudspeaker was performed by Ueda et. al [20]. Position, flow-channel radius, and length of the regenerator were optimized. They found that the best regenerator position is 0.8 of the tube length and the optimum flow-channel radius is 0.19 of the thermal penetration depth. In addition, the optimum regenerator length is 1/1000 of the wave length. Their results showed that the optimum position and radius of the regenerator have a huge impact on the COP. However, the effect of the regenerator length has a small impact on the COP.

A thermoacoustic cooler driven by an electrodynamic loudspeaker was constructed by Bassem et. al [21]. The construction consists of an engine regenerator, a looped tube and a resonator tube. The engine regenerator is installed inside the looped tube. The result showed that 0.2 of Carnot COP is obtained when the cooling temperature T_c is -8 ℃. In this investigation, they defined that the input acoustic power $\dot{W}_{in}$ is set in the junction of the branch tube. It indicates that COP would be lower if the definition of $\dot{W}_{in}$ is set at the loudspeaker. It implies that the existence of the resonator causes an additional dissipation.

1.1.3 A heat-driven thermoacoustic cooler

Recently, the research efforts in thermoacoustic have moved away from the use of electrodynamic loudspeakers as a source of the acoustic power to drive the cooler. Therefore, it is useful to make a couple of the thermoacoustic engine and cooler in a system. Furthermore, employing the thermoacoustic engine as a power source is attracting idea due to the possibility of utilization of waste and solar heat.

Hofler and Adeff [22] built a thermoacoustic cooler driven by a thermoacoustic engine. This engine is heated by the solar heat at 475 ℃. The cooler system could produce 2.5 W of cooling power at $T_c = 5$ ℃.

A couple of the thermoacoustic engine and cooler in a straight tube was investigated by Swift [10]. In his device, an engine stack is located near the closed end of the tube and a cooler stack is positioned next to the engine. This stack cooler is connected to a smaller tube. The tube is connected to a spherical bulb. It was found that the cooling temperature at -11 ℃ in the cooler stack is produced when a 380-W heating power at 400 ℃ is imposed to the hot side of the engine stack. This result is good for understanding the thermoacoustic phenomena. However, the performance of the stack is still low due to the use of the stainless steel as a stack material. This material has high value of thermal conductivity. Hence, the stacks suffer from dissipation.

Yazaki et. al [23] constructed a thermoacoustic cooler driven by a thermoacoustic engine in 2002. The system is consists of two stacks installed in a looped tube. The first stack acts as an engine, while the other stack acts as a cooler. Their results showed that the low cooling temperature is obtained. Furthermore, they reported that a good performance of the cooler would be obtained if the cooler is adjusted in a precise position. However, there was not detail elucidation of the performance.

A single-stage thermoacoustic cooler driven by an engine was built by T. Jin et. al [24]. The cross sectional area of the regenerators is larger than that of the looped tube. Their result showed that the total efficiency is 0.17.

In 2004, a heat-driven thermoacoustic cooler was investigated by Ueda et.al [25]. A combination of a looped tube and a resonator tube is constructed. The stacks are inserted inside the looped tube. The working fluid is the mixture gas of helium and argon. It was found that the total COP of the system is 0.05.

A thermoacoustic cooler driven by a thermoacoustic engine was constructed by Miwa et.al [26]. Their configuration consists of two looped tubes connected by a branch tube. There are two stacks in the cooler system. The first stack is put at the first looped tube. The stack acts as a thermoacoustic engine. The second stack is put at the second looped tube. The stack acts as a thermoacoustic cooler. They found that the efficiency of the engine is 0.06 of Carnot'efficiency and the efficiency of the cooler is 0.048 of Carnot's COP. In addition, the efficiency of the tube is 0.167. As a result, the total efficiency of the cooler system becomes 0.00048.

A heat-driven thermoacoustic cooler was also built by Hasegawa et.al in 2013 [27]. This configuration is similar to that of Miwa's experimental device. Hasegawa's device consists of four stacks installed in the two different looped tubes. Three stacks are employed as engines. The engines are located in the first looped tube. The other stack is employed as a cooler. The cooler is located in the second looped tube. At $T_H/T_A = 1.38$ and $T_C/T_A = 0.9$, their result showed that the total efficiency of the system cooler is 0.09 of the upper limit value.

1.2 Motivation and objective

Thermoacoustic devices have many potential advantages over the conventional energy-conversion system. Firstly, the absence of the mechanical moving parts. This makes the systems virtually maintenance-free and highly reliable. Secondly, thermoacoustic devices usually use inert gases as a working fluid such as helium, nitrogen, and argon. This makes them environmentally friendly. Thirdly, the thermoacoustic technology is beneficial for waste heat recovery. Therefore, we can consider that thermoacoustic systems are competitive technology. In this study, we focus on a thermoacoustic cooler technology.

Based on the description in sec. 1.1, the total efficiency of the heat-driven thermoacoustic cooler is limited at 0.17 of Carnot efficiency [24]. Therefore, it is important to improve the efficiency. According to the previous studies, it was known that the problem of the inefficient systems occur in the engine, cooler and looped tube. Hence, it is essential to increase the efficiency.

Thus, a new cooler system must be introduced to overcome the problems. First, it is important to consider the configuration type of the cooler system. In the case of straight tube, irreversibility process would occur in the regenerator. It makes the engine efficiency is low. On the other hand, the couple of looped tube and resonator has disadvantages. Dissipation of the acoustic power would occur in the resonator. In addition, the acoustic field distribution would not change considerably due to the fix value of velocity in the resonator closed end. Hence, it is difficult to make considerable improvement of the performance. There is another type of the cooler system. That is

double looped tubes with a connecting tube. However, this type suffers from dissipation inside these tubes. Thus, we consider that a single looped tube having two regenerators is expected to be the best configuration type. In addition, according to the investigation conducted by Ueda et.al [25], there is a high possibility to adjust the acoustic field distribution inside a looped tube. The adjustment can be done by changing the geometry of the regenerator such as flow-channel radius. In order to obtain better performance in the looped tube type, an optimisation of the system is needed. Therefore, we focus on the optimisation of a heat-driven cooler system in a looped tube.

1.3 Scope of the thesis

As mentioned above, there is high possibility to get high efficiency using looped tube with two stacks by optimization. Therefore, we decide to perform the optimization of the system. There are 7 chapters in this thesis. The first chapter is introduction. Here, we introduce the reason why we study on the optimization of this thermoacoustic system. Then, in the second chapter we provide and describe the thermoacoustic theory mathematically and physically. In the third chapter, we focus on the how to calculate the transfer matrices. Here, we show the transfer matrix with temperature gradient and without temperature gradient. In chapter 4, we show the validation of transfer matrices using some experimental results obtained by researchers. There are three different validations. The first is validation using straight tube having one stack. In this case, we use electrodynamic loudspeaker as the source of acoustic power. The second is validation using a cooler driven by an engine in a straight tube, and the last is validation

using a cooler driven by an engine in a looped tube. In the chapter 5, we perform the optimization. We selected five parameters to be optimized: relative position of the cooler stack, radius of engine and cooler stacks, and porosity of engine and cooler stacks. In the chapter 6, we re-calculate the optimized value with new mwthod. In the last chapter, we make the conclusions of all previous chapters.

Chapter 2

Thermoacoustic Theory

Thermoacoustic phenomena relates to fluid dynamics. In the fluid dynamics, we consider that the fluid contents a great number of molecules. The states of moving fluid is affected by the distribution of the pressure P, density ρ, and cross-sectional means of oscillatory velocity U. There are some fundamental equations of fluid dynamic; namely conservation of mass (Continuity), Navier-Stokes (Momentum), and general equation of heat transfer for fluid [28].

2.1 Fundamental Equation

To begin with, the equation of conservation of mass (Continuity), Navier-Stokes (momentum), and the general equation of heat transfer for fluid are provided as follow [28].

$$\partial\rho/\partial t + \rho\nabla.U + U.\nabla\rho = 0 \tag{2.1}$$

$$\rho\left[\frac{\partial U}{\partial t} + (U.\nabla)U\right] = -\nabla P + \mu\Delta U + \left(\zeta + \frac{1}{3}\eta\right)\nabla\nabla.U \tag{2.2}$$

$$\rho T\left(\frac{\partial s}{\partial t} + U.\nabla s\right) = (\sigma'.\nabla).U + \nabla.(k\nabla T) \tag{2.3}$$

Since it is considered as incompressible flow, so the second term of eq. 2.1 and the last term of eq.2.2 vanish, and they become

$$\partial\rho/\partial t + U.\nabla\rho = 0 \tag{2.4}$$

and

$$\rho\left[\frac{\partial U}{\partial t} + (U.\nabla)U\right] = -\nabla P + \mu\Delta U \tag{2.5}$$

respectively. Here, ρ, s, T are density, entropy and temperature, respectively. σ' is the viscous stress tensor.

In this theory, we consider about steady-laminar flow through a circular tube with radius r_{tube} . It should be noted that the linearization of all equations is used [29]: (1) The radial gradient of the acoustic pressure is neglected throughout the tube. (2) The radial variations of the average temperature and the viscosity are neglected. (3) The axial heat conduction in the acoustic wave and friction due to the axial gradients are ignored. (4) r_{tube} is much smaller than the length of the tube L_{tube}. (5) The time-variation is assumed to be given by the factor $e^{i\omega t}$ multiplying ρ, U and s, so that the equations will be written down using $\partial/\partial t = i\omega$. Here, for the simplification, the mean values of pressure, temperature and density will be indicated by the subscript *m*; the mean pressure P_m is a constant [29].

The theory refers to the one quantitative one dimensional thermoacoustic prediction tools and formulations developed over the last forty years [29-33].

The continuity equation becomes:

$$i\omega\rho + U\frac{d\rho_m}{dx} = 0 \tag{2.6}$$

and the axial momentum equation has the form

$$i\omega\rho_m U = -\frac{dP}{dx} + \mu\frac{1}{r}\frac{\partial}{\partial r}\left(r\frac{\partial U}{\partial r}\right) \tag{2.7}$$

where μ is the dynamic viscosity. At the wall, $U = 0$. The energy equation is

$$\rho_m c_p\left(i\omega T + U\frac{dT_m}{dx}\right) - i\omega P = \frac{\mu c_p}{\sigma}\frac{1}{r}\frac{\partial}{\partial r}\left(r\frac{\partial T}{\partial r}\right) \tag{2.8}$$

Here, we assume that the fluid has zero viscosity, so the solution of Eq. 2.8 is

$$T = \left(\frac{1}{\rho_m c_p}P - \frac{\nabla T_m}{\omega}U\right)\left(1 - e^{-(1+i)r/\delta_k}\right) \tag{2.9}$$

Equation 2.9 implies that the fluid far from plate, $r \gg \delta_k$, makes negligible thermal

contact with the plate; in that case,

$$T \sim \left(\frac{1}{\rho_m c_p}\right) P - \left(\frac{\nabla T_m}{\omega}\right) U \tag{2.10}$$

The first term here is simply due to the adiabatic compressions and expansions of the fluid. The second term comes from the mean-temperature gradient in the fluid; as the fluid oscillates along x with displacement amplitude U/ω, the temperature at a given point in space oscillates by an amount $\nabla T_m U/\omega$ [see Fig. 2.2 and 2.3]. If eq. 2.10 is zero, so we can find a critical mean-temperature gradient. The critical temperature gradient is important because it determines a stack, which is arranged from some circular tubes, works as an engine or a cooler. The critical mean-temperature gradient can be expressed as

$$\nabla T_{crit} = \frac{|P|/\rho_m c_p}{|U|/\omega} \tag{2.11}$$

Equation 2.7 can be solved as

$$U = \frac{i}{\omega \rho_m}[1 - \chi_v]\frac{dP}{dx} \tag{2.12}$$

The geometry of the channel and gas properties determine the thermoacoustic function χ_v. Eq. 2.12 can be expressed as

$$dP = -\frac{i\omega\rho_m}{1-\chi_v} U\, dx \tag{2.13}$$

Subsequently, after re-organization, eqs. 2.6 and 2.8 become

$$dU = -\frac{i\omega\rho_m dx}{\gamma P_m}[1 + (\gamma - 1)\chi_\alpha]P + \frac{(\chi_\alpha - \chi_v)}{(1-\chi_v)(1-\sigma)}\frac{dT_m}{T_m}U \tag{2.14}$$

The thermoacoustic functions χ_v and χ_α can be expressed as follows

$$\chi_v = \frac{2J_1[(i-1)\, r/\delta_v]}{J_0[(i-1)\, r/\delta_v](i-1)\, r/\delta_v} \tag{2.15}$$

$$\chi_\alpha = \frac{2J_1[(i-1)\, r/\delta_\alpha]}{J_0[(i-1)\, r/\delta_\alpha](i-1)\, r/\delta_\alpha} \tag{2.16}$$

where $J_{0,1}$ is the Bessel function and δ_v and δ_α are the viscous and thermal

penetration depth, respectively. δ_α is defined as the thickness of the layerof gas where heat can diffuse through the gas during a time $1/\omega$, whereas δ_ν is defined as the thickness of the layer where viscosity affect is effective near the boundaries. c_p is the isobaric heat capacity per unit mass.

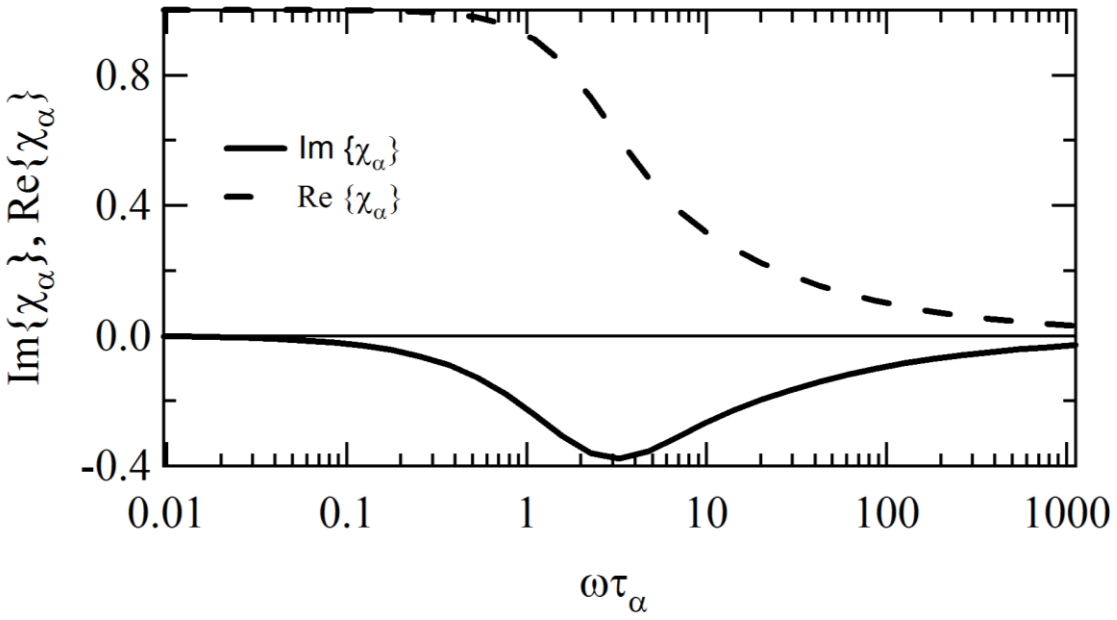

Fig. 2.1 χ_α for circular cylinder; horizontal axis is $\omega\tau_\alpha$ [21]

Figure 2.1 shows χ_α as a function of $\omega\tau_\alpha = r^2/\delta_\alpha^2$. For small $\omega\tau_\alpha$, $Re(\chi_\alpha)$ is large and thus the entropy exchange is large. For large $\omega\tau_\alpha$, $Re(\chi_\alpha)$ is small and thus entropy exchange is small. For intermediate $\omega\tau_\alpha$, $Im(\chi_\alpha)$ shows a valley: irreversibility due to finite thermal diffusivity is large in this region.

2.2. Acoustic power

Eqs. 2.13 and 2.14 yields acoustic field. Thus, acoustic intensity I can be expressed as [34]

$$I = \frac{\omega}{2\pi} \oint PU\, dt \tag{2.17}$$

$$I = \frac{\omega}{2\pi} \oint Re\left[Pe^{i\omega t}\right] Re\left[Ue^{i\omega t}\right] dt = \frac{1}{2} Re\left[P\tilde{U}\right] \tag{2.18}$$

In order to understand thermoacoustic devices, it is necessary to elucidate the power associated with acoustic wave propagation [35]. This is because an acoustic wave causes pressure, density, and temperature changes in thermoacoustic devices, and these are indispensable for energy conversion between heat and work. Then, by multiplying with the cross-sectional area *A* of the tube, acoustic power $\dot{W}$ can be obtained as follow

$$\dot{W} = IA = \frac{1}{2} Re\left[P\tilde{U}\right] A \tag{2.19}$$

When the temperature gradient exists $dT_m/dx \neq 0$, the acoustic power per unit length can be expressed as

$$\frac{d\dot{W}}{dx} = \frac{1}{2} Re\left[\tilde{U}\frac{dP}{dx} + \tilde{P}\frac{dU}{dx}\right] A \tag{2.20}$$

The momentum equation can be expressed as [34]

$$dP = -(i\omega l\, dx + r_v\, dx)U \tag{2.21}$$

$$l = \rho_m \frac{1 - Re[\chi_v]}{|1 - \chi_v|^2} \tag{2.22}$$

$$r_v = \omega \rho_m \frac{Im[-\chi_v]}{|1 - \chi_v|^2} \tag{2.23}$$

and the Continuity equation can be expressed as [34]

$$dU = -\left(i\omega c\, dx + \frac{1}{r_k} dx\right) P + g\, dx\, U \tag{2.24}$$

Here, g can be expressed

$$g = \frac{(\chi_\alpha - \chi_v)}{(1-\chi_v)(1-\sigma)} \frac{1}{T_m} \frac{dT_m}{dx} \tag{2.25}$$

and c and r_k can be written as follows:

$$c = \frac{1}{\gamma p_m}(1 + [\gamma - 1]Re[\chi_\alpha]) \tag{2.26}$$

$$r_k = \frac{\gamma}{\gamma - 1} \frac{P_m}{\omega\, Im[-\chi_\alpha]} \tag{2.27}$$

γ denotes ratio of isobaric to isochoric specific heat.

Substituting eqs. 2.21 and 2.24 into eq. 2.20 yields

$$\frac{d\dot{W}}{dx} = -A\frac{r_v}{2}|U|^2 - A\frac{1}{2r_k}|P|^2 + A\frac{1}{2}Re[g\tilde{P}U] \tag{2.28}$$

The first two terms in Eq. (2.28) are always negative. The first term gives the viscous dissipation of sound and the second term gives the thermal-relaxation dissipation. The third term, which can have either sign, is of the greatest interest in thermoacoustic engines and coolers. This term can be called the source / sink term because it can either produce or consume acoustic power and which exists only if $dT_m/dx \neq 0$. If we assume that the viscosity is zero, so the third term becomes

$$\frac{1}{2}Re[g\tilde{P}U]A = \frac{1}{2}\frac{1}{T_m}\frac{dT_m}{dx}Re[\tilde{P}U]Re[\chi_\alpha]A + \frac{1}{2}\frac{1}{T_m}\frac{dT_m}{dx}Im[\tilde{P}U]Im[-\chi_\alpha]A \tag{2.29}$$

$$\frac{1}{2}Re[g\tilde{P}U] = \frac{1}{T_m}\frac{dT_m}{dx}\dot{W}Re[\chi_\alpha] + \frac{1}{2}\frac{1}{T_m}\frac{dT_m}{dx}Im[\tilde{P}U]Im[-\chi_\alpha]A \tag{2.30}$$

Eq. 2.30 shows that $Re[\chi_\alpha]$ is important for acoustic power in travelling-wave engines and coolers, in which $Re[\tilde{P}U]$ is large, while $Im[-\chi_\alpha]$ is important for acoustic power in standing-wave engines and coolers, in which $Im\left[\widetilde{PU}\right]$ is large.

2.2.1. Acoustic power with zero viscosity

In the case of standing wave engine or cooler, the first term in Eq. (2.29) or (2.30) is zero for standing wave phasing. To make the most of the second term in Eq. (2.29) or (2.30), $Im\,[-\chi_\alpha]$ should be as large as possible. Examination of Fig. 2.1 shows that this is accomplished at $r{\sim}\delta_k$, where $Im[-\chi_\alpha]{\sim}0.4$. Equation (2.27) shows that r_k cannot be neglected, so the source/sink term and the thermal relaxation term in Eq. 2.28 should be considered together. Neglecting viscosity, eqs. (2.29), (2.30), and (2.27) generate

$$\frac{d\dot{W}}{dx} = -\frac{1}{2}|P|^2\frac{(\gamma-1)\omega A\, Im[-\chi_\alpha]}{\gamma P_m} + \frac{1}{2}Im[\tilde{P}U]A\frac{1}{T_m}\frac{dT_m}{dx}Im[-\chi_\alpha] \qquad 2.31$$

Using Eq. (2.11) yields

$$\frac{d\dot{W}}{dx} = \frac{1}{2}|P|^2\omega A\frac{\gamma-1}{\gamma P_m}Im[-\chi_\alpha]\left(\frac{dT_m/dx}{\nabla T_{crit}} - 1\right) \qquad 2.32$$

Here, c_p is

$$c_p = \frac{\gamma}{\gamma-1}\frac{P_m}{\rho_m T_m} \qquad 2.33$$

The situation where $dT_m/dx = \nabla T_{crit}$, for which Eq. (2.32) suggest that acoustic power is neither produced nor absorbed. When $dT_m/dx > \nabla T_{crit}$, the temperature gradient is larger [See Fig. 2.2 a]. It indicates that the acoustic power is produced. On the contrary, when $dT_m/dx < \nabla T_{crit}$, the temperature gradient is smaller [See Fig. 2.2 b]. It implies that the acoustic power is absorbed. According to eq. (2.11), at the critical temperature gradient, $\nabla T_m = \nabla T_{crit} = T_m\beta\omega P/\rho_m c_p U$; there, the temperature change along the plate $2\nabla T_m U/\omega$ $(= 2x\nabla T_m)$ that the parcel sees just matches the parcel's temperature change due to adiabatic compression and expansion $2P/\rho_m c_p$ and no heat flows between the parcel and the plate. It occurs at steps 1 and 3 in the engine and cooler [See Fig. 2.2].

Here, the work flow per unit volume is denoted as $\dot{w}$. The work dw [see Fig. 2.2] done by a differential volume of fluid dV as it expands from $dx\,dy\,dz$ to $dx\,dy\,dz + dV$ is $p\,dV$. Hence the acoustic power per unit volume is

$$\dot{w} = \frac{dw}{dx\,dy\,dz\,dt} = \frac{d\dot{W}}{dV} = \frac{d\dot{W}}{A\,dx} = \frac{1}{2}|P|^2\omega\frac{\gamma-1}{\gamma P_m}Im[-\chi_\alpha]\left(\frac{dT_m/dx}{\nabla T_{crit}} - 1\right) \qquad 2.34$$

Equation 2.34 shows that if $dT_m/dx > \nabla T_{crit}$ the acoustic power is positive, so the work is produced. This is the situation for an engine. However, if $dT_m/dx < \nabla T_{crit}$ the acoustic power is negative, so the work is absorbed to cause uphill heat flux. This is the situation for a cooler.

In step 2 of the engine, the fluid parcel experiences thermal expansion at high pressure, and in step 4 of the engine the fluid parcel experiences thermal contraction at low pressure**.** Therefore, work $dw - dw'$ is done by it. On the contrary, in the step 2 of the cooler the fluid parcel experiences contraction at high pressure, and in step 4 of the cooler the fluid parcel experiences expansion at low pressure. Hence, work $dw - dw'$ is done on it **[see Fig.2.2]**.

Equation 2.31 can be written as follow

$$\frac{d\dot{W}}{dx} = -\frac{1}{2}|P|^2\frac{(\gamma-1)\omega A\,Im[-\chi_\alpha]A}{\gamma P_m} + \frac{A}{2}|P||U|sin\,\theta\,\frac{1}{T_m}\frac{dT_m}{dx}Im[-\chi_\alpha] \qquad 2.35$$

As we can see in eq. 2.35, the time delay (phase difference) θ between P and U exists. When $\theta = 0°$, there is no production or absorption of acoustic power. However, when $\theta = 90°$, the production or absorption of acoustic power is high.

In the case of travelling wave engine or cooler, the second term in Eq. (2.29) or (2.30) is zero for travelling wave phasing. To make the most of the second term in Eq. (2.29) or (2.30), $Re\,[\chi_\alpha]$ should be as large as possible. Examination of Fig. 2.1 shows that this is accomplished at $r \ll \delta_k$, where $Re[\chi_\alpha]\sim1$ and $Im[-\chi_\alpha]\sim0$. Equation

(2.27) shows that r_k cannot be neglected, so the source/sink term and the thermal relaxation term in Eq. 2.28 should be considered together. Neglecting viscosity, eqs. (2.29), (2.30), and (2.27) generate

$$\frac{d\dot{W}}{dx} = -\frac{1}{2}|P|^2 \frac{(\gamma-1)\omega A\, Im[-\chi_\alpha]}{\gamma P_m} + \frac{A}{2} Re[\tilde{P}U] \frac{1}{T_m} \frac{dT_m}{dx} Re[\chi_\alpha] \qquad 2.36$$

Using Eq. (2.11) yields

$$\frac{d\dot{W}}{dx} = \frac{1}{2}|P|^2 \omega A \frac{\gamma-1}{\gamma P_m} \left(\frac{dT_m/dx}{\nabla T_{crit}} \right) \qquad 2.37$$

When $dT_m/dx > \nabla T_{crit}$, the temperature gradient is larger [See Fig. 2.3]. It indicates that the acoustic power is produced. On the contrary, when $dT_m/dx < \nabla T_{crit}$, the temperature gradient is smaller [See Fig. 2.3]. It implies that the acoustic power is absorbed. According to eq. (2.11), at the critical temperature gradient, $\nabla T_m = \nabla T_{crit} = T_m \beta \omega P / \rho_m c_p U$; there, the temperature change along the plate $2\nabla T_m U/\omega$ $(= 2x\nabla T_m)$ that the parcel sees just matches the parcel's temperature change due to compression and expansion $2P/\rho_m c_p$ and no heat flows between the parcel and the plate. It occurs at steps 1 and 3 in the engine and cooler [See Fig. 2.3].

Here, the work flow per unit volume is denoted as $\dot{w}$. The work dw [see Fig. 2.3] done by a differential volume of fluid dV as it expands from $dx\, dy\, dz$ to $dx\, dy\, dz + dV$ is $p\, dV$. Hence the acoustic power per unit volume is

$$\dot{w} = \frac{dw}{dx\, dy\, dz\, dt} = \frac{d\dot{W}}{dV} = \frac{d\dot{W}}{A\, dx} = \frac{1}{2}|P|^2 \omega \frac{\gamma-1}{\gamma P_m} \left(\frac{dT_m/dx}{\nabla T_{crit}} \right) \qquad 2.38$$

Equation 2.35 shows that if $dT_m/dx > \nabla T_{crit}$, so the work is produced. This is the situation for an engine. However, if $dT_m/dx < \nabla T_{crit,}$ so the work is absorbed. This is the situation for a cooler.

In step 2 of the engine the fluid parcel experiences thermal expansion at high pressure, and in step 4 of the engine the fluid parcel experiences thermal contraction at

low pressure**.** Therefore, work $dw - dw'$ is done by it. On the contrary, in the step 2 of the cooler the fluid parcel experiences contraction at high pressure, and in step 4 of the cooler the fluid parcel experiences expansion at low pressure. Hence, work $dw - dw'$ is done on it [see Fig.2.3].

Equation 2.31 can be written as follow

$$\frac{d\dot{W}}{dx} = -\frac{1}{2}|P|^2 \frac{(\gamma-1)\omega A\, Im[-\chi_\alpha]}{\gamma P_m} + \frac{A}{2}|P||U|cos\,\theta\, \frac{1}{T_m}\frac{dT_m}{dx} Re[\chi_\alpha] \qquad 2.39$$

As we can see in eq. 2.39, the time delay (phase difference) θ between P and U exists. When $\theta = 90°$, there is no production or absorption of acoustic power. However, when $\theta = 0°$, the production or absorption of acoustic power is high.

According to eq. (2.28), acoustic power with zero viscosity (not pure travelling wave nor standing wave) can be written as follow

$$d\dot{W}_p = -\frac{1}{2}|P|^2 \frac{(\gamma-1)\omega A\, Im[-\chi_\alpha]}{\gamma P_m} dx + \frac{1}{2}\frac{1}{T_m}\nabla T_m\, Re[\tilde{P}U]Re[\chi_\alpha]dx \qquad 2.40$$
$$+ \frac{1}{2}\frac{1}{T_m}\nabla T_m\, Im[\tilde{P}U]Im[-\chi_\alpha]dx$$

where x is the length of the stack. The second term shows the thermal-relaxation dissipation, $d\dot{W}_p$, and the second and the third terms shows the acoustic power production or absorption due to travelling wave $d\dot{W}_{progg}$ and standing wave $d\dot{W}_{stand}$, respectively. Those can be re-written as follows [34]:

$$d\dot{W}_P = -\frac{1}{2}|P|^2 \frac{(\gamma-1)\omega A\, Im[-\chi_\alpha]}{\gamma P_m} dx \qquad 2.41$$

$$d\dot{W}_{prog} = \frac{A}{2}\frac{1}{T_m}\nabla T_m\, Re[\tilde{P}U]Re[\chi_\alpha]dx \qquad 2.42$$

$$d\dot{W}_{stand} = -\frac{A}{2}\frac{1}{T_m}\nabla T_m\, Im[\tilde{P}U]Im[-\chi_\alpha]dx \qquad 2.43$$

2.2.2. Acoustic power with viscosity

According to Eq. 2.28, acoustic power can be expressed as

$$d\dot{W} = -\frac{1}{2}\rho_m\omega\frac{Im[-\chi_v]}{|1-\chi_v|^2}A|U|^2dx - \frac{1}{2}|P|^2\frac{(\gamma-1)\omega A\, Im[-\chi_\alpha]}{\gamma P_m}dx + \frac{1}{2}A\, Re[g_a\,\tilde{P}U]\frac{1}{T_m}\nabla T_m\, dx + \frac{1}{2}A\, Im[g_a\tilde{P}U]\frac{1}{T_m}\nabla T_m\, dx \quad 2.44$$

Equation 2.44 can be divided into four parts. The first term is viscous dissipation $\dot{W}_v$. The second term is $\dot{W}_p$, the third and last term are $\dot{W}_{progg}$ and $\dot{W}_{stand}$, respectively.

Those can be written as follows [36]:

$$d\dot{W}_v = -\frac{1}{2}\rho_m\omega\frac{Im[-\chi_v]}{|1-\chi_v|^2}A|U|^2dx \quad 2.45$$

$$d\dot{W}_P = -\frac{1}{2}A|P|^2\frac{(\gamma-1)\omega\, Im[-\chi_\alpha]}{\gamma P_m}dx \quad 2.46$$

$$d\dot{W}_{progg} = \tfrac{1}{2}A\, Re[g_a\,\tilde{P}U]\tfrac{1}{T_m}\nabla T_m \text{ dx} \quad 2.47$$

$$d\dot{W}_{stand} = -\frac{1}{2}A\, Im[g_a\tilde{P}U]\frac{1}{T_m}\nabla T_m\, dx \quad 2.48$$

where g_a is a non-dimensional quantity defined as [21]

$$g_a = \frac{\chi_\alpha - \chi_v}{(1-\sigma)(1-\chi_v)} \quad 2.49$$

According to Fig. 2.4 and eqs. 2.45 to 2.50, when $\omega\tau_\alpha < 0.1$, $Im\{g_a\} \sim 0$ and $Re\{g_a\}\sim 1$. Therefore, $\dot{W}_{progg}$ would become dominant. It indicates that travelling wave works well on that $\omega\tau_\alpha$. On the other hand, if $\omega\tau_\alpha\sim 3$, $Im\{g_a\}\sim -0.45$, and $Re\{g_a\}\sim 0.6$. Hence, $\dot{W}_{stand}$ and $\dot{W}_{progg}$ take a part in production or absorption of acoustic power. It implies that travelling and standing wave work together. In addition, when $\omega\tau_\alpha \gg 10$, so $\dot{W}_{progg}$ and $\dot{W}_{stand}$ vanish. It means that there is no production and absorption of acoustic power.

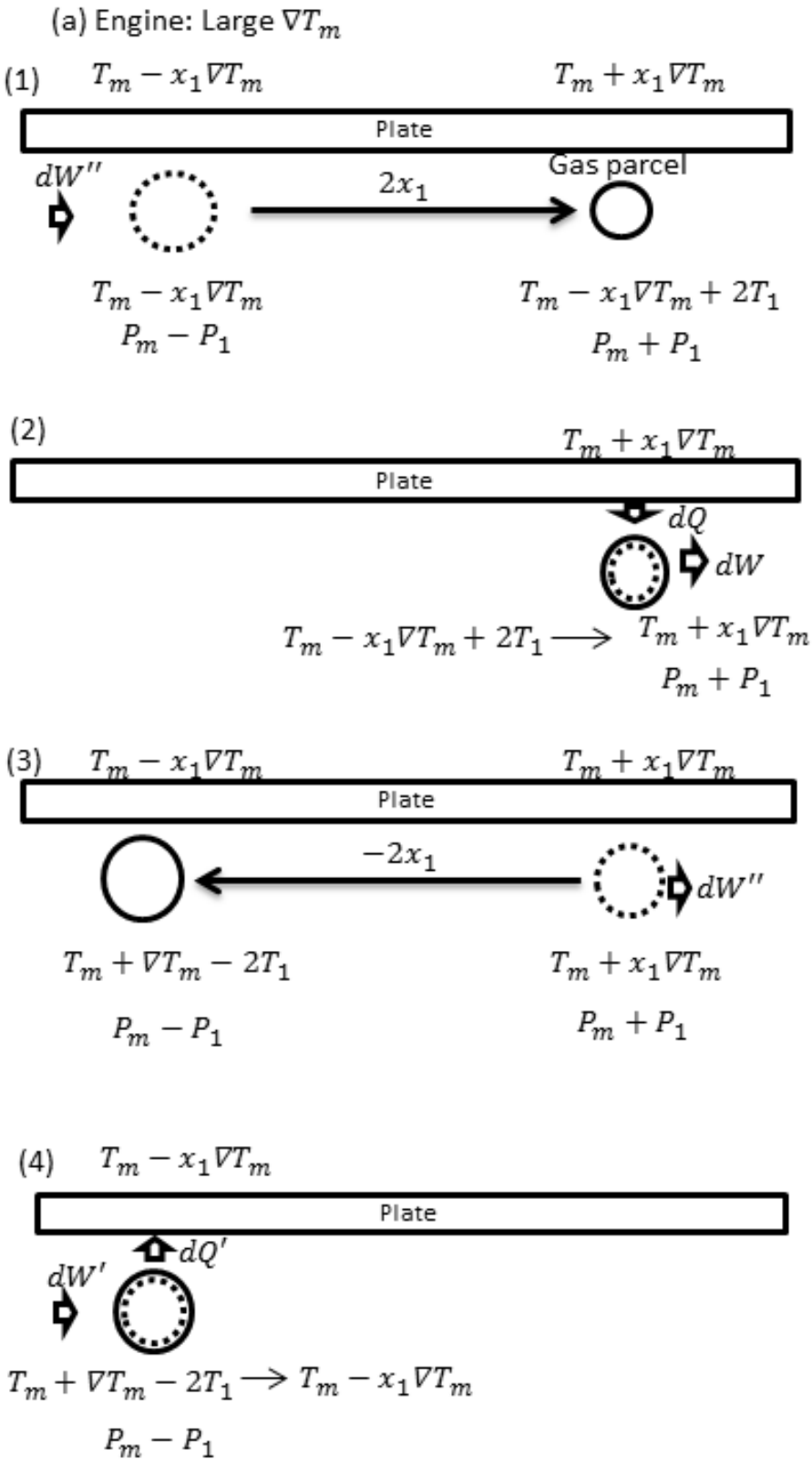

Fig. 2.2 Typical fluid parcels (standing wave) in (a) a thermoacoustic engine [10].

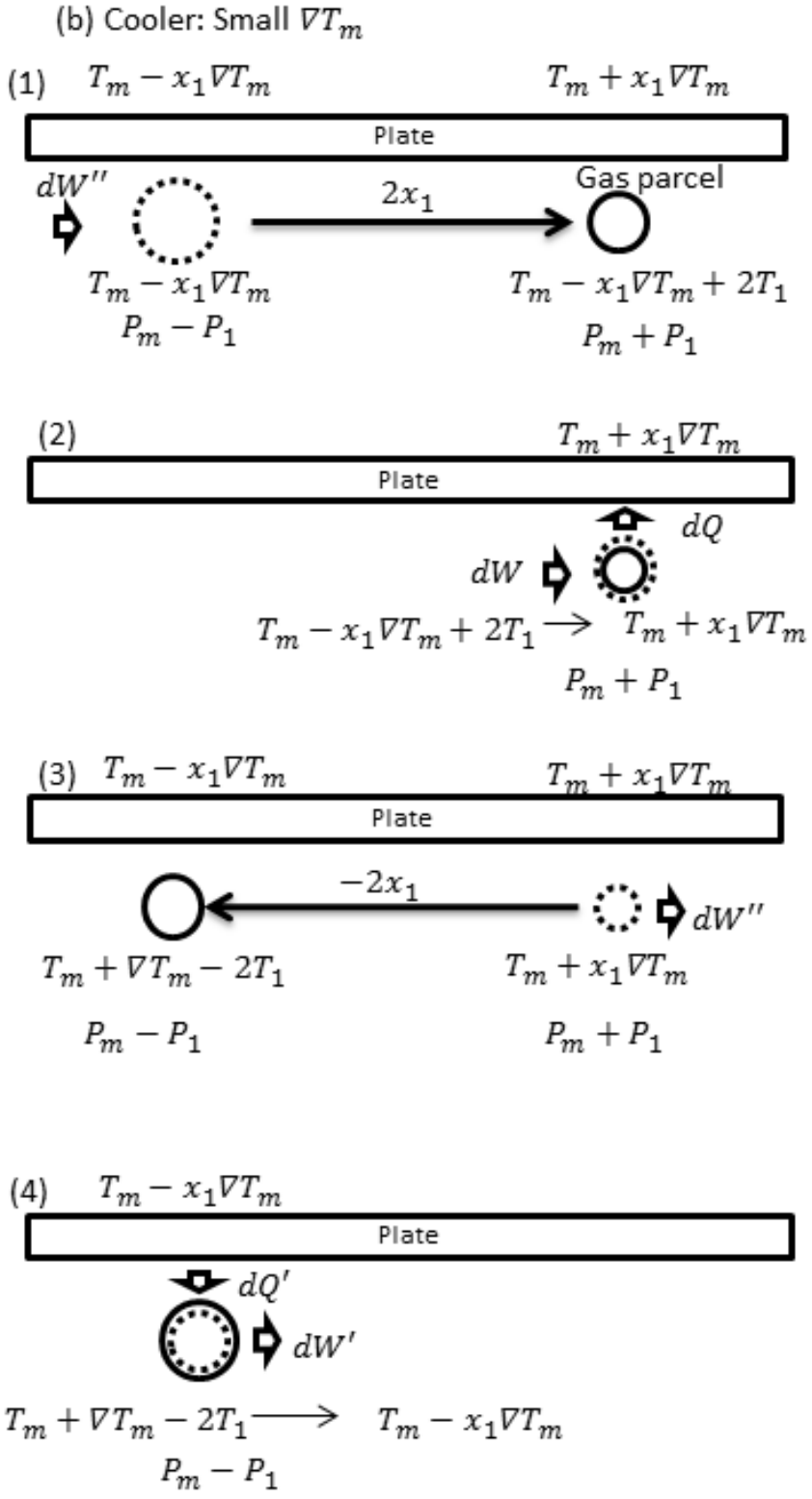

Fig. 2.2 Typical fluid parcels (standing wave) in (b) a thermoacoustic cooler[10].

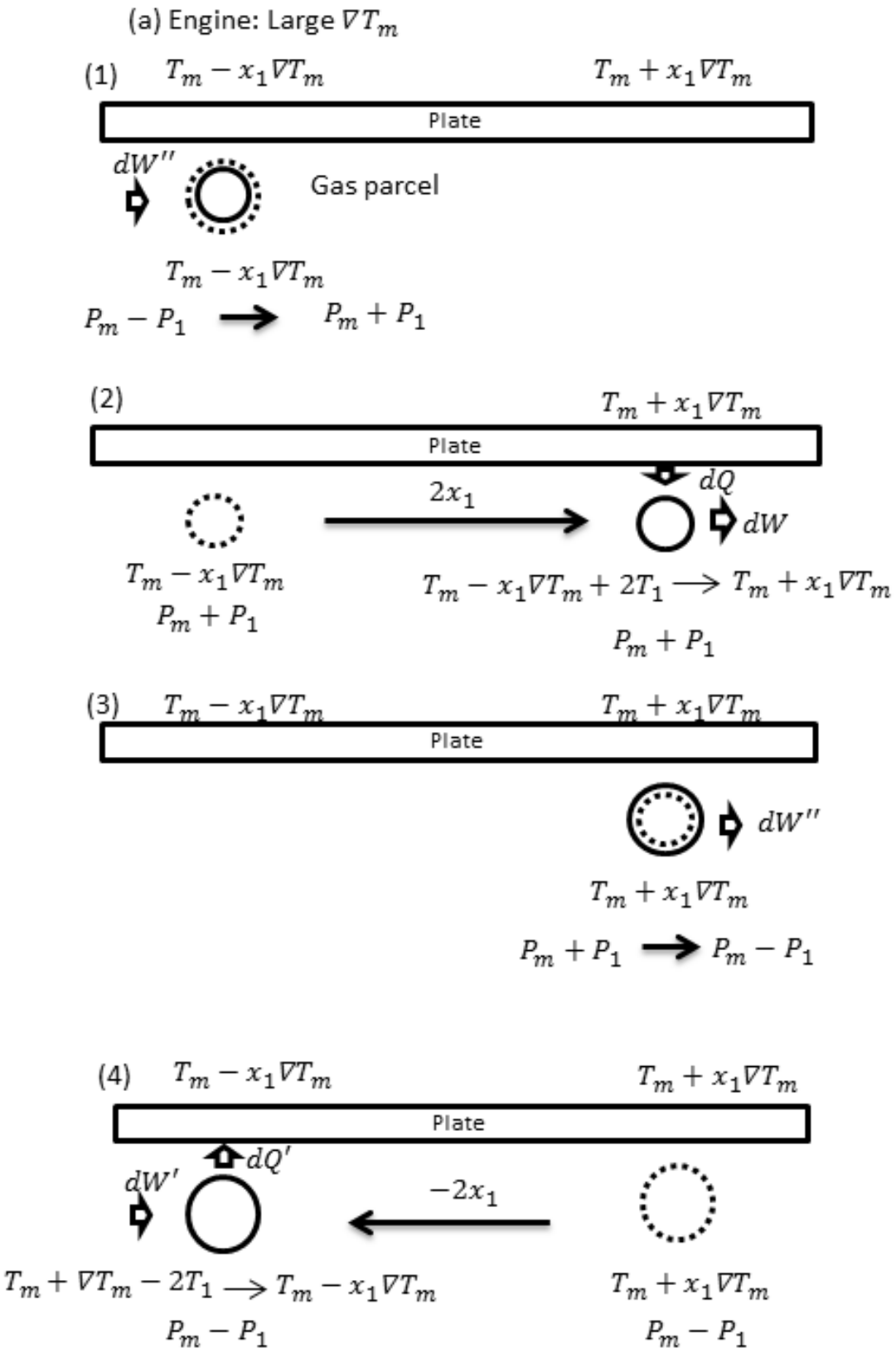

Fig. 2.3 (a) Typical fluid parcels (travelling wave) in (a) a thermoacoustic engine[10].

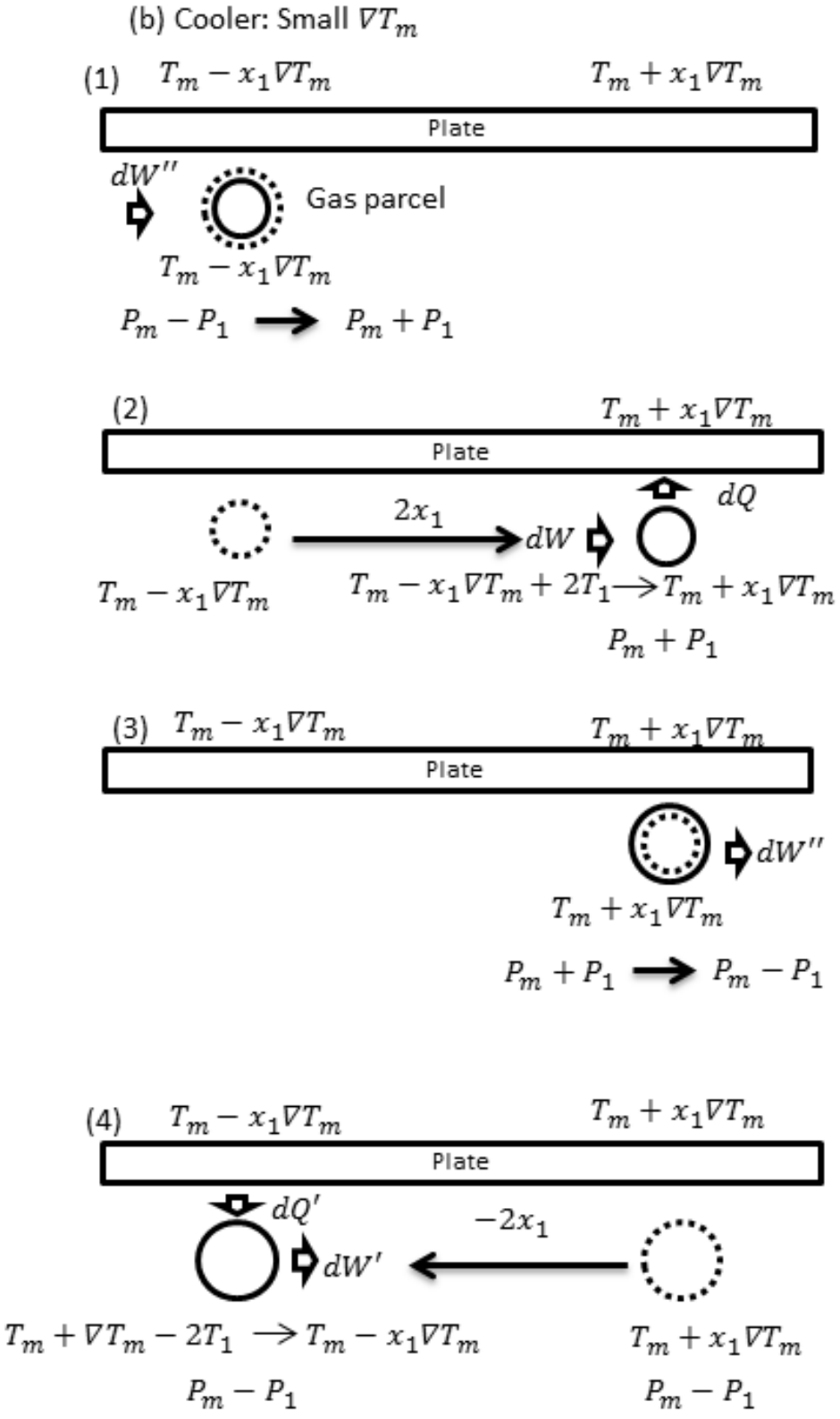

Fig. 2.3 Typical fluid parcels (travelling wave) in (b) a thermoacoustic cooler[10].

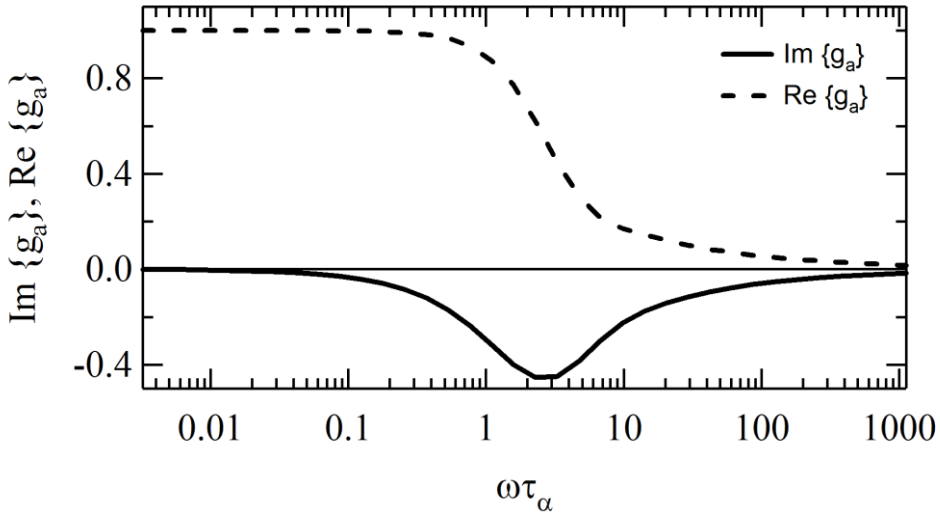

Fig. 2.4 g_a for circular cylinder; horizontal axis is $\omega\tau_\alpha$ [36]

2.3. Total Power

According to the Rott approximation, the total power $\dot{H}$ can be written [34]

$$\dot{H} = \frac{1}{2}\rho_m \int Re\left[H\tilde{U}\right] dA - (Ak + A_{solid}k_{solid})\frac{dT_m}{dx} \qquad 2.50$$

The first term represents the enthalpy flux and the second term represents the heat conduction of gas and wall stack.

Enthalpy is defined as [34]

$$H = \frac{\gamma}{\gamma - 1}\Re T = c_p T \qquad 2.51$$

where $\Re$ is the gas constant and it defines as $\Re = \Re_{univ}/m$. $\Re_{univ}$ is universal gas constant whose the value is 8.314 J/mol.K and m is molar mass.

σ is the Prandtl number. Substituting eq. 2.52 to eq.2.51 yields [34]

$$\dot{H} = \frac{1}{2}\rho_m c_p \int Re\left[T\tilde{U}\right] dA - (Ak + A_{solid}k_{solid})\frac{dT_m}{dx} \qquad 2.52$$

where T can be expressed as

$$T = \frac{1}{\rho_m c_p}(1-\chi_\alpha)P - \frac{1}{i\omega}\frac{(1-\chi_\alpha)-\sigma(1-\chi_v)}{(1-\chi_v)(1-\sigma)}\frac{dT_m}{dx}U \tag{2.53}$$

Using Eqs. 2.13 and 2.53 for U and T and performing the integration in Eq. (2.52) yields [34].

$$\begin{aligned}\dot{H} = \frac{1}{2}Re\left[P\tilde{U}\left(1-\frac{\chi_\alpha-\tilde{\chi}_v}{(1+\sigma)(1-\tilde{\chi}_v)}\right)\right] \\ + \frac{\rho_m c_p|U|^2}{2A\omega(1-\sigma)\left|1-\tilde{f}_v\right|^2}Im(\chi_\alpha+\sigma\chi_v)\frac{dT_m}{dx} \\ - (Ak + A_{solid}k_{solid})\frac{dT_m}{dx}\end{aligned} \tag{2.54}$$

The total power can be written

$$\dot{H} = \frac{1}{2}Re\left[P\tilde{U}\right] + \frac{1}{2}\rho_m T_m \int Re\left[S\tilde{U}\right]dA - (Ak + A_{solid}k_{solid})\frac{dT_m}{dx} \tag{2.55}$$

where S is entropy. The first term is acoustic power, and the second and last terms are heating power $\dot{Q}$.

2.4 Heating Power

2.4.1 Heating power with zero viscosity

Heating power can be found using expression

$$\dot{Q} = \dot{H} - \dot{W} \tag{2.56}$$

Here, we do not take into account the value of fluid and plate conductivity. In inviscid fluid where the viscosity is negligible, the heating power for standing wave can be expressed as

$$\dot{Q} = \frac{dQ}{dt} = \frac{1}{2}|P||U|\,A\,Im[-\chi_\alpha]\left(\frac{dT_m/dx}{\nabla T_{crit}} - 1\right) \tag{2.57}$$

Equation 2.57 shows the value of heating power, which implies the total heat flux $\dot{Q}$

along the plate. When $\nabla T_m/dx = \nabla T_{crit}$, so there is no heat flux. For $dT_m/dx > \nabla T_{crit}$, the fluid parcel moves a distance $2x \sim 2U/\omega$ toward the pressure node [see step. 3 Fig. 2.2 (a)] and deposit an amount of heat dQ[see step. 4 Fig. 2.2 (a)]. This is part of the thermodynamic cycle of the engine. On the other hand, when $dT_m/dx < \nabla T_{crit}$, the fluid parcel moves a distance $2x$ toward the pressure antinode [see step. 3 Fig. 2.2 (b)] and deposit an amount of heat dQ [see step. 3 Fig. 2.2 (b)]. This is part of the thermodynamic cycle of the cooler.

For travelling wave mode, the heating power can be expressed as

$$\dot{Q} = \frac{1}{2}|P||U|A\, Im[-\chi_\alpha]\left(\frac{dT_m/dx}{\nabla T_{crit}} - \frac{Re[\chi_\alpha]}{Im[-\chi_\alpha]}\right) \qquad 2.58$$

For mix standing and travelling wave mode, the heating power can be expressed as follow

$$\dot{Q} = -\frac{1}{2}A\left(\, Re\left[\chi_\alpha\, P\tilde{U}\right] + Im\left[\chi_\alpha\, P\tilde{U}\right]\right) + A\frac{\rho_m c_p|U|^2}{2\omega(1-\sigma^2)|1-\chi_v|^2}Im(\chi_\alpha + \sigma\tilde{\chi}_v)\frac{dT_m}{dx} \qquad 2.59$$

2.4.2 Heating power with viscosity

Heating power (not pure standing nor travelling wave) considering the viscosity, thermal conductivity of the fluid and plate can be expressed as follow

$$\dot{Q} = -\frac{1}{2}A\, Re\left[g_b\, P\tilde{U}\right] - \frac{1}{2}A\, Im\left[g_b\, P\tilde{U}\right] + A\frac{\rho_m c_p|U|^2}{2\omega(1-\sigma^2)|1-\chi_v|^2}Im(\chi_\alpha + \sigma\tilde{\chi}_v)\frac{dT_m}{dx} + (Ak + A_{solid}\, k_{solid})\frac{dT_m}{dx} \qquad 2.60$$

The first, second, third and last terms of Eq. 2.61 can be written as [36,37,38]

$$\dot{Q}_{progg} = -\frac{1}{2} A\, Re\left[g_b\, P\tilde{U}\right] \tag{2.61}$$

$$\dot{Q}_{stand} = -\frac{1}{2} A\, Im\left[g_b\, P\tilde{U}\right] \tag{2.62}$$

$$\dot{Q}_d = A \frac{\rho_m c_p |U|^2}{2\omega(1-\sigma^2)|1-\chi_v|^2} Im(\chi_\alpha + \sigma\tilde{\chi}_v) \frac{dT_m}{dx} \tag{2.63}$$

$$\dot{Q}_k = -(Ak + A_{solid}\, k_{solid}) \frac{dT_m}{dx} \tag{2.64}$$

respectively.

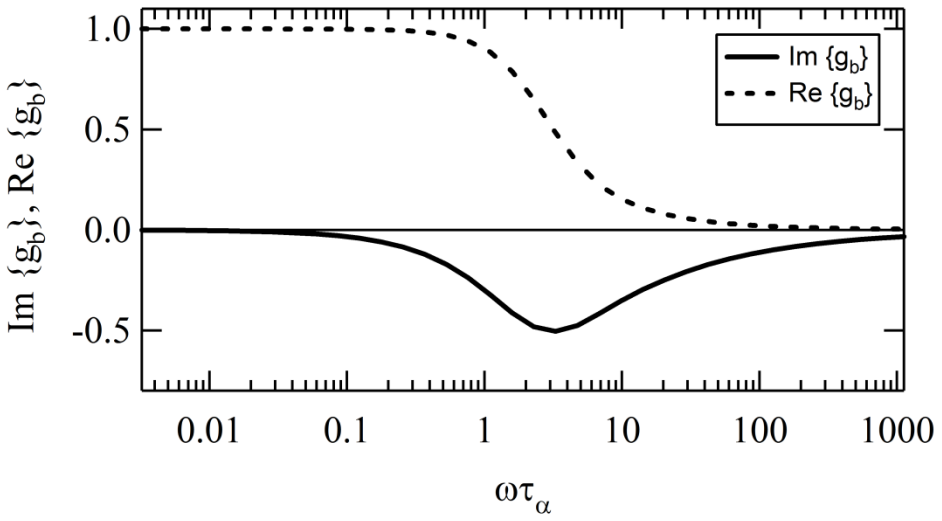

Fig. 2.5 g_b for circular cylinder; horizontal axis is $\omega\tau_\alpha$ [36]

Here, A and k are the area and thermal conductivity of fluid. A_{solid} and K_{solid} are the area and thermal conductivity of the plate. g_b in eqs. 2.62 and 2.63 is defined as [36,38]

$$g_b = \frac{\chi_\alpha - \tilde{\chi}_v}{(1+\sigma)(1-\tilde{\chi}_v)} \tag{2.65}$$

As we can see in figure 2.5, when $\omega\tau_\alpha < 0.1$, the progressive component $\dot{Q}_{progg}$ becomes dominant. If $\omega\tau_\alpha \sim 3$, the standing component $\dot{Q}_{stand}$ and dream pipe component $\dot{Q}_d$ become high. If $\omega\tau_\alpha \gg 10$, Q vanishes.

2.5 Conclusion

This chapter gives the theory of thermoacoustic which elucidates the fundamental concept of it. It also shows Rott's equations which is essential to calculate the acoustic field distribution inside the looped tube and all of the components. In this theory, we also explain about acoustic power and heating power.

Chapter 3

Transfer Matrix

In this chapter, we describe the calculation method of the transfer matrix of the components in a thermoacoustic cooler system. Due to the boundary condition, the thermoacoustic cooler system can be divided into three different systems. The first is a cooler driven by an electrodynamic loudspeaker, the second is a cooler driven by an engine in a straight tube, and the third is a cooler driven by an engine in a looped tube.

To calculate the performance of a thermoacoustic cooler system, we use a transfer matrix. The transfer matrix is based on the momentum and continuity equations derived by Rott [29]. The equations were written in eqs. 2.13 and 2.14. Here, the assumption that the heat capacity of the channel wall is considerably larger than that of the working gas. Eqs. 2.13 and 2.14 can be modified in a matrix form as follows [39]:

$$\frac{d}{dx}\begin{pmatrix} P(x,t) \\ U(x,t) \end{pmatrix} = C(x)\begin{pmatrix} P(x,t) \\ U(x,t) \end{pmatrix} \tag{3.1}$$

$$C(x) \equiv \begin{pmatrix} 0 & -\frac{1}{A}\frac{i\omega\rho_m}{1-\chi_\nu} \\ -\frac{i\omega A[1+(\gamma-1)\chi_\alpha]}{\gamma P_m} & \frac{\chi_\alpha-\chi_\nu}{(1-\chi_\nu)(1-\sigma)}\frac{1}{T_m}\frac{dT_m}{dx} \end{pmatrix}$$

It should be noted that $\rho_m, \gamma, \chi_\nu, \chi_\alpha$ and σ depend on T_m.

When $dT_m/dx = 0$. Eq. 3.1 can be solved analytically. This is because $\chi_\nu, \chi_\alpha, \gamma$ and σ are independent of *x*. When the oscillatory pressure and velocity at point x_0 are denoted by P_0 and U_0, respectively, the solution can be expressed as

$$\begin{pmatrix} P(x,t) \\ U(x,t) \end{pmatrix} = M_1(x,x_0)\begin{pmatrix} P_0(x,t) \\ U_0(x,t) \end{pmatrix}, \tag{3.2}$$

$$M_I(x,x_0) \equiv \begin{pmatrix} \cos[k(x-x_0)] & \dfrac{-i\omega\rho_m \sin[k(x-x_0)]}{Ak(1-\chi_\nu)} \\ \dfrac{Ak(1-\chi_\nu)sin[k(x-x_0)]}{i\omega\rho_m} & \cos[k(x-x_0)] \end{pmatrix}$$

Here, k is the complex wave number given by

$$k = \frac{\omega}{a}\sqrt{\frac{1+(\gamma-1)\chi_\alpha}{1-\chi_\nu}} \tag{3.3}$$

where a is the adiabatic sound speed. Equation (3.2) shows that when P and U are specified for one point, the distributions of P and U along the tube without the temperature can be calculated.

When $dT_m/dx \neq 0$, it is difficult to solve Eq.(3.1) analytically. Hence, it is computationally integrated. By applying a forward difference scheme using the fourth-order Rung-Kutta method to Eq. (3.1),

$$\begin{pmatrix} P(x+\Delta x,t) \\ U(x+\Delta x,t) \end{pmatrix} = \big(E+\Delta x C'(x)\big)\begin{pmatrix} P(x,t) \\ U(x,t) \end{pmatrix} \tag{3.4}$$

$$C'(x) = \frac{1}{6}(RK_A + 2RK_B + 2RK_C + RK_D)$$

$$RK_A = C(x),$$

$$RK_B = C(x+\Delta x/2)\left(E+\tfrac{\Delta x}{2}RK_A\right),$$

$$RK_C = C(x+\Delta x/2)\left(E+\frac{\Delta x}{2}RK_B\right)$$

$$RK_D = C(x+\Delta x)(E+\Delta x RK_C)$$

can be obtained, where E is a unit matrix. Hence,

$$\begin{pmatrix} P(x,t) \\ U(x,t) \end{pmatrix} = M_{II}(x,x_0)\begin{pmatrix} P_0(x_0,t) \\ U_0(x_0,t) \end{pmatrix} \tag{3.5}$$

$$M_{II}(x,x_0) \equiv (E+\Delta x C'_{n-1})(E+\Delta x C'_{n-2})\ldots(E+\Delta x C'_1)(E+\Delta x C'_0)$$

is obtained. In Fig. 3.2, n is the number of partitions between x_0 and x, Δx is defined as $(x - x_0)/n$, and C_j' represents C' at $x = x_0 + j\Delta x$. Using eq. 3.5, the distributions of P and U in a uniform flow path can be calculated.

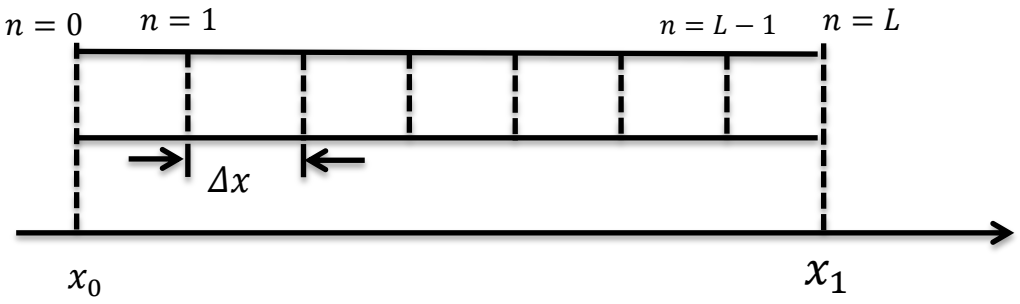

Fig. 3.1 Model the tube with temperature gradient

Here, n is the number of partitions between x and x_0, Δx is defined as $(x - x_0)/n$. D_j' represents D' at $x = x_0 + j\Delta x$.

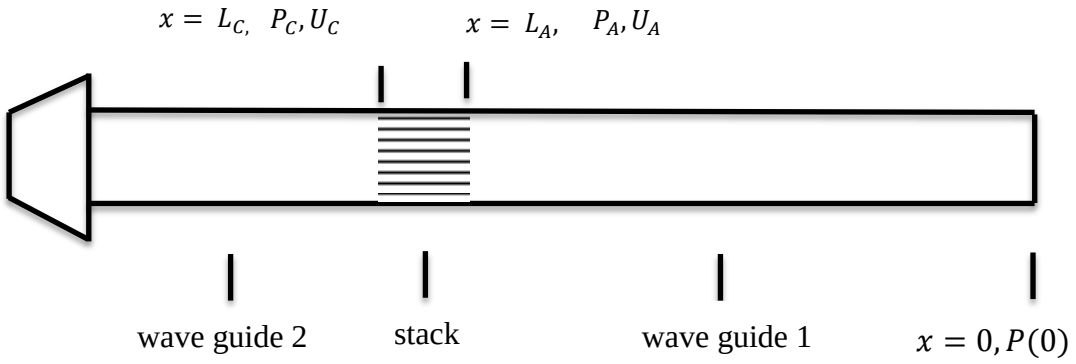

Fig. 3.2 The schematic illustration of a cooler
driven by an electrodynamic loudspeaker in a straight tube.

3.1 A Cooler driven by an electrodynamic loudspeaker

A cooler driven by an electrodynamic loudspeaker is shown in Fig. 3.2. It is divided into 3 components: (1) wave guide 1, (2) stack, (3) wave guide 2.

Here, the procedure of the calculation of the $\dot{W}$ and $\dot{Q}$ are described in Fig. 3.3.

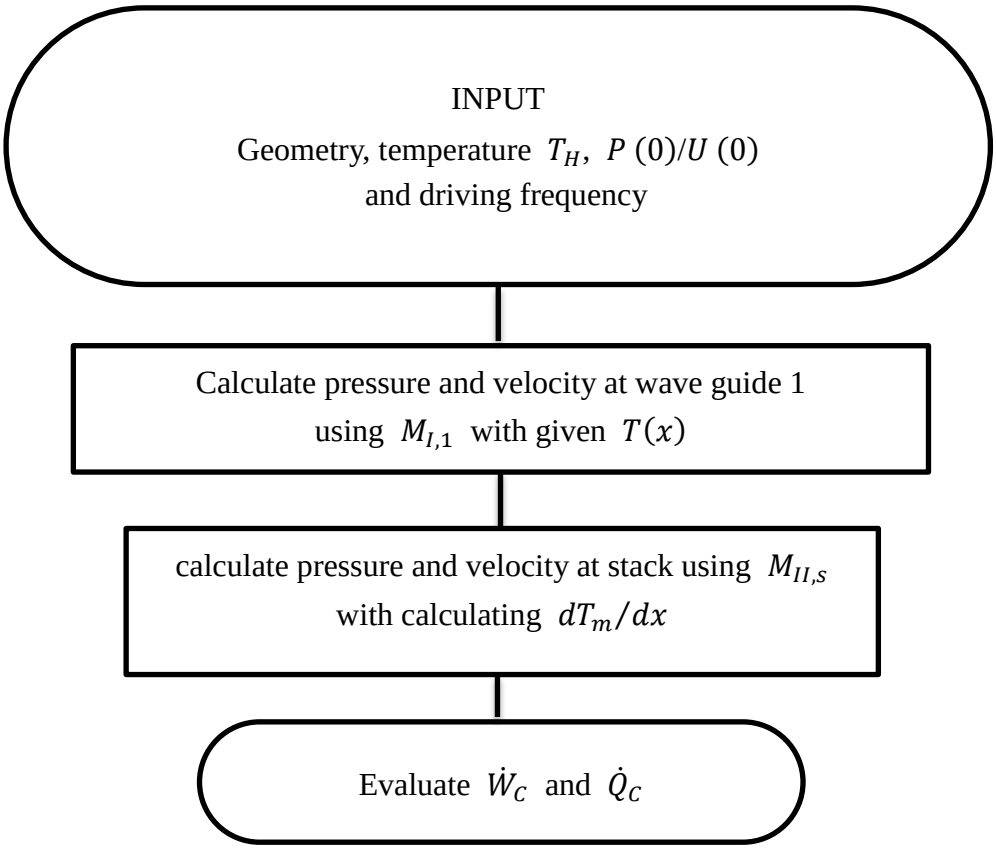

Fig. 3.3 flow chart for evaluating $\dot{W}_C$ and $\dot{Q}_C$

In the first step, the geometry of the cooler, temperatures T_H and T_C, driving frequency, $P(0)$, and $U(0)$ are determined as the input conditions. In the second step, the transfer matrix of the straight tube from $x = 0$ to $x = L_A$, $M_{I,1}$ [See Fig.3.3] is calculated by using M_I at $T_m = 300\,K$. Using $M_{I,1}$, P_A and U_A is calculated. In the

third step, using transfer matrix M_{II}, the transfer matrix of the stack $M_{II,s}$ is calculated. Using $M_{II,s}$, the distribution of pressure and velocity (P_A to P_C and U_A to U_C) in the stack is calculated with calculating dT_m/dx. In the last step, $\dot{W}_C$ and $\dot{Q}_C$ is evaluated using $P_C, U_C,$ and $M_{II,s}$.

3.2 A Cooler driven by an engine in a straight tube

A cooler driven by an engine in a straight tube is shown in Fig. 3.4 [10]. It is divided into 14 components: (1) wave guide 1, (2) connecting point 1, (3) hot heat exchanger, (4) connecting point 2, (5) engine stack, (6) connecting point 3, (7) ambient heat exchanger 1, (8) ambient heat exchanger 2, (9) connecting point 4, (10) cooler stack, (11) connecting point 5, (12) cold heat exchanger, (13) connecting point 6, (14) wave guide 2.

3.2.1 Calculation procedure

The calculation flow chart is shown in figure 3.5 and described as follows:

1. The geometry of the cooler, T_C, driving frequency are set. The ambient temperature T_A is set at 297 K and cooling temperature T_C is varied as a part of result.
2. The stability limit condition is calculated [40]. (This method is described in sec. 3.2.2). It is calculated with (dT_m/dx) = constant. As a result of the calculation, T_H, ω, $P_a/P_{E,A}$ are obtained.
3. By using the obtained values for T_H, ω, $P_a/P_{E,A}$, the pressure and velocity at the end of the stack, namely $(P_{E,H}/U_{E,H})$, $(P_{C,A}/U_{C,A})$ and $(P_{C,C}/U_{C,C})$ are

calculated with calculating dT_m/dx.

4. The pressure and velocity obtained from the previous result are used for calculating the acoustic power at the ends of the engine and cooler stacks, $(\dot{W}_{E,A}, \dot{W}_{E,H}, \dot{W}_{C,A}$ and $\dot{W}_{C,C})$ and also the heating power at the end of them $(\dot{Q}_H$ and $\dot{Q}_C)$.

5. 3.2.2 Method for calculating stability limit

In the wave guide 1, the transfer matrix $M_{I,w1}$ of this region was calculated by using M_I in eq. 3.2. Similarly, the transfer matrices for hot heat exchanger, ambient heat exchanger 1, ambient heat exchanger 2, cold heat exchanger and wave guide 2 are calculated and denoted by $M_{I,h}$, $M_{I,a1}$, $M_{I,a2}$, $M_{I,c}$, $M_{I,w2}$, respectively. In the engine stack, eq. 3.5 is used to compute the transfer matrix $M_{II,es}$. Similarly, in the cooler stack, it is also used to compute the transfer matrix $M_{II,cs}$. The total flow-path areas in the components are different from each other, and thus the connecting matrix is as follows:

$$K_{m,n} = \begin{pmatrix} 1 & 0 \\ 0 & A_n/A_m \end{pmatrix} \quad 3.6$$

Where A denotes the total area and the subscripts m and n denote the number of the components. The transfer matrices of the components and connecting matrices are used to express the transfer matrix of the total system as follows:

$$M_{all} = M_{I,w1}K_{2,1}M_{I,h}K_{3,2}M_{II,es}K_{4,3}M_{I,a1}M_{I,a2}K_{5,4}M_{II,cs}K_{6,5}M_{I,C}K_{7,6}M_{I,w2} \quad 3.7$$

Here, $K_{2,1}, K_{3,2}, K_{4,3}, K_{5,4}, K_{6,5}$, and $K_{7,6}$ are the connecting matrix between wave guide 1 and hot heat exchanger, hot heat exchanger and engine stack, engine stack and ambient heat exchanger, ambient heat exchanger and ambient heat exchanger of the cooler stack, cooler stack and cold heat exchanger, and cold heat exchanger and wave

guide 2, respectively. By using M_{all}, the oscillatory pressure P_a and cross-sectional mean of oscillatory velocity U_a are related to the oscillatory pressure P_b and cross-sectional mean of oscillatory velocity U_b as

$$M_{all}\begin{pmatrix} P_a \\ U_a \end{pmatrix} = \begin{pmatrix} P_b \\ U_b \end{pmatrix} \quad 3.8$$

For this tube, Eq. 3.8 can be modified as

$$M_{all}\begin{pmatrix} P_a \\ 0 \end{pmatrix} = \begin{pmatrix} 0 \\ U_b \end{pmatrix} \quad 3.9$$

This is because U_a in the closed end of the tube must be zero due to the closed end and P_b in the open end of the tube must be zero due to the open end. U_a and P_b in eq. 3.8 are nonzero if m_{11} is zero, i.e., if

$$m_{11} = 0 \quad 4.0$$

Therefore, Eq. 4.0 determines the condition of the stability limit in the straight tube with closed and open tube.

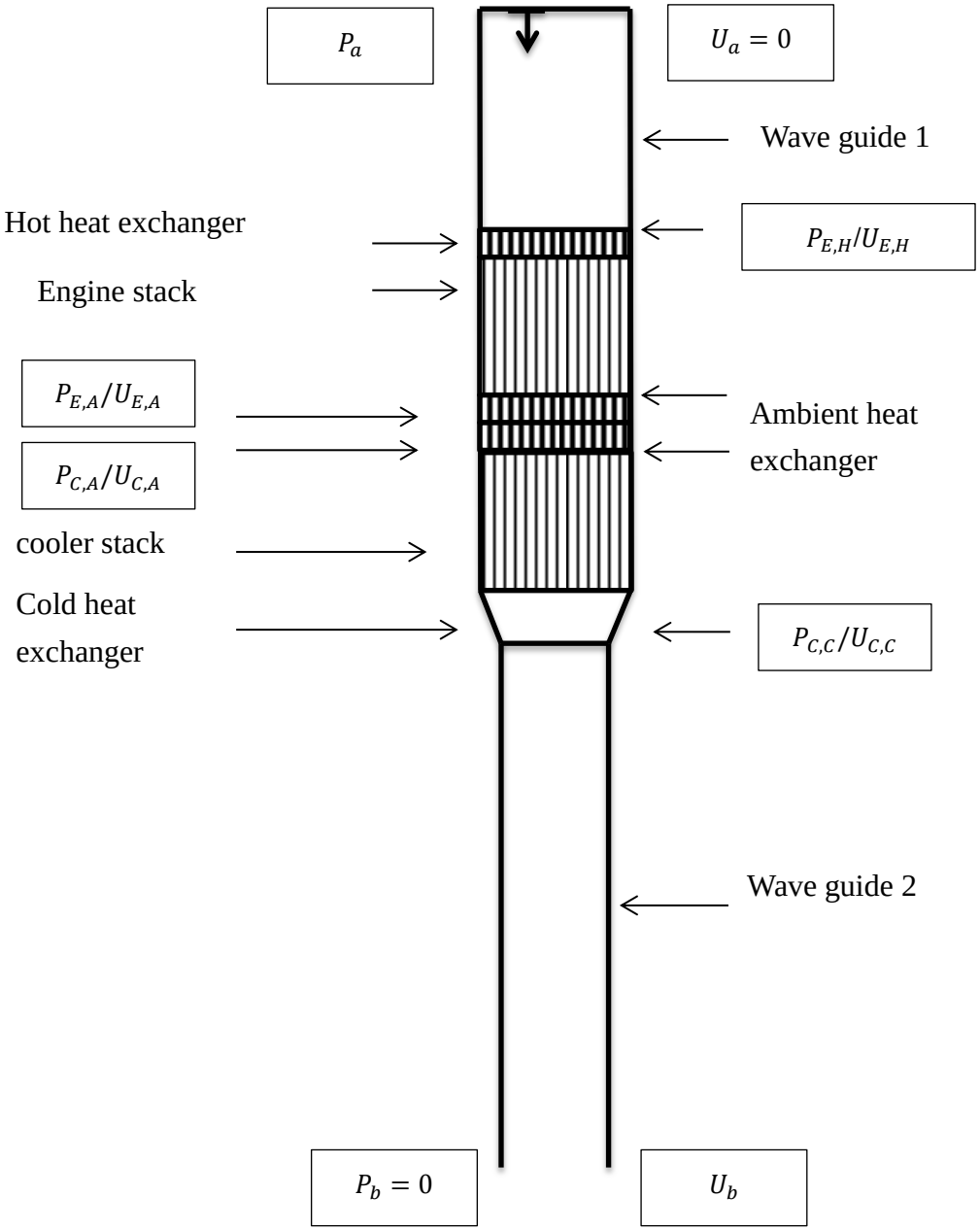

Fig. 3.4 Schematic illustration of a cooler driven by an engine in a straight tube [10].

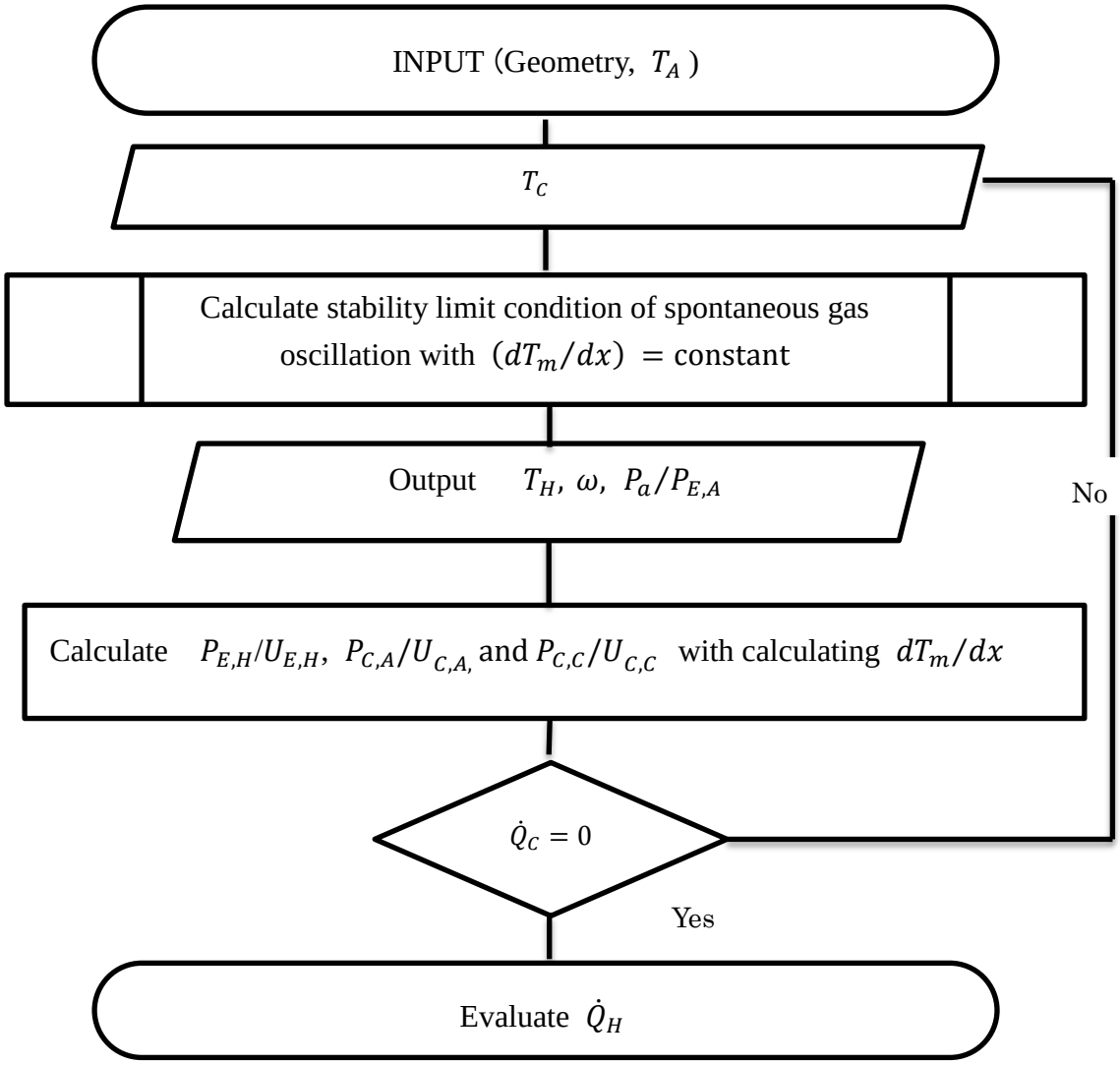

Figure 3.5 Flow chart for evaluating $\dot{W}_{E,A}$, $\dot{W}_{E,H}$, $\dot{W}_{C,A}$, $\dot{W}_{C,C}$, $\dot{Q}_H$ and $\dot{Q}_C$

3.3 A Cooler driven by an engine in a looped tube

A cooler driven by an engine in a looped tube is shown in Fig. 3.6 [23]. The length of the looped tube L_{loop} is 2.8 m, and its radius is 2 cm. The looped tube is filled with a 0.51 MPa helium gas. One of the stacks acts as an engine stack, and it is sandwiched

by ambient and hot heat exchangers. The other stack acts as a cooler stack, and it is sandwiched by ambient and cold heat exchangers. The length of the stacks is 4 cm. The distance between the two stacks is denoted as L (see Figure 3.6). This parameter is varied as one of important parameter to obtain the better performance. The stacks are modelled as an array of circular channels. The radii of the circular channels is denotes as r_e and the radii of the cooler is denoted as r_c. The porosity of the stacks is denoted as φ. $L, r_e, r_c,$ and φ are used as the parameters with respect to which the performance of the system is varied.

The ambient temperature T_A is 301 K, and the cold temperature T_C is 251 K, but the hot temperature T_H is determined as one of the calculation results. The parallel-stacked plates are the model of the heat exchangers. The space between the plates is 1 mm and the height is 10 mm. There are two thermal buffer tubes. The tubes exist along the looped tube. One of the thermal buffer tubes is positioned at the vicinity of the hot heat exchanger. The temperature in the thermal buffer tube changes from T_H to T_A. The other space is located at the vicinity of the cold heat exchanger, and the temperature changes from T_C to T_A (see Figure 3.6).

The looped tube in Fig.3.6 is modelled as a straight tube. The straight tube is divided into 10 components. They are (1) an ambient heat exchanger, (2) an engine stack, (3) a hot heat exchanger, (4) a thermal buffer tube (5) a wave guide, (6) another ambient heat exchanger, (7) a cooler stack, (8) a cold heat exchanger, (9) another thermal buffer tube, and (10) another wave guide. It is assumed that the temperature gradient is imposed only on components (2), (4), (7) and (9), and that T_m for components (1), (3), (5), (6), and (10) is maintained at an ambient temperature T_A, and T_m for component (8) is maintained at T_C.

In this subsection, the calculation method of the transfer matrix of the components (which are the waveguides, heat exchangers, stacks, and thermal buffer tubes) is described. Here, the assumption that the heat capacity of the channel wall is considerably larger than that of the working gas is used.

When $dT_m/dx = 0$. Eq.3.1 can be solved analytically. This is because $\chi_v, \chi_\alpha, \gamma$ and σ are independent of *x*. When the oscillatory pressure and velocity at point x_0 are denoted by P_0 and U_0, respectively, the solution can be expressed as eq. 3.2.

When $dT_m/dx \neq 0$, it is difficult to solve Eq.(3.1) analytically. Hence, it is computationally integrated. By applying a forward difference scheme using the fourth-order Rung-Kutta method to Eq. (3.1), Eq. 3.4 can be obtained, where *E* is a unit matrix. Hence, Eq. 3.5 is obtained. In Fig. 3.1, *n* is the number of partitions between x_0 and x, Δx is defined as $(x - x_0)/n$, and C_j' represents C' at $x = x_0 + j\Delta x$. Using eq. 3.5, the distributions of P and U in a uniform flow path can be calculated.

3.3.1 Calculation procedure

The calculation flow chart is shown in Figure 3.6 and is described as follows:

1. The geometry of the cooler system is set. The temperature of the hot end of the engine stack, T_H, is determined as a result of the calculation, while temperatures (T_A and T_C) are fixed as follows: $T_A = 301\ K$ and $T_C = 251\ K$.
2. The stability limit condition under which the spontaneous gas oscillation becomes neutral is calculated by using the transfer method [40]. As a result of this calculation, T_H, ω, $P_{E,A}$ and $U_{E,A}$ are obtained.
3. By using the obtained values for heating temperature T_H, angular frequency ω, and

impedance which is defined as the ratio of oscillatory pressure and velocity at the ambient end of the engine stack $P_{E,A}/U_{E,A}$, the ratio of oscillatory pressure and velocity at the hot end of the engine stack $P_{E,H}/U_{E,H}$, the ratio of oscillatory pressure and velocity at the ambient end of the cooler stack $P_{C,A}/U_{C,A}$, and the ratio of oscillatory pressure and velocity at the cold end of the cooler stack $P_{C,C}/U_{C,C}$ are calculated.

4. The obtained combinations of the pressure and velocity are used to calculate the acoustic power at the ends of the engine and cooler stacks, $(\dot{W}_{E,A}, \dot{W}_{E,H}, \dot{W}_{C,A}$ and $\dot{W}_{C,C})$. Moreover, the thermal power at the hot end of the engine stack and at the cold end of the cooler stack $(\dot{Q}_H$ and $\dot{Q}_C)$ are calculated by using the calculated $\dot{W}_{E,H}$ and $\dot{W}_{C,C}$.
5. The calculated $\dot{W}_{E,A}, \dot{W}_{E,H}, \dot{W}_{C,A}, \dot{W}_{C,C}, \dot{Q}_H,$ and $\dot{Q}_C$ are used to evaluate $\eta_E, \eta_{tube}, COP_C$ and COP_{total}.

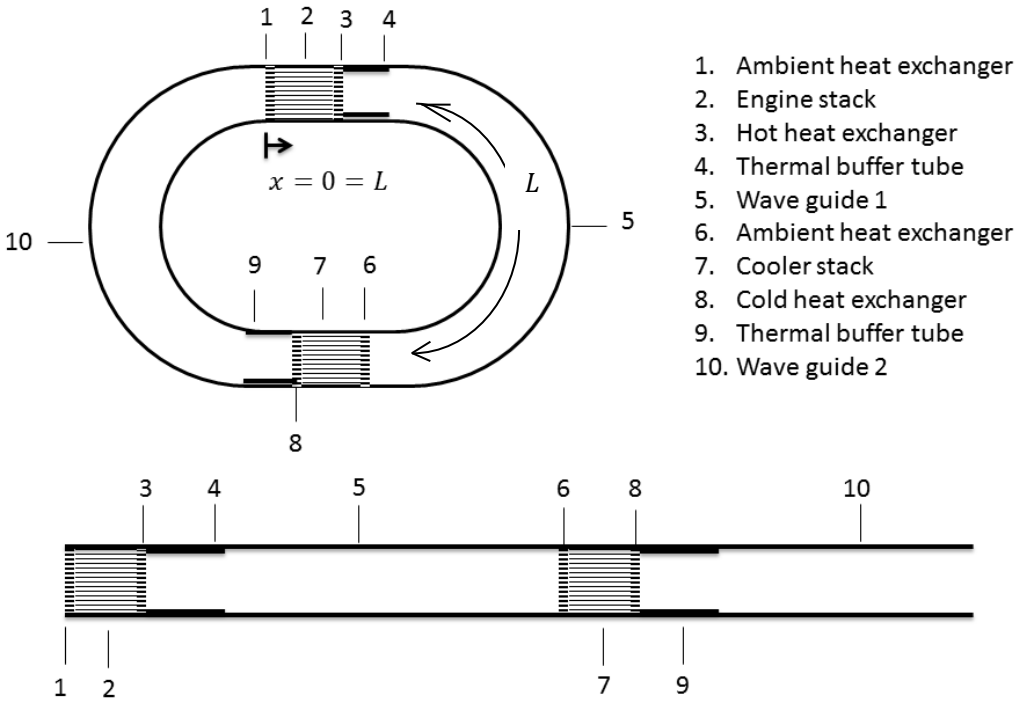

Figure 3.6 Schematic illustrations of a cooler driven by an engine in a looped tube modelled as a straight tube

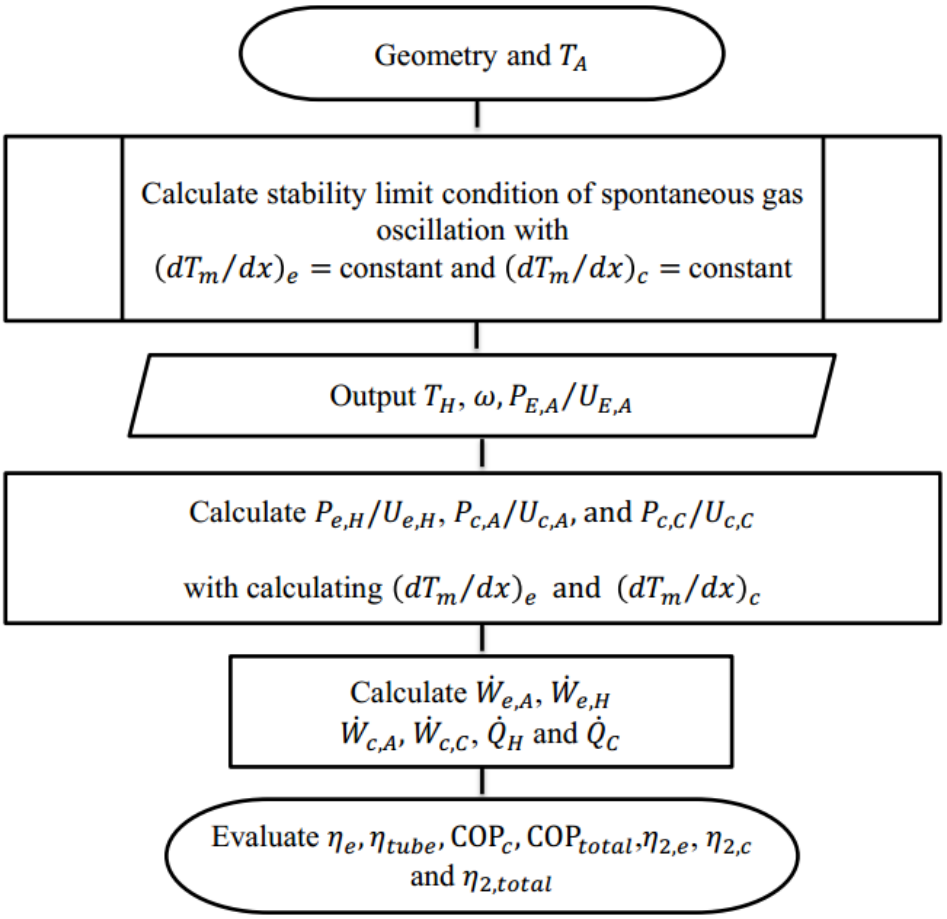

Figure 3.7 Flow chart for evaluating η_E, COP_C, η_{tube}, COP_{total}, $\eta_{2,e}$, $\eta_{2,c}$, and η_{total}

3.4 Conclusion

In this chapter, we describe the transfer matrix method. It was described that there are two different types of transfer matrices. The first is the transfer matrix for calculating acoustic field distribution without temperature gradient, and the second is the transfer matrix for calculating acoustic field distribution with temperature gradient. Here, we also described the transfer matrices methods that can be used by different configuration of the cooler.

Chapter 4

Validation of the Transfer Matrix

Transfer matrices are important in the calculation. In order to validate them, the comparison between calculations and experiments are needed. There are two different transfer matrices applied in different cooler system having many components. There are three different kinds of the system needed to be validated. The first is a cooler driven by an electrodynamic loudspeaker. In this case, we made a validation using comparison between calculation and experimental result conducted by Farikhah et.al [41]. The second is a cooler driven by an engine in a straight tube construsted by Swift [10] and the third is a cooler driven by an engine in a looped tube constructed by Yazaki et. al [23].

4.1 Design of thermoacoustic device using stems of goose down stack

The transfer matrix of a cooler driven by an electrodynamic loudspeaker shown in chapter 3 can be validated using the experimental result found by Farikhah et.al [41]. In order to show the validation of the transfer matrices, we calculate the temperature in the ambient and cold sides of the stack and compare them with the experimental results. Figure 4.1 shows the set-up of the experiment. The design is constructed with some apparatus. They are audio function generator, loudspeaker, voltmeter, ampere meter,

amplifire, resonator, temperature sensors (LM 35), thermometer digital, and a computer. First, the audio function generator is set. It is connected to an amplifire to amplify the input from audio function generator. Then, the output from amplifire is measured by ampere meter and voltmeter. In the same time, the input from the amplifire enters to the electrodynamic loudspeaker. In the loudspeaker the electrical audio signal converts an electrical audio signal (electrical power) into a corresponding sound (acoustic power). Then, the acoustic wave propagates along the straight tube (resonator) and enters the stack from the ambient stack. In addition, the end of the resonator is closed. In order to measure the cooling temperature, two temperature sensors attach in the ambient and cold ends of the stack. LM 35 is used as the sensors. The sensors are connected to a thermometer digital. The measured temperatures are shown in a computer. Moreover, it is measured within 120 second.

The resonance'frequency of resonator f is determined through equation below

$$f = \frac{nv}{4L} \tag{4.1}$$

Orde *n* is 1 while *v* is velocity of sound in air (331 m/s). The length of the resonator L is 0.75 m. In addition, the radius of the resonator r_r is 2.5 cm. Based on eq. 4.1, we got f is 110 Hz.

The stack is derived from the stem of goose down (Fig. 4.2). The form of stack is pores in which the radius of each pore is about 1 mm. There are 105 pores of the stems inserted into a circular tube which the diameter is about 50 mm, and the length is 100 mm.

There are some stages to make the stack. Firstly, the original stems are cut from top end of the goose down that the length is just approximately between 30 mm and 50 mm. Secondly, 2 or 3 of the stems are connected to each other to extend them become 100

mm. Then, the stems are bound by cardboard (Fig. 4.2).

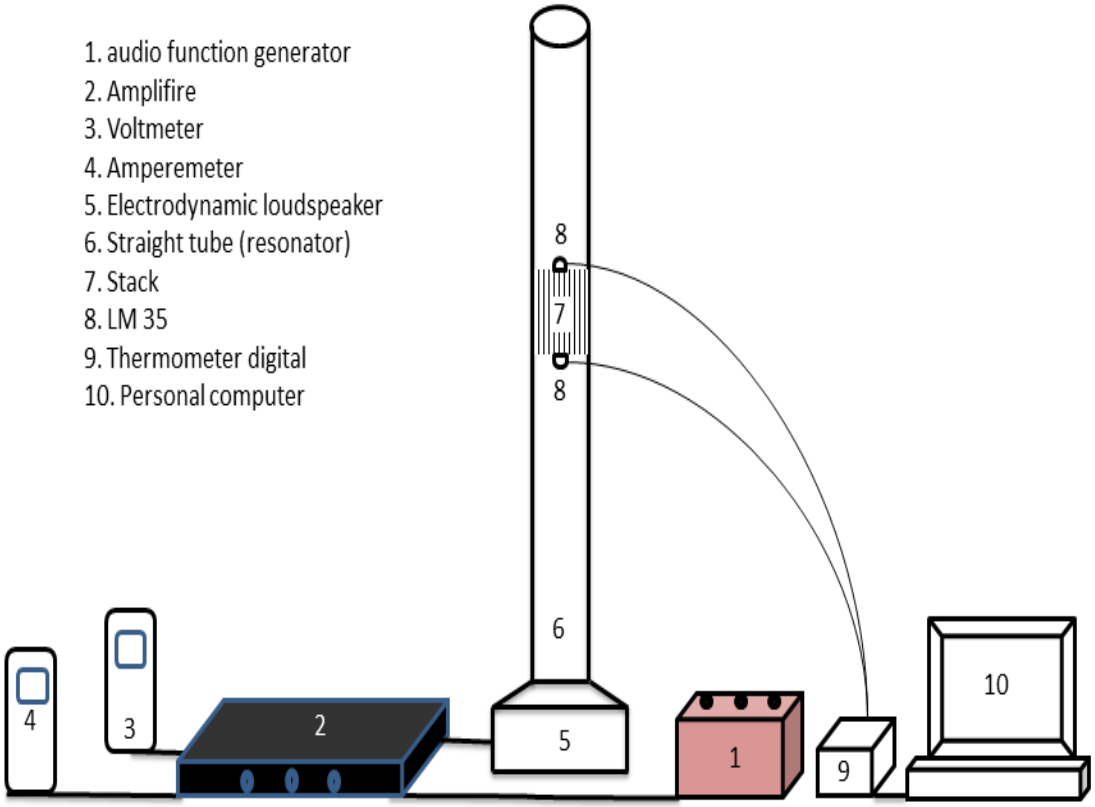

Figure 4.1 Design of thermoacoustic device [41]

Figure 4.2 stems of the goose down stack [41]

In term of stack, there is a dimensionless parameter for the geometry of the stack.

The thermal and viscous penetration depths are given by eqs. 4.2 and 4.3, respectively.

$$\delta_k = \sqrt{\frac{2K}{\rho c_p \omega}} \tag{4.2}$$

and

$$\delta_v = \sqrt{\frac{2\mu}{\rho\omega}} \tag{4.3}$$

where K, $\rho, \mu,$ and c_p is the thermal conductivity, density, viscosity and isobaric specific heat of gas, and ω is the angular frequency of the acoustic wave [44]. In this experiment the flow channel radius $r/\delta_k = 3.8$ and $r/\delta_v = 4.5$ [41].

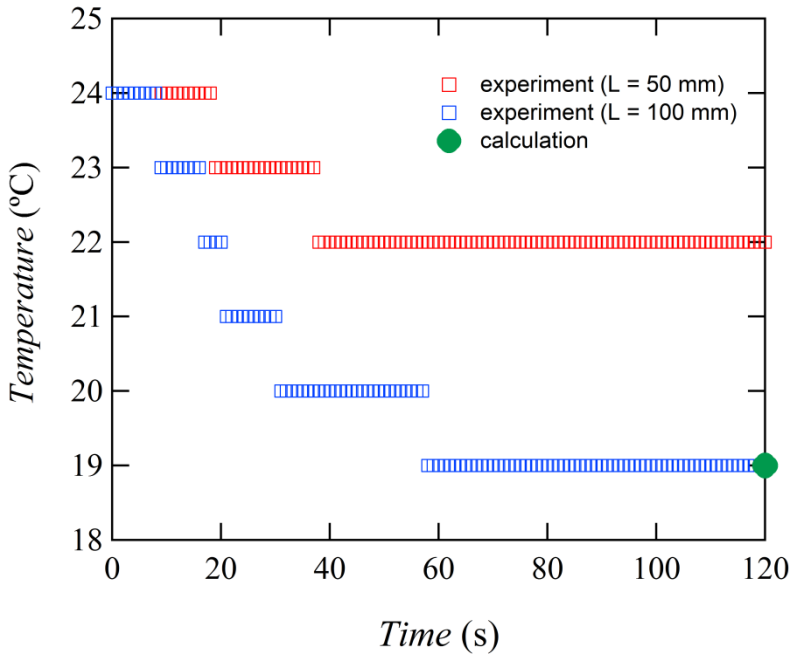

Figure 4.3 Temperature as a function of Time in the cold side of the stack [41]

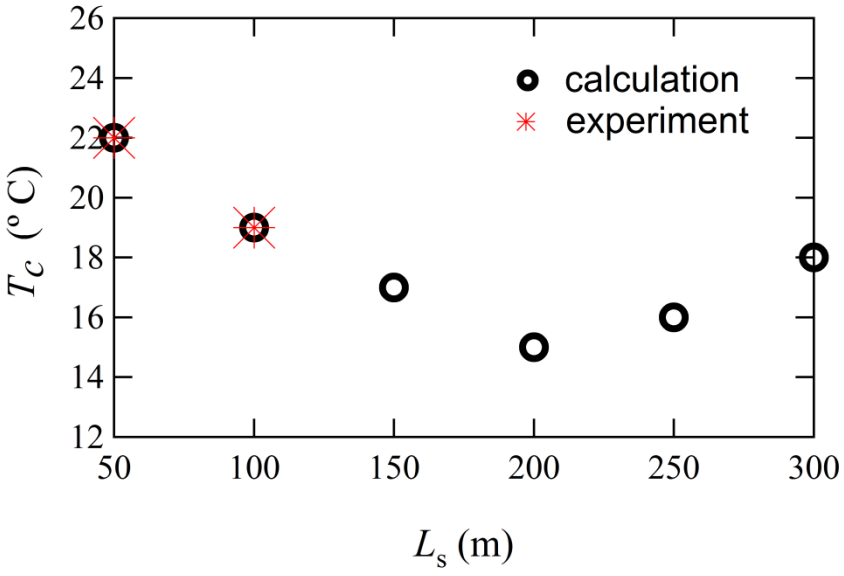

Figure 4.4 T_C as a function of L_S

The calculation of the cooling temperature in the cold side of the stack T_C is conducted using the transfer matrix in eqs. 3.4 and 3.5. In Figure 4.3, the numerically obtained T_C at $L_S = 50$ mm is denoted by square red markers, while the numerically obtained T_C at $L_s = 100$ mm is denoted by square blue markers. It should be noted that the experimental conditions outlined by Farikhah et.al [41]. The stack works as a cooler without ambient and cold heat exchangers. Moreover, the atmospheric air is used as a working gas. In addition, the length of the tube is 750 mm. As can be seen in this figure, the experimental result shows that in the cold side of the stack the temperature drops 2 ℃ from 24 ℃ to 22 ℃ at $L_s = 50\,mm$ and it drops 5 ℃ at $L_s = 100\,m$. In the calculation, T_C is calculated using the transfer matrix. The method for calculating T_C is follows:

1. The cooling power $\dot{Q}_C$ at $L_S = 50$ mm is calculated using the transfer matrix in eq. 3.5 and eq. 2.60. It is found that $\dot{Q}_C$ is 4.3 W.

2. T_C is experimentally measured without external cooling load ($\dot{Q}_{CC} = 0$). Here, $\dot{Q}_{CC}$ is defined as

$$\dot{Q}_{CC} = \dot{Q}_C - \dot{Q}_{loss} \quad 4.1$$

$$\dot{Q}_C = \dot{Q}_{loss} \quad 4.2$$

3. Coefficient of the material stack k_{eff} is calculated. It can be defined as

$$k_{eff} = \frac{(T_C - T_A)/L_S}{\dot{Q}_{loss}} \quad 4.3$$

where $\dot{Q}_{loss}$ is loss power and T_A is the ambient temperature. In this step, we use $L_s = 50$ mm. Using eq. 4.2 we can find k_{eff}. It is found that k_{eff} is 0.1 W / m.K.

4. $\dot{Q}_{loss}$ is calculated at $L_S = 100$ mm using the obtained k_{eff} from the previous step. In this step, it was found that $\dot{Q}_{loss}$ is 5.4 W.

5. T_C at $L_s = 100$ mm is calculated at $\dot{Q}_{CC} = 0$. It is found that T_C is 19 ℃.

Based on the result of the calculations and experiments, we can see that a good agreement is obtained between experimental and numerical results.

Figure 4.4 shows T_c as a function of L_s. As can be seen in this figure, T_c decreases as L_s decreases and reaches the lowest value when L_s is 200 mm. Here, the red markers show the experimental results at $L_s = 50$ mm and $L_s = 100$ mm. When L_s equals 50 mm, T_c is 22 ℃, and when L_s equals 100 mm, T_c is 19 ℃.

4.2 A cooler driven by an engine in a straight tube

Swift provided the experimental measured pressure between the ambient heat exchangers P_1 in a straight tube [10]. In order to validate the transfer matrix method used in all components

in the tube, we calculate P_1, T_{H}, T_{C}, and $\dot{Q}_{\mathrm{H}}$ and compare them with the experimental results obtained by Swift [10].

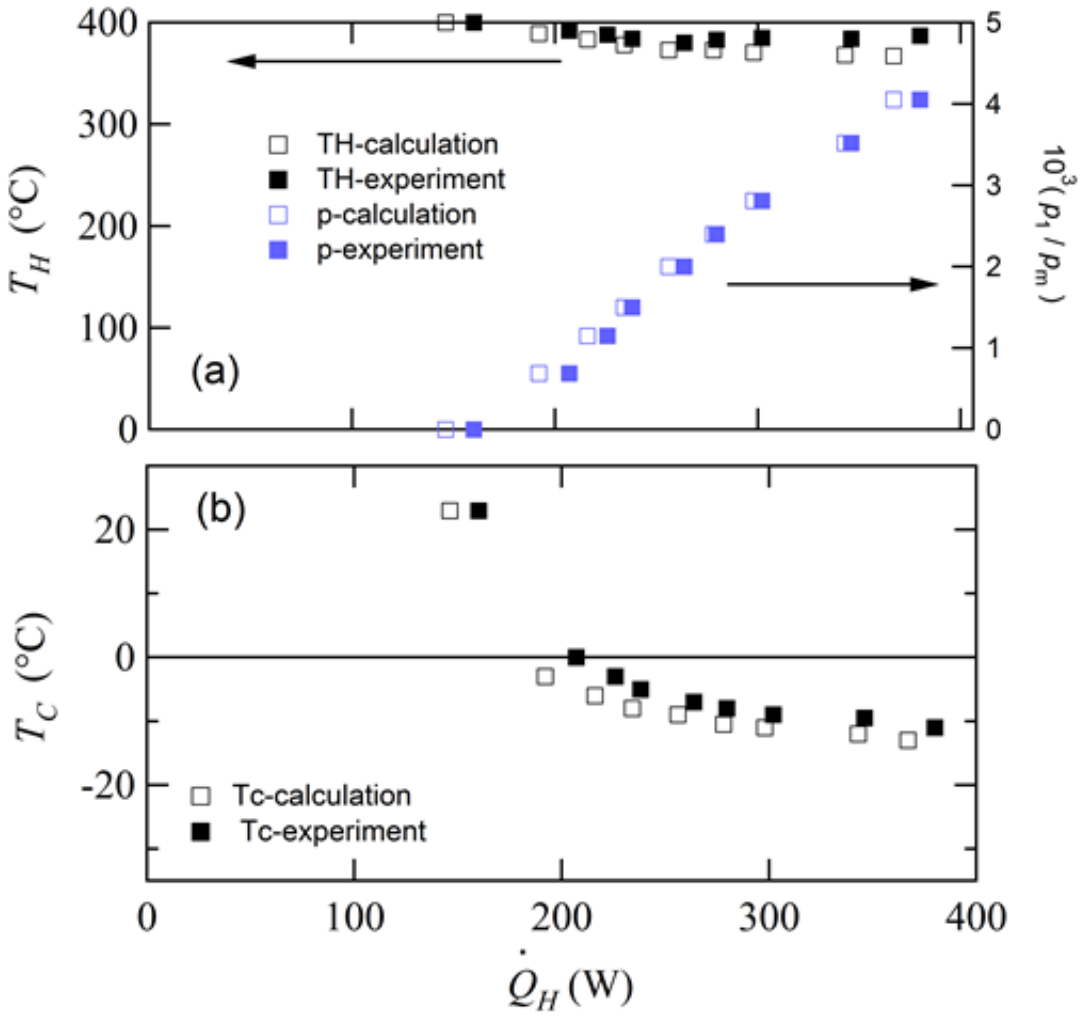

Figure 4.5 (a) T_{H} (b) T_{C} and $10^3(P_1/P_m)^2$ as a function of position $\dot{Q}_{\mathrm{H}}$ in the stack [10]

It should be noted that the length of the stacks is 40 mm, and the length of the tube is 37 cm. One of the end of the tube is open which is connected to the bulb and the other is closed. Moreover, the working gas is helium at 0.1 MPa and T_A is 24 ℃. In addition, the flow channel radius of the stacks is 0.4 mm. In our calculation, the acoustic streaming [34, 42, 43]

and the thermal conduction along the x-axis are neglected for simplicity. As can be seen in Fig. 4.5, the numerically obtained T_{H}, T_{C}, and $\dot{Q}_{\mathrm{H}}$ have a good agreement between numerical and experimental results.

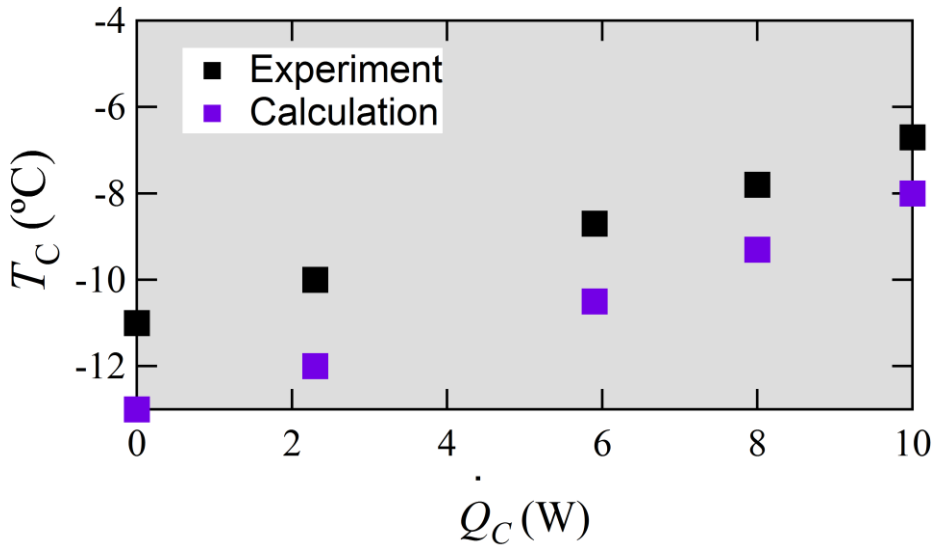

Figure 4.6 $\dot{Q}_c$ as a function of T_C at $\dot{Q}_H$= 380 W [10]

In Fig. 4.6, we show the comparison results between calculation and experiment. In the experiment, the results are shown in the black-square symbols, the effect of the external load $\dot{Q}_c$ imposed to the cold heat exchanger is shown. When $\dot{Q}_c$ is increased from 0 to 10 W, T_c increases from -11 ℃ to -6 ℃. In this figure, the calculation results are shown in the purple-square symbols. As can be seen in this figure, as $\dot{Q}_c$ is increased from 0 to 10 W, T_c rises from -13 ℃ to -8 ℃. As can be seen in this figure, there is a discrepancy between experiment and calculation results. We consider that the discrepancy can be attributed to the minor losses occur in the tube. In the calculation, we did not take into account the effect of minor losses.

4.3 A cooler driven by an engine in a looped tube.

The experimentally measured acoustic field in the looped tube was provided by Yazaki et. al [23]. However, they did not demonstrate the performance. Therefore, in order to show the validation of the present numerical method, pressure and velocity along the looped tube were calculated and compare them with the experimental result obtained by them.

Figure 4.7 shows the numerical results of acoustic field. $|P|$, $|U|$ along the looped tube and Arg (Z) $(= -\theta)$ in the vicinity of engine stack and in the engine stack are denoted by solid lines for the numerical results, while the experimental results denoted by square-solid symbols. It should be noted that the experimental results of their work, the second stack work as a load without ambient and cold heat exchangers. Air is the working gas. In this calculation, the pressure amplitude at the ambient end of the engine stack is set at 1.7 kPa. This is same as the pressure amplitude in their experiment. It should be noted that they plotted the phase difference $\theta(= -Arg\ (Z))$. Figure 4.7 shows that there is a good agreement between the experimental and numerical results.

4.4. Conclusion

This chapter provides the validation of transfer matrices. These transfer matrices were validated using three different configuration of thermoacoustic system. The first is validation with experimental result conducted by Farikhah et.al, the second was validated using experimental results obtained by Swift and the last is validated by comparison with Yazaki's work. Based on those validations, we can see that the calculations of the transfer matrices have a

good agreement with those experimental results.

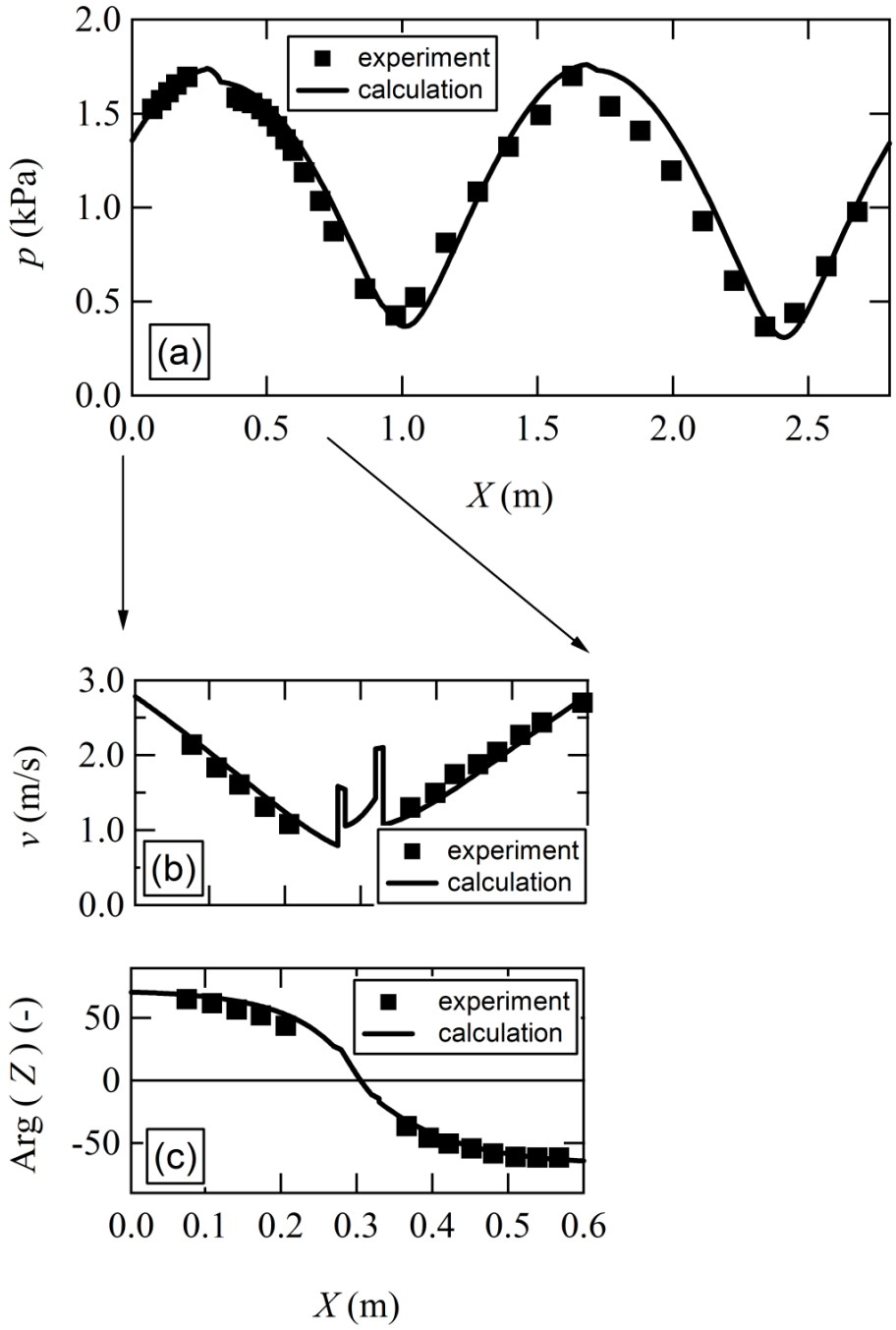

Figure 4.7 $|P|, |U|,$ and Arg (Z) as a function of x [23]

Chapter 5

Optimization of a heat-driven thermoacoustic cooler

In this chapter, we optimize numerically the heat-driven thermoacoustic cooler. In this investigation, we optimize Yazaki's experimental work [23]. This chapter is divided into two sections. In Sec. 5.1, we describe the thermoacoustic energy conversion efficiency. Section 5.2 shows the optimizing results. We consider five optimizing parameters; position, radius of engine, radius of cooler, porosity of engine and porosity of cooler.

5.1 Thermoacoustic energy conversion efficiency

In the optimization, we calculate the efficiency. This efficiency is calculated based on the energy conversion in the engine and cooler stacks. In thermoacoustic, the energy is converted from thermal energy into acoustical energy and conversely. In the case of energy conversion in the engine stack, the energy is converted from thermal into acoustical energy. As a result, the acoustic power could be produced. On the other hand, in the case of energy conversion in the cooler stack, the acoustical energy is converted into the thermal energy. Hence, the cooling power could be produced.

There are some important control parameters. They are normalized absolute value of the impedance $|Z/(\rho a)|$, argument value of the impedance $Arg\ (Z) = -\theta$, radius of the stacks r/δ, and $SWR\ (P_{max}/P_{min})$. Here, ρ is the the density of the gas while a

is the sound speed of the gas. Moreover, θ is the phase difference and δ is the thermal penetration depth which means how far heat and momentum can diffuse laterally during a time interval of the order of the period of the oscillation divided by π [34].

In this calculation, we calculated the second-law efficiency of engine stack $\eta_{2,e}$ as an independent engine stack [see Fig. 5.1] with different input of $|Z/(\rho a)|$ and θ. Moreover, the calculation condition is shown in table 5.1. Here, $\eta_{2,e}$ is defined as follow:

$$\eta_{2,e} = \frac{\eta_e}{\eta_{Carnot}} \tag{5.1}$$

where η_e is the thermal efficiency. Moreover, η_{Carnot} is the thermodynamic upper limit value of η_e. η_e and η_{Carnot} can be defined as follows:

$$\eta_e = \frac{\Delta \dot{W}_e}{\dot{Q}_H} \tag{5.2}$$

$$\eta_{Carnot} = \frac{T_H - T_A}{T_H} \tag{5.3}$$

Here, T_H and T_A are the heating temperature and ambient temperature, respectively. $\Delta \dot{W}_e$ is the acoustic power generated in the stack and $\dot{Q}_H$ is the heating power in the hot end of the stack.

Second-law efficiency of the cooler is denoted by $\eta_{2,c}$. It is expressed as follow:

$$\eta_{2,c} = \frac{COP}{COP_{Carnot}} \tag{5.4}$$

Here, COP stands for Coefficient of Performance and COP_{Carnot} is the thermodynamic upper limit value of COP. They can be defined as follows :

$$COP = \frac{\dot{Q}_c}{\Delta \dot{W}_c} \tag{5.5}$$

$$COP_{Carnot} = \frac{T_C}{T_A - T_C} \tag{5.6}$$

where $\dot{Q}_C$, $\Delta \dot{W}_C$ and T_C are the cooling power, acoustic power consumed by the stack,

and cooling temperature, respectively.

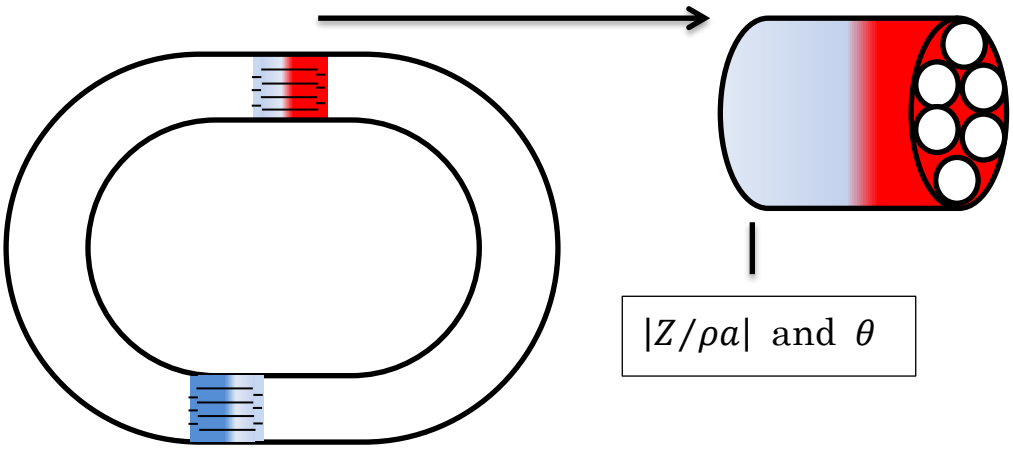

Figure 5.1 The engine stack.

Table 1. The calculation condition of the independent calculation of $\eta_{2,e}$ in the engine stack with different input of $|Z/(\rho a)|$ and θ.

The geometry of the engine stack	
Narrow radius of the stack (r_s)	0.1 mm
Diameter of the stack (D)	40 mm
Length of the stack (L_s)	40 mm
Ambient temperature (T_a)	300 K
Heating temperature (T_H)	700 K
The operating condition	
Gas	Helium
Density (ρ)	4.75 kg/m^3
Sound speed (a)	1032 m/s
Mean pressure (P_m)	3.0 MPa

Figure 5.2 shows the contour plot of the calculated $\eta_{2,e}$. It is shown as a function of θ and $|Z/(\rho a)|$ when T_H is 700 K and r/δ is 1.7 and Figure 5.3 shows it at

$r/\delta = 0.55$. Here, r/δ is the same as the value of $\sqrt{\omega\tau}$. Here, ω is the angular frequency and τ is the thermal relaxation time. As can be seen in Fig. 5.2, the optimum value of $|Z/(\rho a)|$ and θ at $r/\delta = 1.7$ is 6.5 and 83°, respectively.

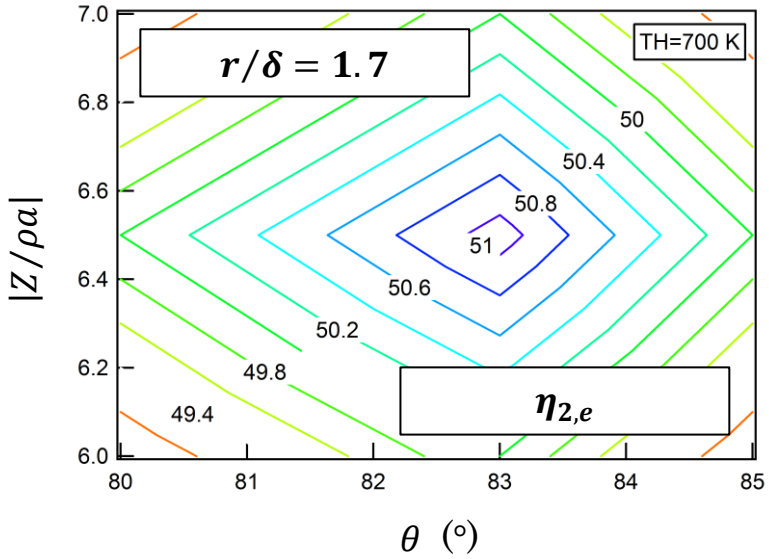

Figure 5.2 $\eta_{2,e}$ as a function of θ and $|Z/\rho a|$ at $r/\delta = 1.7$

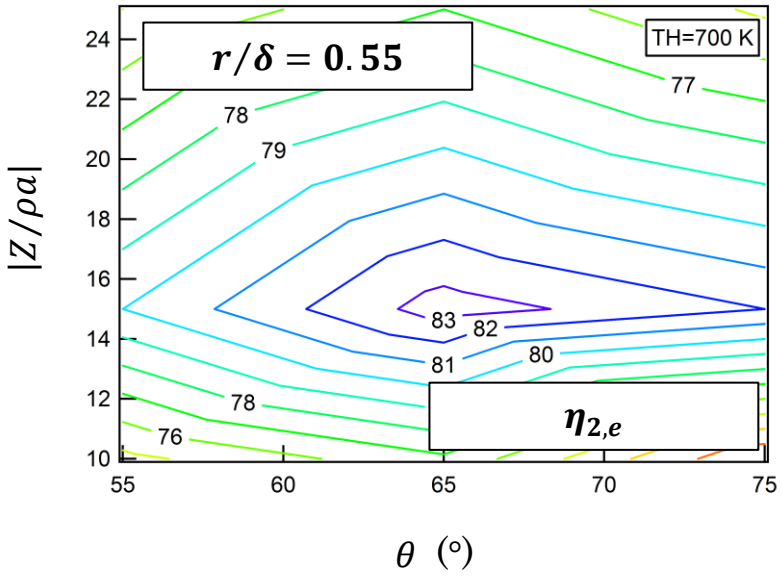

Figure 5.3 $\eta_{2,e}$ as a function of θ and $|Z/\rho a|$ at $r/\delta = 0.55$

In the optimum values, it was found that $\eta_{2,e}$ is 51 % of the upper limit value. On the other hand, as can be seen in Fig. 5.3, the optimum value of $|Z/(\rho a)|$ and θ at $r/\delta = 0.55$ is 15 and 65°, respectively. It was found that $\eta_{2,e}$ reaches 83 % of the upper limit value.

The other controlled parameter is SWR. It stands for standing wave ratio, which defines as the ratio between the maximum pressure amplitude P_{max} and the minimum pressure amplitude, P_{min}. The model of the calculated SWR as a function of I_{min}/I_{max} was calculated using only looped tube without any stacks inside with the length of the tube L_{loop} equals one wave length λ $\left(L_{loop} = \lambda = 2.8\, m\right)$ [see Fig. 5.4]. In the model, the diameter of the tube is 40 mm. The tube is filled with 0.51 MPa of helium gas. The angular frequency ω is 2312 rad. In addition, the ambient temperature is set at 301 K.

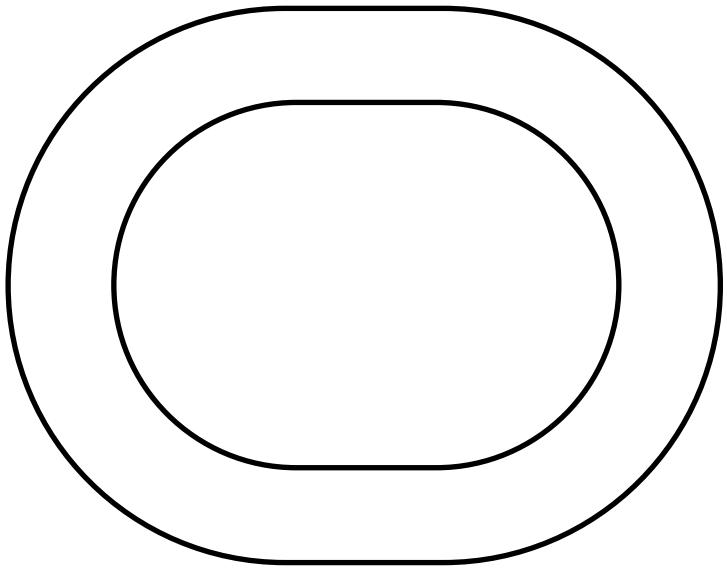

Figure 5.4 the looped tube

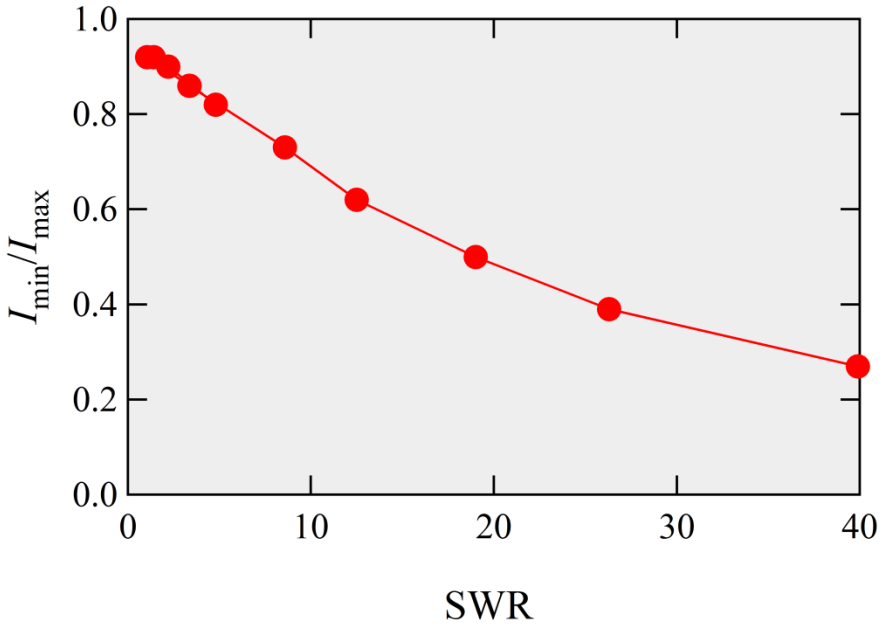

Figure 5.5 SWR as a function of I_{min}/I_{max}

Here, we use $|Z/(\rho a)|$ from 0.25 to 18 as the input parameter with keeping $\theta = 0°$. The varied input $|Z/(\rho a)|$ would result on changing SWR and I_{min}/I_{max}.

Figure 5.5 shows the calculated SWR as a function of I_{min}/I_{max}. Here, I_{min}/I_{max} implies how much acoustic power can be transported efficiently along the tube. If I_{min}/I_{max} is 1, it means the efficiency of the tube is 100 %, which has zero dissipation inside the looped tube. As can be seen in Fig. 5.5, when SWR is increased, I_{min}/I_{max} is dropped. It was found that in the looped tube, I_{min}/I_{max} reaches 0.92 if SWR is 1. It indicates that when SWR is 1 (unity), the acoustic power could be efficiently transported. Therefore, we can say that the optimum SWR is 1 which is 92 % of the acoustic power is transported along the tube.

5.2. Optimization of five parameters.

5.2.1 Optimization of cooler stack position

Yazaki et. al found that there is a dependence of relative position on the efficiency [23]. Therefore, we changed the relative position. In this investigation, the helium gas at 0.51 MPa was used to fill the looped tube. A 0.27 mm radius was set for engine and cooler stacks. A 301 K temperature at ambient end of the stacks and a 2260 rad/s frequency were set. In this investigation, we set the cooling temperature T_c is 251 K.

In this research, the numerical optimization has been done by using thermoacoustic theory proposed by Rott, Swift, and Tominaga [29,33,34,36,38]. We use the configuration constructed by Yazaki et.al [See Fig. 5.6].

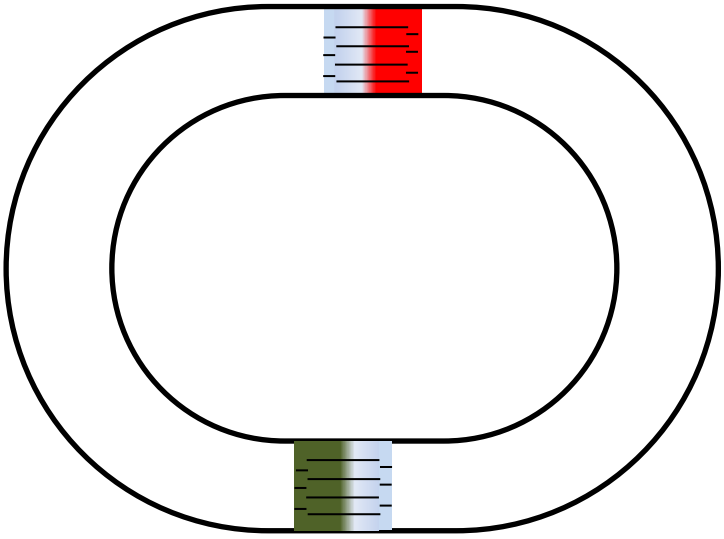

Figure 5.6 Schematics of the heat-driven cooler [23]

In this calculation, we optimize the relative position of the stacks L/L_{loop}.

Second-law efficiency of the engine $\eta_{2,e}$, second-law efficiency of the cooler $\eta_{2,c}$, efficiency of the tube η_{tube} and efficiency total of the whole cooler $\eta_{2,total}$ are evaluated.

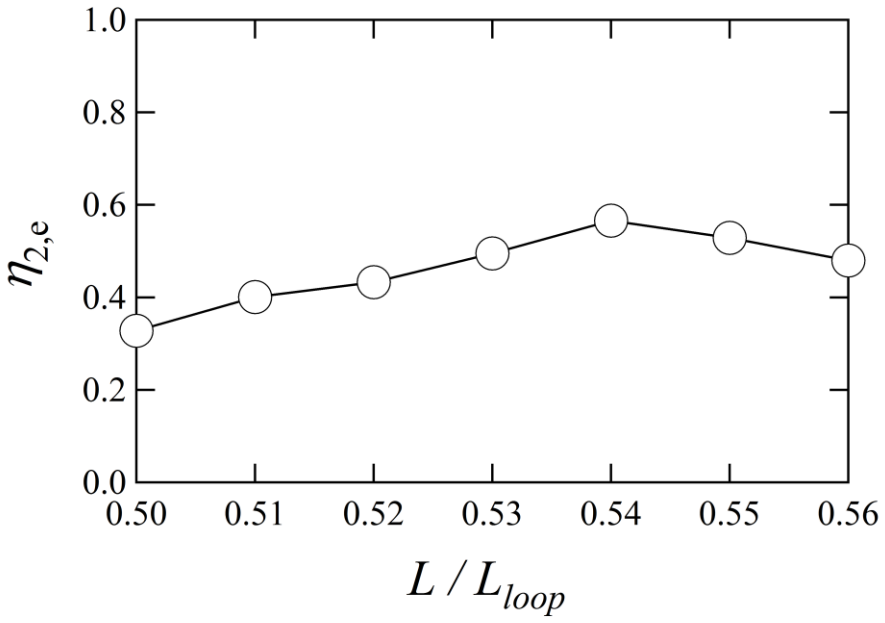

Figure 5.7 L/L_{loop} as a function of $\eta_{2,e}$ [49]

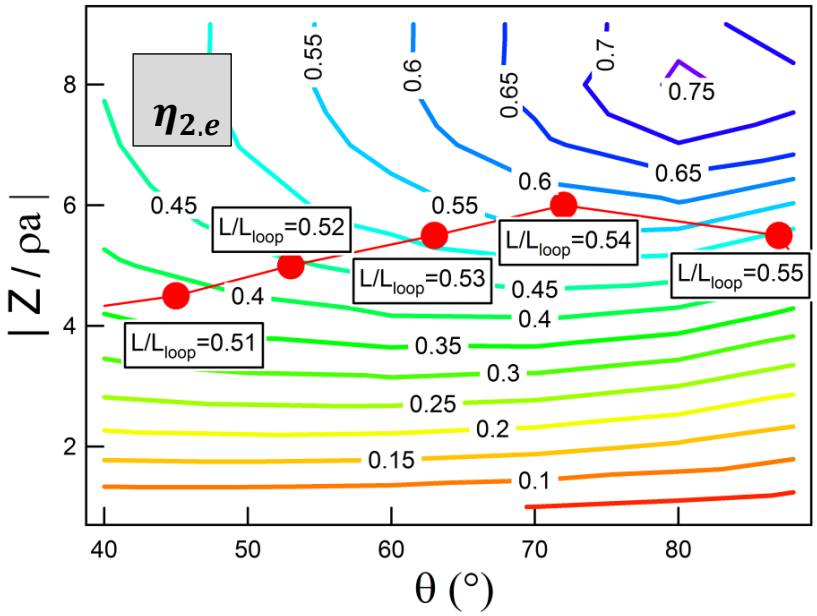

Figure 5.8 $\eta_{2,e}$ as a function of $|Z/(\rho a)|$ and θ

In Figure 5.7, L/L_{loop} is shown as a function of $\eta_{2,e}$. As L/L_{loop} increases from 0.50 to 0.54, $\eta_{2,e}$ rises from 0.32 to 0.57, and at $L/L_{loop} > 0.54$, $\eta_{2,e}$ drops. It means that the optimum value of L/L_{loop} is 0.54. We consider that this result can be attributed to the value of $|Z/(\rho a)|$ and θ. Figure 5.8 shows the contour plot of $\eta_{2,e}$ as a function of $|Z/(\rho a)|$ and θ. The contour plot was calculated under the condition $r_e/\delta = 1.5$ [23] and the heating temperature T_H is 674 K. The contour plot shows that the optimum value of $|Z/(\rho a)|$ and θ is 8 and 80 °, respectively. It was found that the maximum $\eta_{2,e}$ which can be obtained under the condition $r_e/\delta = 1.5$ is 0.75 of the thermodynamical upper limit value. It should be noted that the calculation was performed under the condition of independent stack. In this case, the values do not depends on the acoustic field distribution in the looped tube. In figure 5.8, we also plot $\eta_{2,e}$ as a function of $|Z/(\rho a)|$ and θ under the condition that L/L_{loop} is varied from 0.50 to 0.56. They are shown in the red-closed circle symbols. As can be seen in this figure, the optimum value of $|Z/(\rho a)|$ and θ is 6 and 70°, respectively. It was found when L/L_{loop} is 0.54, $\eta_{2,e}$ reaches 0.57 of thermodynamic upper limit value. This value is 1.8 times higher than the value at $L/L_{loop} = 0.50$. These values are near the optimum values shown in the contour plot. However, there is a discrepancy of the optimum values. These can be attributed to the geometry. In the case of contour plot, $\eta_{2,e}$, $|Z/(\rho a)|$ and θ were calculated with single stack without looped tube. On the other hand, in the case of calculation in the red symbols, $\eta_{2,e}, |Z/(\rho a)|$ and θ were calculated in a looped tube with cooler stack. These values not only depend on the engine stack but also these depend on the geometry of looped tube and the cooler stack. Nevertheless, the discrepancy is only 11 % of the maximum $\eta_{2,e}$. Therefore, we can say that the reason behind the obtaining of the optimum value of L/L_{loop} at 0.54 is due to

the optimum value of $|Z/(\rho a)|$ and θ is obtained in the near of optimum values showed in the contour plot.

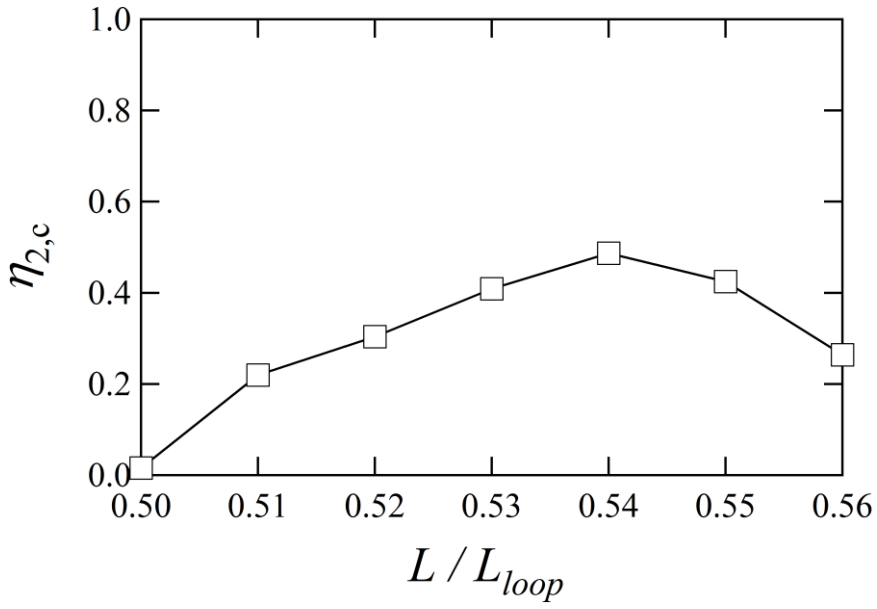

Figure 5.9 L/L_{loop} as a function of $\eta_{2,c}$ [49]

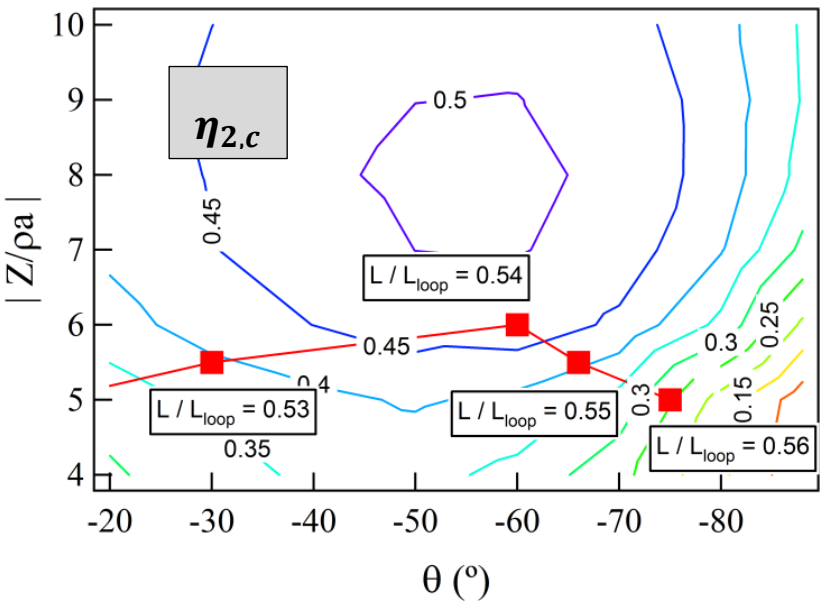

Figure 5.10 $\eta_{2,c}$ as a function of $|Z/(\rho a)|$ and θ

Figure 5.9 shows $\eta_{2,c}$ as a function of L/L_{loop}. It shows that the optimum L/L_{loop} is 0.54. This value is 96 times higher than that of at $L/L_{loop} = 0.50$. At the optimum value, $\eta_{2,c}$ is 0.48 of thermodynamical upper limit value.

We consider that the reason for the existence of the optimum value is shown in Figure 5.10. This figure shows the contour plot of $\eta_{2,c}$ as a function of $|Z/(\rho a)|$ and θ. This contour plot was calculated under the condition $r/\delta = 1.5$ and the cooling temperature $T_c = 251\,K$. The contour plot shows that the optimum value of $|Z/(\rho a)|$ and θ is 8 and -55 °, respectively. It was found that the maximum $\eta_{2,c}$ which can be obtained under the condition $r_e/\delta = 1.5$ is 0.50 of the thermodynamical upper limit value. It should be noted that the calculation was performed under the condition of independent stack. In this case, the values do not depend on the acoustic field distribution in the looped tube. In figure 5.10, we also plot $\eta_{2,c}$ as a function of $|Z/(\rho a)|$ and θ under the condition that L/L_{loop} is varied from 0.50 to 0.56. They are shown in the red-closed square symbols. As can be seen in this figure, the optimum values of $|Z/(\rho a)|$ and θ are 6 and -60°, respectively. They were found when L/L_{loop} is 0.54, $\eta_{2,c}$ is 0.48 of thermodynamical upper limit value. These values are near the optimum values shown in the contour plot. However, there is a discrepancy of the optimum values. These can be attributed to the geometry. In the case of contour plot, $\eta_{2,c}$ $|Z/(\rho a)|$ and θ were calculated with single stack without looped tube. On the other hand, in the case of calculation in the red symbol, $\eta_{2,c,}$ $|Z/(\rho a)|$ and θ were calculated for the cooler stack inside the looped tube having an engine stack. These values not only depend on the cooler stack but also depend on the geometry of looped tube and the engine stack. Nevertheless, the discrepancy is only 4 % of the

maximum $\eta_{2,c}$. Therefore, we can say that the reason behind the obtaining of the optimum value of L/L_{loop} at 0.54 is because the optimum value of $|Z/(\rho a)|$ and θ obtained in this geometry is near to the optimum values obtained by using only one engine stack.

Figure 5.11 shows η_{tube} as a function of L/L_{loop}. Here, η_{tube} can be defined as follow:

$$\eta_{tube} = \frac{\Delta \dot{W}_C}{\Delta \dot{W}_e} \tag{5.1}$$

Unlike $\eta_{2,e}$ and $\eta_{2,c}$, when L/L_{loop} rises from 0.50 to 0.56, η_{tube} monotonically drops from 0.46 to 0.21. The optimum value is at $L/L_{loop} = 0.50$. However, it is not good to set the configuration at the position because at $L/L_{loop} = 0.50$, $\eta_{2,e}$ and $\eta_{2,c}$ would become substantially low. As a consequence, $\eta_{2,total}$ becomes low.

Here, Standing Wave Ratio (SWR) is introduced to consider the dependence of η_{tube} on L/L_{loop}. SWR is P_{max}/P_{min}. Here, P_{max} and P_{min} are the maximum and minimum values of the pressure amplitude in the looped tube. As we can see in Fig. 5.12 shown in blue-circle symbols, SWR rises gradually and become far from unity when L/L_{loop} increases from 0.50 to 0.56. When SWR is near unity, it means that the travelling wave like field occur in the looped tube. As a result, the acoustic power could be transported efficiently. On the other hand, when SWR is far from unity, the standing wave like field would occur in the looped tube. It indicates that the acoustic power could not be transported efficiently. Figure 5.12 indicates that as L/L_{loop} is increased the standing wave like field would occur in it. Moreover, as we showed and mentioned before [see Fig. 5.5], the highest I_{min}/I_{max} was obtained when SWR is unity (1). Here, I_{min}/I_{max} corresponds to η_{tube}. As we can see in the blue symbols, which show the calculated results of η_{tube} as a function of L/L_{loop}, the highest η_{tube} is obtained

when SWR is 6. This value is nearer unity compared to the others. It was found that η_{tube} reaches 0.46. This value is lower than the optimum value found in the red symbols. It is happened because in the blue symbols the calculated η_{tube} and SWR are calculated under the condition that two stacks inside the looped tube. On the other hand, in the red symbol, the calculated I_{min}/I_{max} and SWR are calculated under the condition that there are no stacks inside the looped tube. Nevertheless, the optimum values obtained in the blue symbol is near to the optimum value in the red symbol.

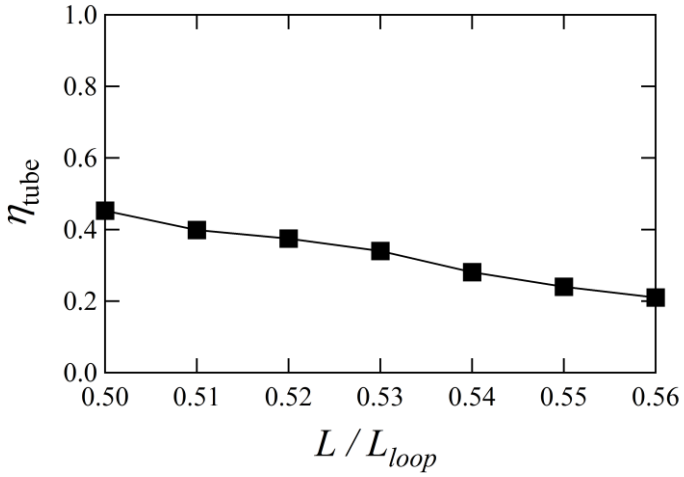

Figure 5.11 η_{tube} as a function of L/L_{loop} [49]

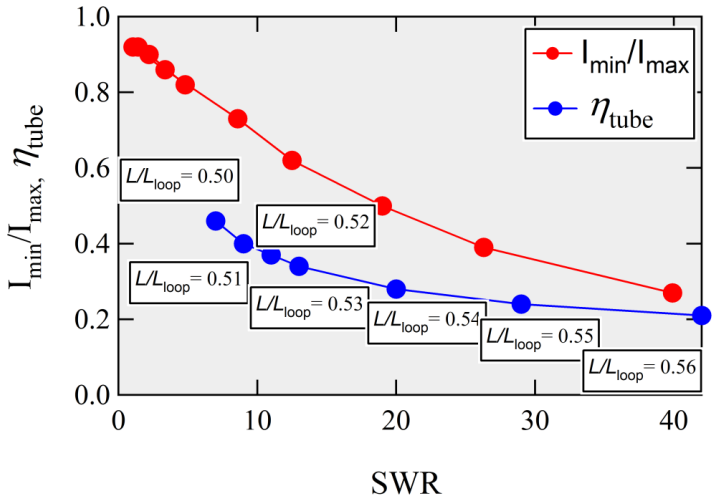

Figure 5.12 SWR as a function of I_{min}/I_{max}, η_{tube} [49].

Here, the total efficiency of the whole cooler is denoted as $\eta_{2,total}$ which is defined as

$$\eta_{2,total} = \frac{COP_{total}}{\eta_{Carnot,total}} \quad 5.2$$

where COP_{total} and $\eta_{Carnot,total}$ are defined as follows:

$$COP_{total} = \frac{\dot{Q}_C}{\dot{Q}_H} \quad 5.3$$

$$\eta_{Carnot,total} = \eta_{Carnot}.COP_{Carnot} \quad 5.4$$

$\eta_{2,total}$ also can be expressed as

$$\eta_{2,total} = \eta_{2,e}.\eta_{2,c}.\eta_{tube} \quad 5.5$$

When L/L_{loop} increases from 0.50 to 0.54, the total efficiency of the cooler $\eta_{2,total}$ increases [see Fig. 5.13]. On the other hand, when L/L_{loop} decreases from 0.54 to 0.56, it drops. It was found that the optimum value of $\eta_{2,total}$ reaches 0.08 of the total thermodynamic upper limit value. It means that $\eta_{2,total}$ is 85 times larger than the values of $\eta_{2,total}$ at $L/L_{loop} = 0.50$. This means that there is a dependence of relative position on the performance of the system.

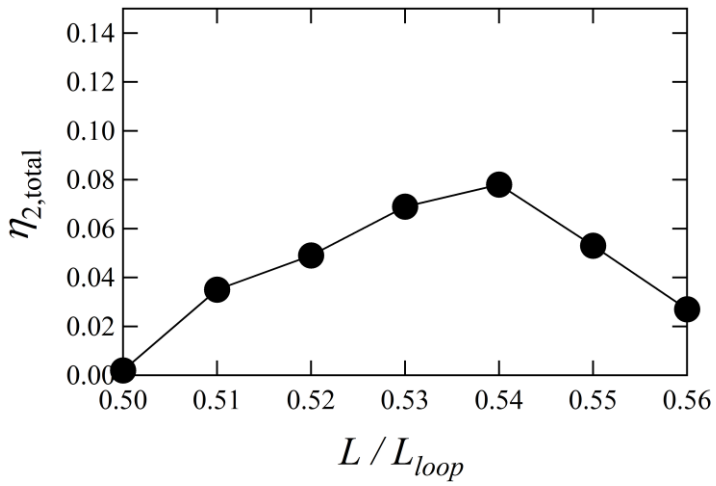

Figure 5.13 L/L_{loop} as a function of $\eta_{2,total}$ [49]

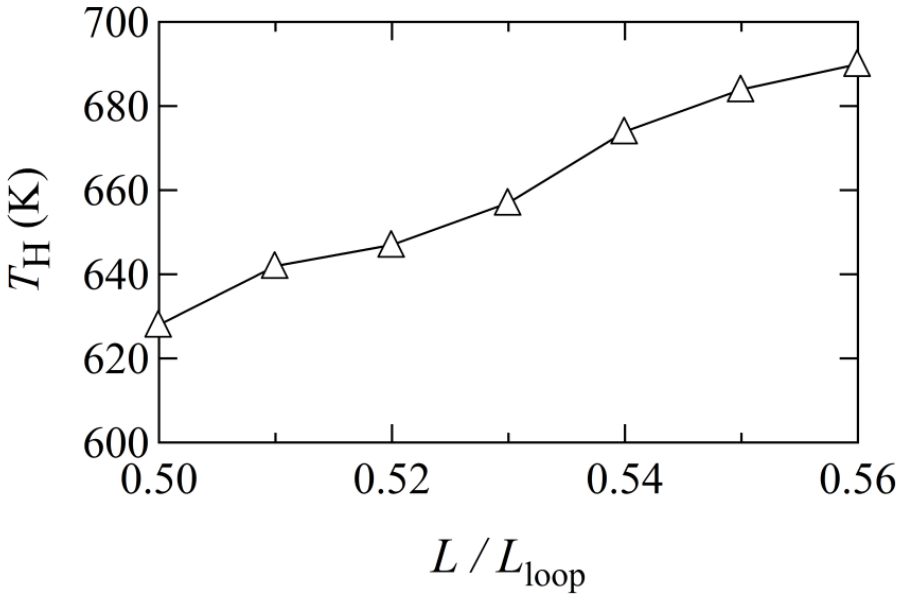

Figure 5.14 T_H as a function of L/L_{loop} [49]

In Figure 5.14, the calculated hot temperature in the engine stack T_H is shown as a function of L/L_{loop}. When L/L_{loop} is increased from 0.50 to 0.56, T_H is also increased from 628 K to 690 K. However, setting the stack position at $L/L_{loop} = 0.50$ is not good due to the low value of the efficiencies.

5.2.2 Optimization of radius of engine and cooler Stacks

In this calculation, L/L_{loop} is set at 0.54, which is the optimum value obtained in the previous optimization. As shown in contour plot of Figure 5.15, when r_e/δ and r_c/δ are reduced, $\eta_{2,total}$ increases. It was found that the optimum value of r_e/δ and r_c/δ is 0.96 and 1.06, respectively and the value of $\eta_{2,total}$ is 0.10 of the thermodynamic upper limit.

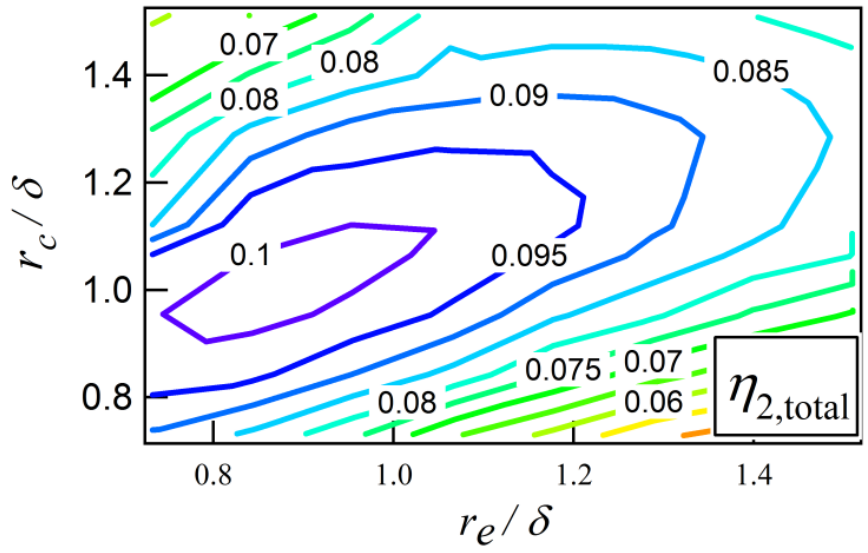

Figure 5.15 $\eta_{2,total}$ as a function of r_e/δ and r_c/δ [49]

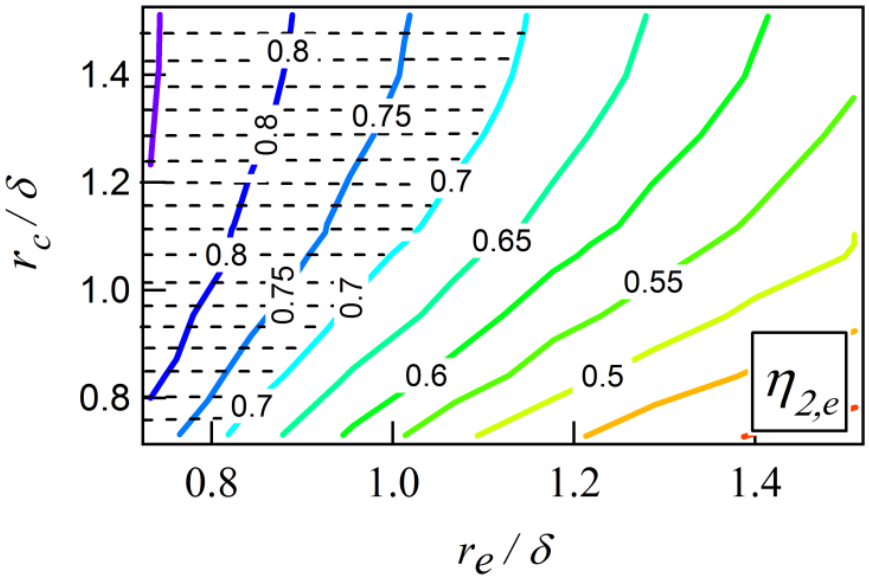

Figure 5.16 $\eta_{2,e}$ as a function of r_e/δ and r_c/δ [49]

$\eta_{2,total}$ can be divided into three parts; $\eta_{2,e}$, $\eta_{2,c}$ and η_{tube}. Figure 5.16 shows that $\eta_{2,e}$ increases when r_e/δ is decreased. In addition, as can be seen in this figure, there is a hatched-area which means that $\eta_{2,e}$ obtained in this calculation is comparable to that of the most efficient thermoacoustic engine [42, 47].

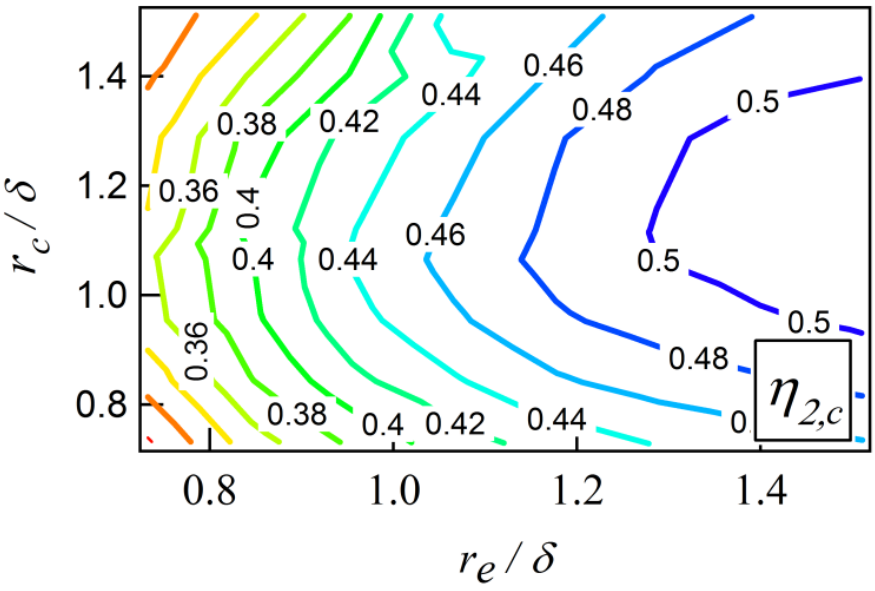

Figure 5.17 $\eta_{2,c}$ as a function of r_e/δ and r_c/δ [49]

As shown in Fig. 5.17, $\eta_{2,c}$ increases when r_e/δ is increased. It means that there is an opposite dependence between $\eta_{2,e}$ and $\eta_{2,c}$ on r_e/δ. In order to consider the reason for the opposite dependence, $|Z/(\rho a)|$ is calculated at the engine and cooler stack.

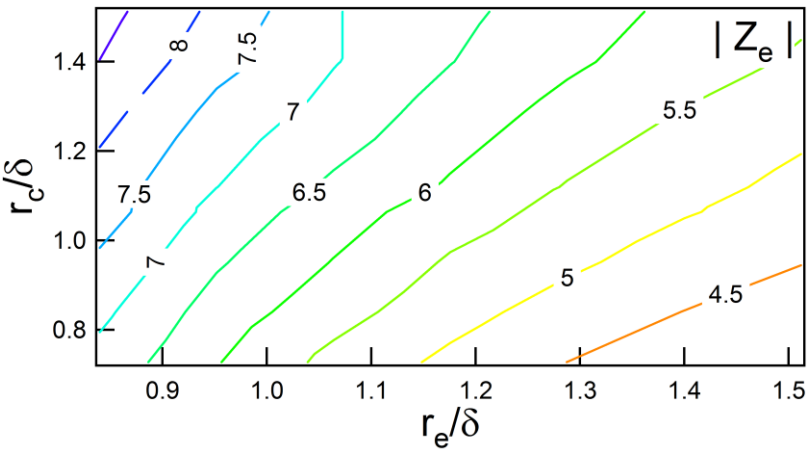

Figure 5.18 $|Z_e/(\rho_e a_e)|$ as a function of r_e/δ and r_c/δ

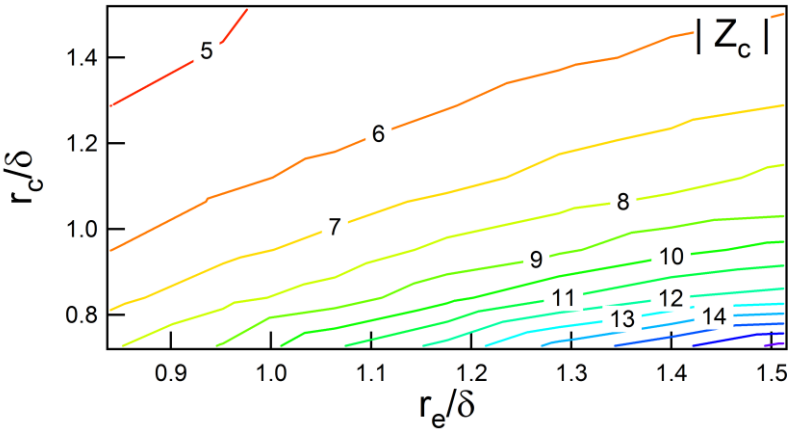

Figure 5.19 $|Z_c/(\rho_c a_c)|$ as a function of r_e/δ and r_c/δ

As can be seen in Figs. 5.18, in the engine stack when r_e/δ is decreased, $|Z_e/(\rho_e a_e)|$ becomes high. In the cooler stack, conversely, as shown in Fig. 5.19, when r_e/δ is decreased, $|Z_c/(\rho_c a_c)|$ becomes low. Therefore, the opposite dependence is exist.

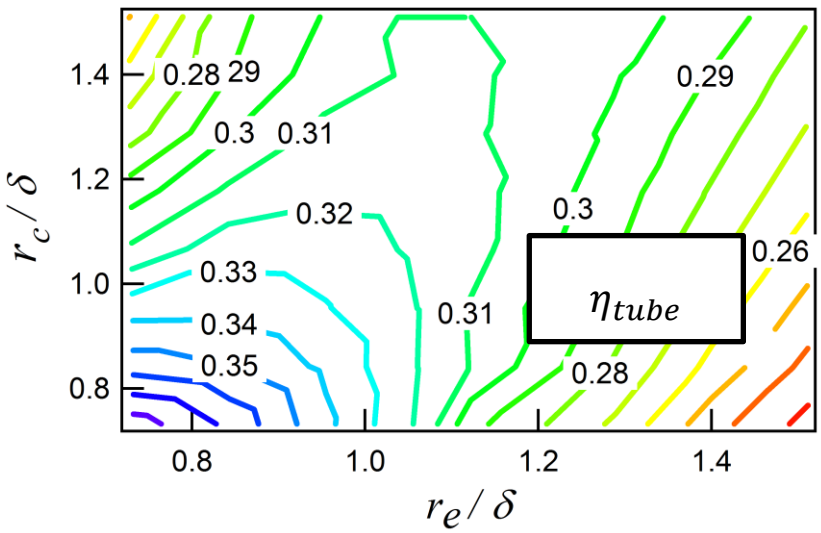

Figure 5.20 η_{tube} as a function of r_e/δ and r_c/δ

Figure 5.20 shows the contour plot of η_{tube} as a function of r_e/δ and r_c/δ. As can be seen in the figure, as r_e/δ and r_c/δ decreased, η_{tube} becomes high.

Eventually, at the optimum value, which $r_e/\delta = 0.96$ and $r_c/\delta = 1.06$, $\eta_{2,e}$, $\eta_{2,c}$, η_{tube} are 0.70, 0.44 and 0.33, respectively.

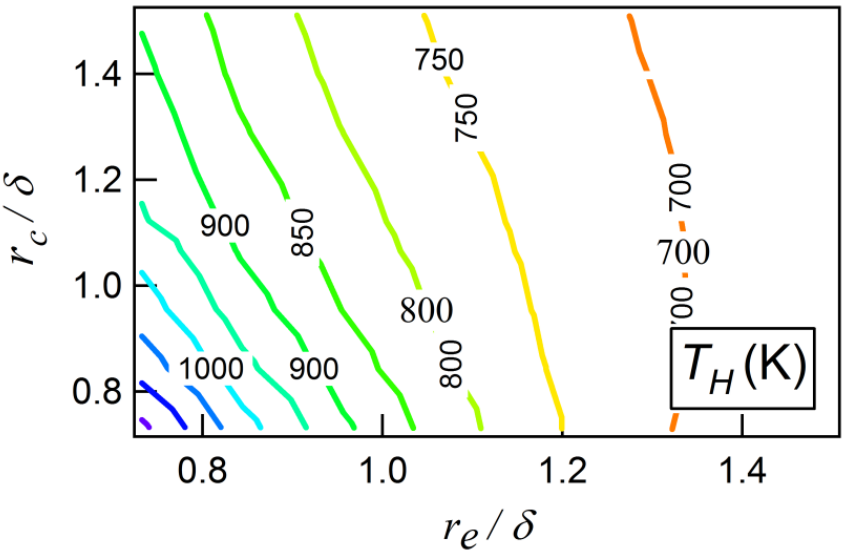

Figure 5.21 T_H as a function of r_e/δ and r_c/δ

T_H is shown in Fig. 5.21. As r_e/δ and r_c/δ decreased, T_H becomes high. It indicates that the proper r_e/δ and r_c/δ are important to utilize waste heat.

5.2.3 Optimization of engine and cooler porosities

According to the previous result, η_{tube} is low compared with $\eta_{2,e}$ and $\eta_{2,c}$. Hence, it is important to improve η_{tube}. We consider that increasing mean pressure P_m and porosity of engine and cooler could increase η_{tube}.

In the previous optimization, we performed the numerical calculation under the condition that P_m is 0.51 M.Pa. In this section, the porosities are optimized under the

condition that $P_m is\ 3.0\ MPa$. Moreover, we also increase the porosities.

To obtain the optimum porosities, we selected porosity of engine and cooler from 0.77 to 1.7, where it is defined as a ratio of the sum of the areas of the narrow circular tubes composing stacks and the cross-sectional area of the looped tube [See Fig. 5. 22]. It can be expressed as

$$Porosity\ = \frac{A_s.n}{A_{tube}} = \frac{A_s + A_s + A_s + A_s + \cdots}{A_{tube}} \qquad 5.6$$

where A_s is the cross-sectional area of narrow circular tube composing stacks, n is the number of the narrow circular area, and A_{tube} is the cross-sectional area of the looped tube [see Fig. 5.22].

In Fig. 5.23, the contour plot of $\eta_{2,total}$ calculated under the condition $L/L_{loop} = 0.54$, $r_e/\delta = 0.96$ and $r_c/\delta = 1.06$, which are the optimum value of L/L_{loop}, r_e/δ, and r_c/δ. This figure shows that a high $\eta_{2,total}$ is obtained at porosities=1.3. The condition porosities=1.3 implies that the engine and cooler stacks would work well if the total area of the stacks is slightly larger than that of the tube (see Fig.5. 22). In the optimum values, $\eta_{2,total}$ reaches 0.24 of the thermodynamic upper limit value. This value is three times higher than that of porosity of Yazaki's experimental set up.

Figure 5.24 and 5.25 show the contour plot of $\eta_{2,e}$ and $\eta_{2,c}$ as a function of engine and cooler porosities. As can be seen in Fig. 5.24, when the engine porosity is increased and the cooler porosity is decreased, $\eta_{2,e}$ is improved. Conversely, as shown in Fig. 5.25, $\eta_{2,c}$ is improved when the engine porosity is decreased and the cooler porosity is increased.

$\eta_{2,e}$ and $\eta_{2,c}$ becomes 0.78 and 0.44 of the thermodynamic upper limit value when the porosities are 1.3.

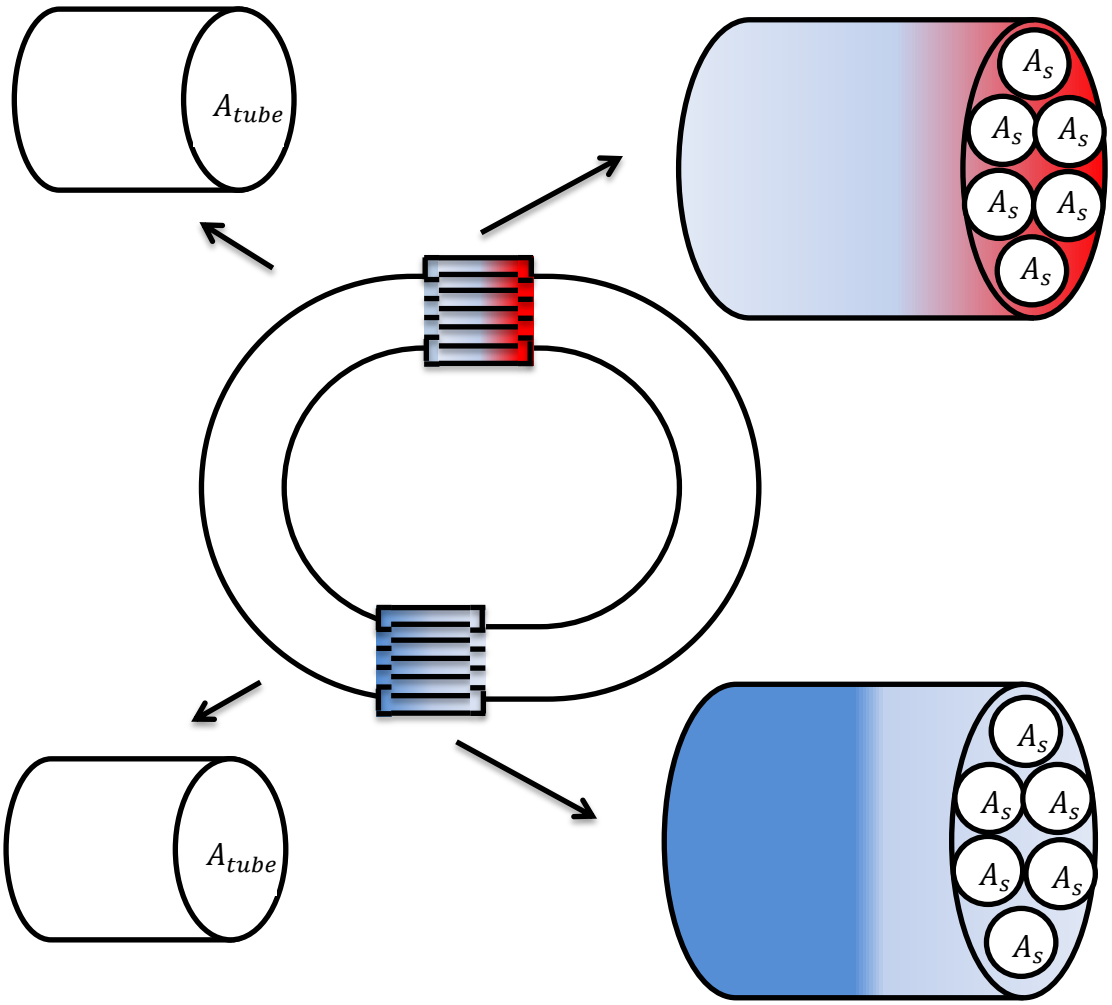

Figure 5.22 Schematics of the heat-driven cooler with the optimum porosities

Figure 5.26 shows that η_{tube} is increased from 0.44 to 0.70 of the upper limit value when the porosities is increased from 0.77 to 1.3. It means that there is a considerable improvement of η_{tube} by increasing the porosities at 1.3. Therefore, we can say that the porosities is the important parameter for increasing the efficiency.

Compared to the results of optimization of radius of engine and cooler at $P_m = 0.51\ MPa$, using $P_m = 3.0\ MPa$ and with similar porosities at 0.77, $\eta_{2,e}$ and $\eta_{2,c}$ are remains constant. Likewise, with $P_m = 3.0\ MPa$, increasing porosities from 0.77 to 1.3 do not give any effect on

$\eta_{2,e}$ and $\eta_{2,c}$. However, when P_m is increased from 0.51 MPa to 3.0 MPa, with keeping same porosities at 0.77, η_{tube} rises from 0.33 to 0.44. Further, with keeping mean pressure at 3.0 MPa, increasing porosities from 0.77 to 1.3, η_{tube} rises from 0.44 to 0.70. It means that increasing P_m and porosities have a huge impact on increasing η_{tube}. As a result, $\eta_{2,total}$ is improved.

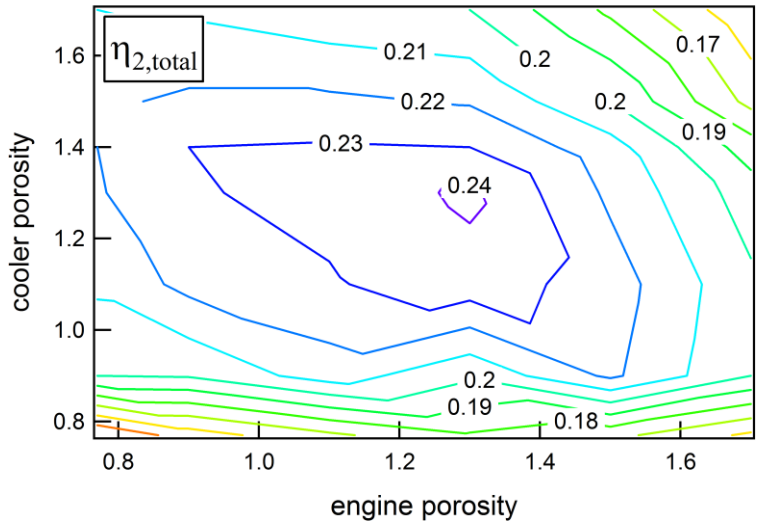

Figure 5. 23 contour plot of $\eta_{2,total}$ as a function of engine and cooler porosities

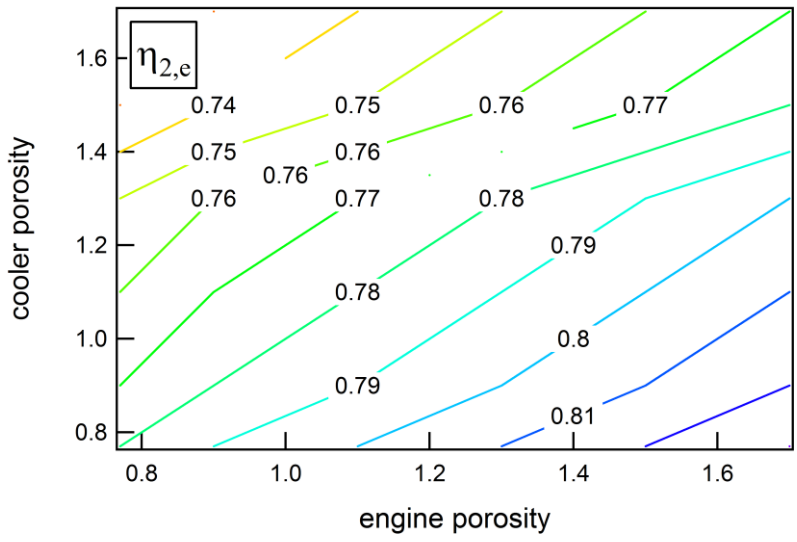

Figure 5. 24 contour plot of $\eta_{2,e}$ as a function of engine and cooler porosities

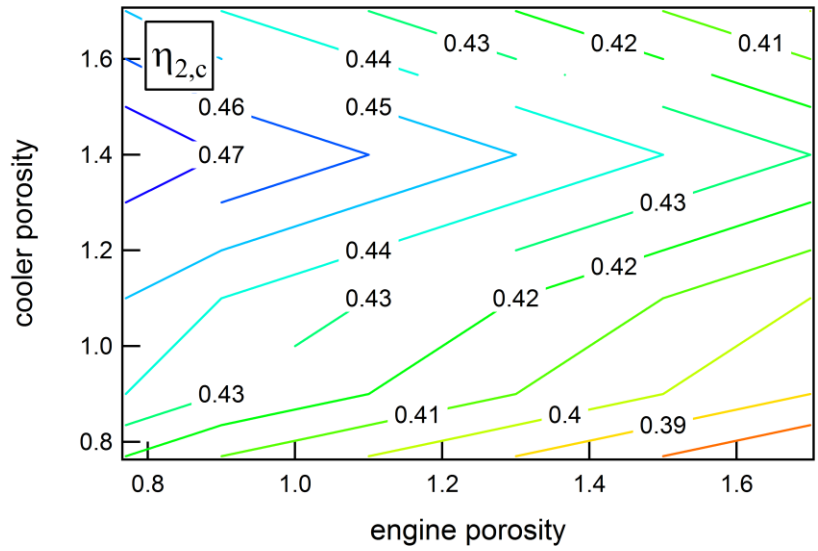

Figure 5. 25 contour plot of $\eta_{2,c}$ as a function of engine and cooler porosities

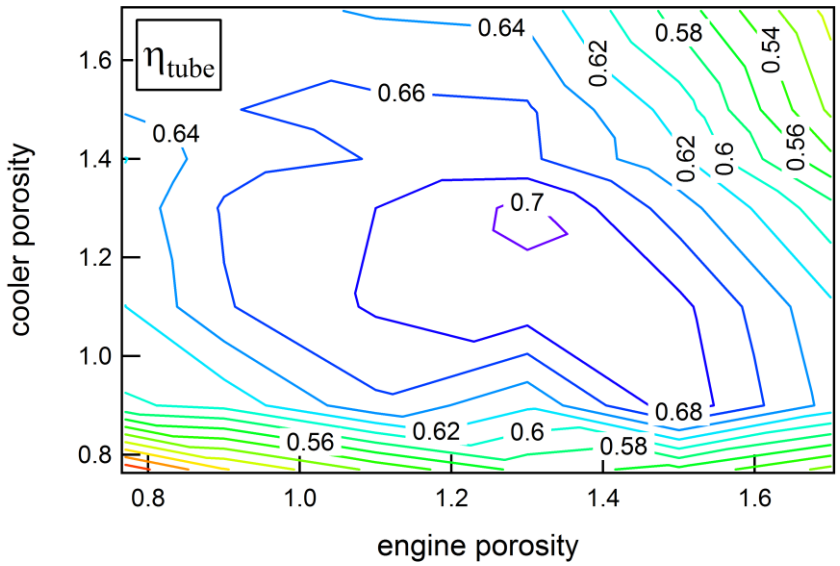

Figure 5. 26 contour plot of η_{tube} as a function of engine and cooler porosities

In this optimization, we did three cycle of the optimization. Table 5.2 shows them. As can be seen in the table, there are five parameters were optimized; L/L_{loop}, T_C, r_e/δ, r_c/δ, engine porosity and cooler porosity.

Table 5.2 Three cycle optimization

		$\frac{L}{L_{loop}}$	$\frac{r_e}{\delta}$	$\frac{r_c}{\delta}$	Engine porosity	Cooler porosity	$P_m(MPa)$	$\eta_{2,total}$
$C_1(cycle\ 1)$	a	**0.54**	1.5	1.5	0.77	0.77	0.51	0.08
	b	0.54	**0.96**	**1.06**	0.77	0.77	0.51	0.10
	c	0.54	0.96	1.06	**1.3**	**1.3**	3	0.24
$C_2\ (cycle\ 2)$	a	**0.54**	0.96	1.06	1.3	1.3	3	0.24
	b	0.54	**0.96**	**1.06**	1.3	1.3	3	0.24
	c	0.54	0.96	1.06	**1.3**	**1.3**	3	0.24
$C_3(cycle\ 3)$	a	**0.54**	0.96	1.06	1.3	1.3	3	0.24
	b	0.54	**0.96**	**1.06**	1.3	1.3	3	0.24
	c	0.54	0.96	1.06	**1.3**	**1.3**	3	0.24

As we can see in the table, in the cycle 1.a, the optimization of L/L_{loop} is performed with changing the position of the cooler from 0.50 to 0.56. In this cycle, r/δ_e, r/δ_c, porosity of the engine, porosity of the cooler and P_m are kept constant. It was found that $\eta_{2,total}$ is 0.08 of the total Carnot efficiency. Further, in the cycle 1.b, the simultaneous optimization is performed with changing the engine and cooler radii simultaneously. We also keep other parameters as a constant. As a result, we found that $\eta_{2,total}$ becomes 0.10 of the total Carnot efficiency. Later on, in the cycle 1.c, the

engine and cooler porosities are optimized with keeping others as constant. It was found that $\eta_{2,total}$ becomes 0.24 of the total Carnot efficiency. We also perform optimization for the cycle 2 and 3. We found that the optimum values are still same and the values of $\eta_{2,total}$ is also similar with the cycle 1.

It was found that the optimum values of L/L_{loop}, r_e/δ, r_c/δ, engine porosity and cooler porosity are 0.54, 0.96, 1.06, 1.3 and 1.3, respectively. In addition, It was found that $\eta_{2,total}$ reaches 0.24 of upper limit value [50].

5.3 Conclusion

The optimization was performed using five parameters. They are relative position of the cooler, radius of engine and cooler stacks, and porosity of them. It was found that the optimum relative position of the cooler stack is 0.54, the optimum radius of engine and cooler are 0,96 and 1.06, respectively, and the optimum porosities are 1.3. Moreover, at the optimum values, we found the total efficiency is 0.24 of the upper limit value.

Chapter 6

Calculation of the energy conversion efficiency of a stacked-screen regenerator using thermoacoustic theory

According to the results mentioned in the previous chapter (Chapter 5), the optimum value of r_e/δ and r_c/δ are 0.96 and 1.06. at 3 MPa of helium. The radii of them are 0.070 mm and 0.078 mm, respectively.

In thermoacoustic theory [51], the basic equation of hydrodynamics is sorted out based on several assumptions, analysing the stacks as an energy converter [52]. One of the assumptions is the flow path in the stack is uniform. However, the real uniform flow path stacks is not available in those sizes because they are very small. The real uniform flow path stacks is usually larger than 0.3 mm. The only one solution is using wire screen mesh stacks which have many variation of very small flow channel radius ($< 0.3\ mm$). We call these stacks as stacked-screen regenerators. Therefore, we need to use these regenerators instead of the ordinary stacks. However, the flow channel radii are non-uniform. Hence, it is important to calculate the energy conversion efficiency using the regenerators. Thus, in this chapter, we will focus on how to calculate energy conversion using a stacked-screen regenerator having non-uniform (complex) flow path area.

6. 1. Transfer Matrix for complex flow path

In 2009, Ueda et. al experimentally measured the velocity amplitude in the stack and modelled the complex flow path into the uniform flow path. Ueda et. al proposed an experimental formula on ''equivalent flow path diameter''[51]. Obayashi et. al. measured the viscous loss depending on the velocity amplitude in the stack and proposed an empirical formula [52] proposed by Tanaka and the above-mentioned Ueda's experimental formula [53]. Later, we will call this empirical formula the expression of Tanaka-Ueda-Obayashi (TUO).

In 2012, Obayashi et. al [53] measured the attenuation of acoustic power $\dot{W}$ occurred in the stacked-screen regenerator. They measured P and U between the regenerator. Their experiment results conducted under a condition that $dT_m/dx = 0$. It was found that the attenuation factor of the acoustic power is

$$\frac{dW}{dx} = \frac{-A_1}{2}\left(\frac{0.8\rho_m}{d_h}|U| - Im\left[\frac{\omega\rho_m}{1-\chi_v}\right]\right)|U|^2 \tag{6.1}$$

Here, d_h is the hydraulic diameter. To get the d_h, we can obtain the value if the thin wire diameter that forms the regenerator d_{wire} and the radii of the regenerator r are known. The formula is written as

$$r = \frac{\sqrt{d_h d_{wire}}}{2} \tag{6.2}$$

In the case of acoustic power production or consumption along the regenerator length dW/dx, it can be defined as follow

$$\frac{dW}{dx} = \frac{A}{2}\left(Re\left[\frac{dP}{dx}\tilde{U}\right] + Re\left[\tilde{P}\frac{dU}{dx}\right]\right) \tag{6.3}$$

In the experiment, $dU/dx = 0$, so equation 6.3 becomes

$$\frac{dW}{dx} \sim \frac{A}{2}\left(Re\left[\frac{dP}{dx}\widetilde{U}\right]\right) = \frac{A}{2}\left(Re\left[\frac{dP}{Udx}\right]\right)|U|^2 \qquad 6.4$$

By comparing equation 6.1 and 6.4, the equation becomes

$$\mathrm{Re}\left[\frac{dP}{U\,dx}\right] \sim -\frac{0.8\rho_m}{d_h}|U| + Im\left[\frac{\omega\rho_m}{1-\chi_v}\right] \qquad 6.5$$

and using eq. 2.13 (chapter 2), eq. 6.5 can be written as follow

$$Re\left[\frac{dP}{U\,dx}\right] = Im\left[\frac{\omega\rho_m}{1-\chi_v}\right] \qquad 6.6$$

To sum up, we can say that by adding a real number $-\frac{0.8\rho_m}{d_h}|U|$, the velocity inside the regenerator increase.

Here, the experimental results can be incorporated into numerical calculations. Therefore, In the layer metal mesh regenerator, instead of eq.2.13, the following equation is used for the complex flow path

$$\frac{dP}{dx} = -\left(\frac{i\omega\rho_m}{1-\chi_v} + \frac{0.8\rho_m}{d_h}|U|\right)U \qquad 6.7$$

In the case of flow path, a continuous formula that can be written as eq. 2.14, It is necessary to examine whether it can be used inside the complex flow path. Hasegawa et al [54] measured the amount of heat carried by the oscillating flow in a complex flow path (stacked-screen regenerator) when the velocity amplitude $|U|$= 2 m/s using atmospheric air in the experiment. The results show that the theoretical value has a good agreement with the experimental result.

Here, it is important to modify the transfer matrix. Thus, the new transfer matrix can be written as follows [53, 55]:

$$\begin{pmatrix} P_{l+1} \\ U_{l+1} \end{pmatrix} = \begin{pmatrix} P_l \\ U_l \end{pmatrix} + \Delta x \begin{pmatrix} b_{11} & b_{12} \\ b_{21} & b_{22} \end{pmatrix}_l \begin{pmatrix} P_l \\ U_l \end{pmatrix} \qquad 6.8$$

$$b_{11} = 0 \qquad 6.9$$

$$b_{12} = -\frac{i\omega\rho_m}{1-\chi_v} - \frac{0.8\rho_m}{d_h}|U|$$

$$b_{21} = -\frac{i\omega[1+(\gamma-1)\chi_\alpha]}{\gamma P_m}$$

$$b_{22} = \frac{\chi_\alpha - \chi_v}{(1-\chi_v)(1-\sigma)}\frac{1}{T_m}\frac{\Delta T_m}{\Delta x}$$

6. 2. Validation between Calculation and experimental result of Obayashi

Obayashi et al installed a stacked-screen regenerator with a temperature difference ΔT at both ends in the oscillating flow field and the acoustic power is measured. It was found that the acoustic power before and after the regenerator changed. It changed because of the velocity amplitude. It indicates that there is a velocity amplitude $|U|$ dependence on the change amount of acoustic power ΔW. In addition, there also exists the temperature dependence ΔT on ΔW.

In their studies, they used the wire mesh which is made of 30 mesh stainless steel, its length is 40 mm, and the wire diameter is 0.22 mm. The porosity is 0.78. From this various quantities, hydraulic diameter and equivalent flow path diameter are calculated.

Numerical calculations are performed using equations 2.50 and 6.7, and compared with the experimental results. Following the experimental conditions, the boundary conditions for P and U in the calculation are such the temperature is the room temperature and the acoustic impedance is $(P/U)\rho_m c$. Here, c is the adiabatic sound speed and ρ_m is the density. The driving frequency is 44 Hz and the working fluid is air at 1 atm.

6.1

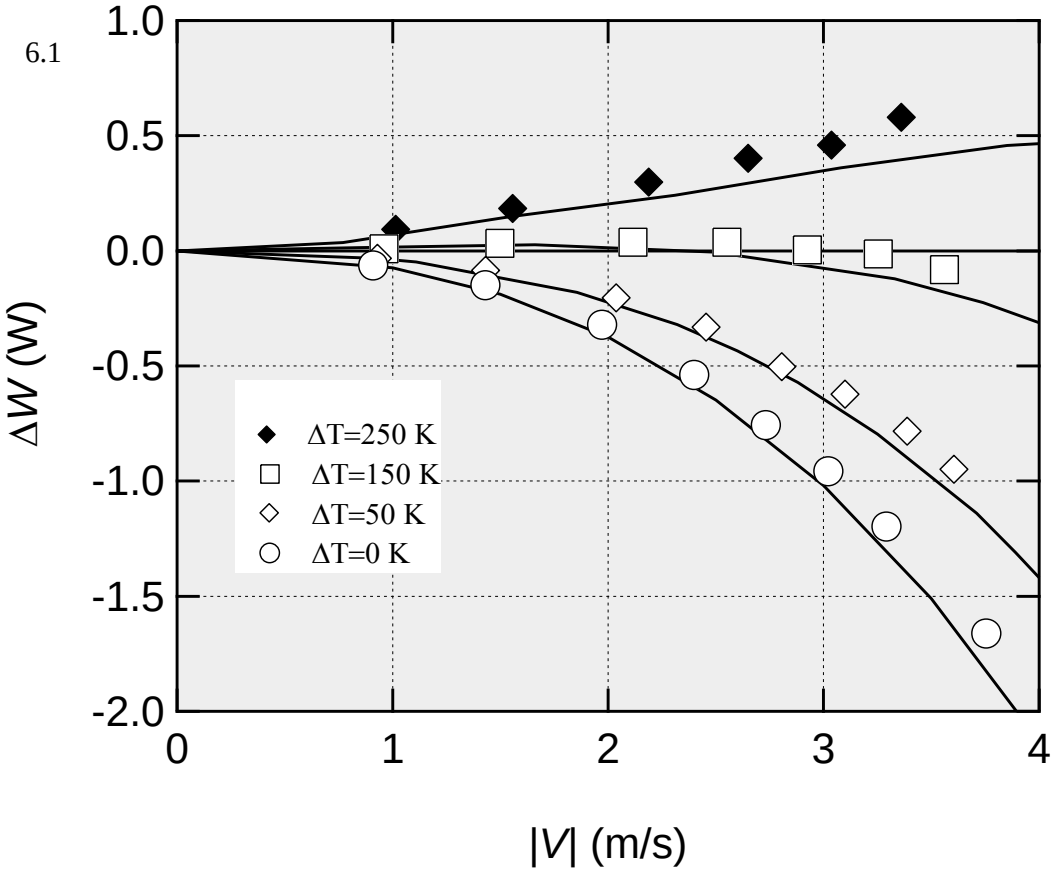

Fig. 6.1 The acoustic power gain. The difference of acoustic power at the hot and cold ends of the regenerator is shown as a function of the average velocity amplitude $|V|$. The simbols show the experimental results cap-tured from the literature 33 and the lines show the calculation results based on eqs. 2.50 and 6.7 [53, 55]

Figure 6.1 shows the experiment result of Obayasi et.al [53]. The calculation results are indicated by a solid line. The different symbols in the figure show the temperature difference ΔT. The horizontal axis shows the velocity amplitude at both ends of the regenerator. The average value $|V| = 0.5 \times (|U_H| + |U_C|)$ is taken, and on the vertical axis, the difference in acoustic power $\Delta W = W_H - W_C$ is taken. Here, the letter H and C are values at the high temperature end and the low temperature end of the regenerator, respectively. When ΔW is a positive value, the acoustic power at the high temperature side is larger and negative when it is the opposite. As can be seen from this

figure, in all temperature differences, the symbol and the solid line have a good agrement. For example, paying attention to the result when $\Delta T = 150\,K$, ΔW becomes positive when $|V|$ is small. On the other hand, ΔW becomes negative as $|V|$ increases.

6.3 Influence of complexity of flow channel on energy conversion efficiency in the stacked-screens with optimum values

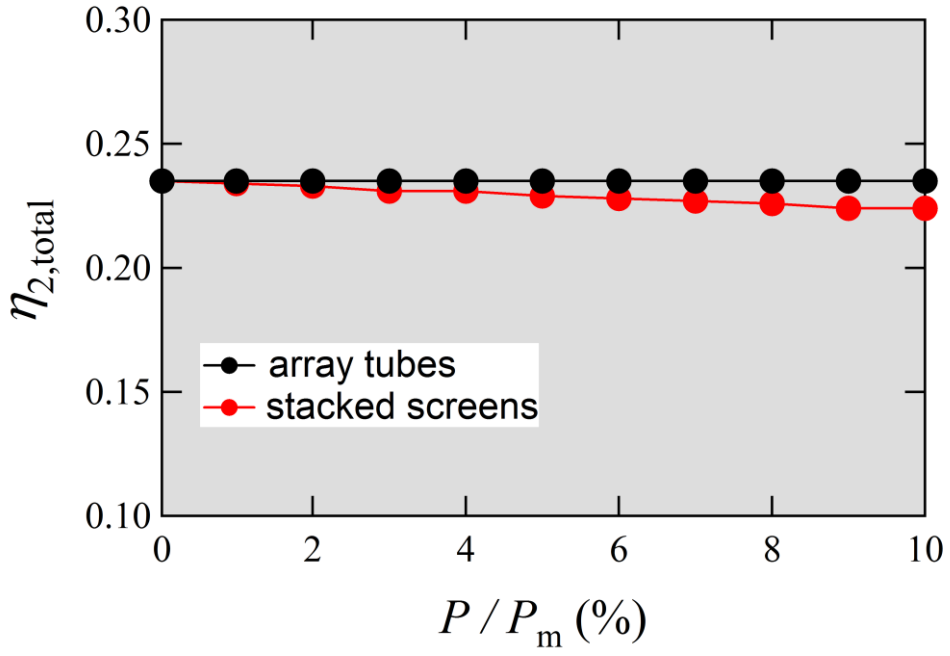

Fig. 6.2 $\eta_{2,total}$ as a function of (P/P_m)

As can be seen in figure 6.2, we compare the optimum results with the stack composed of array tubes and the stack composed of stacked-screens. Using array tubes denoted by black-circle symbols, $\eta_{2,total}$ remains constant when P/P_m is increasing. On the other hand, using the stacked-screen regenerator , $\eta_{2,total}$ decrease from 0.24 to 0.22. It indicates that using the stacked-screens the performance will be decreased.

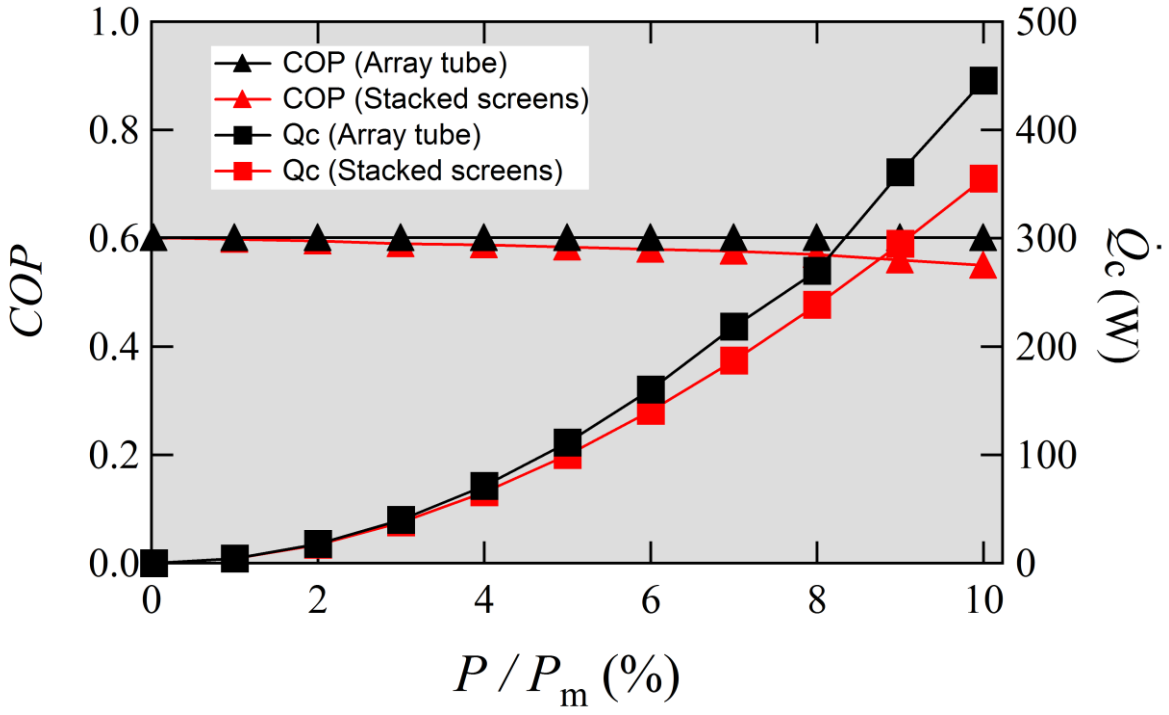

Fig. 6.3 COP and $\dot{Q}_C$ as a function of (P/P_m)

Figure 6.3 shows that using array tubes COP remains constant at 0.6 when P/P_m rises. On the other hand, using stacked screens COP drops from 0.6 to 0.55 as P/P_m increases. Moreover, Using array tubes $\dot{Q}_c$ increase when P/P_m increase. It is found that at $P/P_m = 10$ %, $\dot{Q}_c$ is 446 W. Furthermore, when stacked screens are used, $\dot{Q}_c$ is 370 W at $P/P_m = 10$ %.

6.4 Conclusion

Calculation of the energy conversion for stacked screen wire mesh using thermoacoustic theory was performed. In this calculation, we re-calculate the optimized values obtained in the previous chapter using the stacked-screens and we compare the

results with calculation using the array tubes. It was found that at P/P_m= 10 %, the performance of the total system is decreased from 0.24 to 0.22 of the upper limit value.

Chapter 7

Conclusion

The optimization of a heat-driven thermoacoustic cooler system in a looped tube with two stacks was performed. The system consists of ten components. They are ambient heat exchanger of engine, engine stack, hot heat exchanger, thermal buffer tube, wave guide 1, ambient heat exchanger, cooler stack, cold heat exchanger, thermal buffer tube 2, and wave guide 2.

After introduction of the history of thermoacoustic, we provided the thermoacoustic theory. In this study, the performance of the cooler system was calculated using transfer matrix method described in chapter 3. In chapter 3 we also make a new combination of calculation of stability limit and calculation of the performance. Therefore, the method is important to be validated. This validation was conducted in chapter 4. It was found that there is a good agreement between calculation and the experiment results. Then, using the transfer matrices, we performed the numeric calculation to calculate the optimization and performance of the system in chapter 5. Moreover, it was found that there are optimum values. Using three cycle optimization, we found that the optimum relative position of the cooler is 0.54. Furthermore, using simultaneous optimization of engine and cooler radii, the optimum radius of the engine and cooler stacks is 0.96 and 1.06, respectively. The optimum porosity of engine and cooler is 1.3. Moreover, it was also found that the total efficiency of the whole system is 0.24 of upper limit value.

Based on the above mentioned, the radii are very small. It is less than 0.3 mm. Therefore, we need to use stacked-screen wire mesh as an engine and cooler stacks. Hence, in chapter 6, we compare the stack made of array tubes and stacked-screens. It

was found that the performance of the whole system is decreased from 0.24 to 0.22.

Optimization of the heat-driven thermoacoustic cooler is important because the results revealed that the optimum values of the relative position, radii and porosities of the stacks have a huge impact on obtaining high performance. Moreover, at the present, the performance of the heat-driven thermoacoustic cooler is the best compared to that of obtained by the previous researchers.

Acknowledgements

This Thesis would not have been possible without the guidance and the support of several individuals who in one way or another contributed and extended their valuable assistance in the preparation and completion of this study.

First, I would like to express my heartiest appreciation and gratitude to my supervisor Dr. Yuki Ueda for his advices, guidance, insight, and attention.

Second, I would like to express my gratitude to Professor Atsusi Akisawa for his suggestion and kindness.

I would like to express my gratitude to Enoki Sensei, Fukushima Sensei, Nakayama Sensei, Fujiki Sensei, Ishida Sensei and Nishidate Sensei for their kindness.

I would like to express my heartiest appreciation and gratitude to Indonesian government for the financial support they gave me. I felt indebted to my country Indonesia.

I would like to express my gratitude to laboratory's members who always support me.

I also would like to express my deep gratitude to my mother, father who already passed away and family who always pray for me and encourage me to never give and become persistence.

Finally, I would like to express my gratitude to all my Indonesian friends who always help and support me.

Bibliography

[1]A. A. Putnam and W. R. Dennis, ‘‘Survey of organ pipe oscillations in systems,’’ J. Acoust. Soc. Am. **28**, 246-259 (1956).

[2]B. Higgin. ‘‘Nicholson’s Journal I,’’ Journal of Natural philosophy and Chemical art, **129**, 22- (1802).

[3]P. L. Rijke, ‘‘Notiz über eine neue art, die in einer an beiden enden offenen rohre enthaltene luft in schwingungen zu versetzen,’’ Ann. Phys. Chem. **107**, 339-343, (1859).

[4]G. Bisio and G. Rubatto, ‘‘Sondhauss and Rijke oscillations. Thermodynamic analysis, possible applications and analogies,’’ Energy, **24,** 117-131 (1999).

[5]K. T. Jr. Feldman, ‘‘Review of the literature on rijke thermoacoustic phenomena,’’ J. Sound. Vib. **7,** 83-89 (1968).

[6]C. Sondhauss, ‘‘Ueber die schallschwingungen der luft in erhitzten glasröhren und in gedeckten pfeifen von ungleicher weite,’’ Ann. Phys. Chem. **79**, 1-34 (1850).

[7]G. Kirchoff, ‘‘Ueber den einfluss der warmeileitung in einem gase auf die schallbewegung,’’ Ann. Phys. Chem. **134**, 177-193 (1868).

[8]L. Rayleigh, *The theory of sound*, (Dover, New York, 1945), 2nd ed.

[9]K.W.Taconis and J. J. M. Beenakker, ‘‘Measurements concerning the vapor-liquid equilibrium of solutions of ^3he in ^4he below 2.19 K,’’ Physica, **15**, 733-739 (1949).

[10]G. W. Swift. ‘‘Thermoacoustic engines,’’ J. Acoust. Soc. Am. **84**, 1145-1180 (1988).

[11]G. W. Swift. ‘‘Analysis and performance of a large thermoacoustic engine,’’ J. Acoust. Soc. Am. **92**, 1551-1563 (1992).

[12]P. H. Ceperley. ‘‘A pistonless stirling engine,’’ J. Acoust. Soc. Am. **66**, 1508-1513 (1979).

[13]S. Backhauss and G. W. Swift, ‘‘A thermoacoustic-Stirling heat engine: Detailed study,’’ J. Acoust. Soc. Am. **107**, 3148-3166 (2000).

[14]T. Yazaki, A. Iwata, T. Maekawa, and A. Tominaga, ‘‘Travelling wave thermoacoustic engine in a looped tube,’’ Phys. Rev. Lett. **81**, 3128-3131 (1988).

[15]T. J. Hofler, ‘‘Thermoacoustic refrigerator design and performance,’’ Ph.D. dissertation, Physics Department, University of California at San Diego, 1986.

[16] S. L. Garret, J. A. Adeff, and T. J. Hofler. ‘‘Thermoacoustic refrigerator for space applications,’’ J. of Thermophysics and Heat Transfer, **7**, 595-599 (1993).

[17]M. E. H. Tijani, J. C. H. Zeegers, and A. T. A. M de Waele, ‘‘Design of thermoacoustic refrigerators,’’ Cryogenics. **42,** 49-57 (2002).

[18]M. E. H. Tijani, J. C. H. Zeegers, and A. T. A. M de Waele, ‘‘Construction and performance of a thermoacoustic refrigerator,’’ Cryogenics. **42,** 59-66 (2002).

[19]M. Poese, R. Smith, S. Garret, and P. Gosellin, ‘‘Thermoacoustic refrigerator for ice

cream sales,'' Proc. 6th Gustav Lorentzen Conf. on Natural Working fluids, 2004.

[20]Y. Ueda, M. M. Bassem, K. Tsuji, A. Akisawa, ''Optimization of the regenerator of a travelling-wave thermoacoustic refrigerator,'' J. Appl. Phys. **107**, 034901-1-5 (2010).

[21]M. M. Bassem, Y. Ueda, A. Akisawa, ''Design and contruction of a travelling wave thermoacoustic refrigerator,'' International Journal Refrigeration. **34**, 1125-1131 (2011).

[22]J. A. Adeff and T. J. Hofler, ''Design and construction of a solar-powered, thermoacoustically driven, thermoacoustic refrigerator,'' J. Acoust. Soc. Am. **107,** 37-42 (2000).

[23]T. Yazaki, T. Biwa, and A. Tominaga, ''A pistonless stirling cooler,'' Appl. Phys. Let. **81**, un157-159 (2002).

[24]T. Jin, R. Yang, Y. Wang, Y. Feng, and K. Tang, ''Acoustic field characteristics and performance analysis of a looped travelling-wave thermoacoustic refrigerator,'' Energy Conversion and Management, **123,** 243-251 (2016).

[25]Y. Ueda, T. Biwa, U. Mizutani, and T. Yazaki, ''Experimental studies of a thermoacoustic Stirling prime mover and its application to a cooler,'' J. Acoust. Soc. Am. **115**, 1134-1141 (2004).

[26]M. Miwa, T. Sumi, T. Biwa, Y. Ueda, T. Yazaki, ''Measurement of acoustic output power in a travelling wave engine,'' Ultrasonics. **44**, 1527-1529 (2006).

[27]S. Hasegawa, T. Yamaguchi, Y. Oshinoya, ''Thermoacoustic refrigerator driven by a low temperature-differential, high-efficiency multistage thermoacoustic engine,'' Applied Thermal Engineering, **58**, 394-399 (2013).

[28]L. D. Landau and E. M. Lifshitz, *Fluid Mechanics*, (Pergamon, Oxford, 1982).

[29]N. Rott, ''Damped and thermally driven acoustic oscillations in wide and narrow tubes,'' Z angew. Math. Phys. **20**, 230 (1969).

[30]N. Rott, ''Thermally driven acoustic oscillations. Part II: stability limit for helium,'' Z angew Math. Phys. **24**, 54-73 (1973).

[31]N. Rott, ''Thermally driven acoustic oscillations. Part III: second-order heat flux,'' Z angew Math. Phys. **26**, 43-49 (1975).

[32]N. Rott, ''Thermally driven acoustic oscillations. Part iv: tubes with variable cross-section,'' Z. angew. Math. Phys. **27**, 197-224 (1976).

[33]N. Rott, ''Thermally driven acoustic oscillations. Part vi: excitation and power,'' Z. angew. Math. Phys. **34**, 609-626 (1983).

[34] G. W. Swift., *Thermoacoustics*: *A Unifying perspective for some engines and refrigerators*. (Acoustical Society of America, New York, 2002).

[35] G. W. Swift, *Springer Handbook of Acoustics: Thermoacoustic* (Springer: New York, NY, USA, 2006).

[36]A. Tominaga, ''Thermodynamic aspects of thermoacoustic theory,'' Cryogenic, **35**, 427-440

(1995)

[37] A. Tominaga, ''Thermoacoustic theory of regenerator in refrigerator,'' TEION KOGAKU, **26**, 30-36 (1990).

[38] A. Tominaga, *Fundamental thermoacoustic*, (Uchidarokakumo, Tokyo, Japan, 1998).

[39] Y. Ueda, ''Calculation method for the prediction of the performance of a travelling wave thermoacoustic cooler,'' J. Power and energy system, 2, 1276-1282 (2008).

[40]Y. Ueda, C. Kato, ''Stability analysis of thermally induced spontaneous gas oscillations in straight and looped tube,'' J. Acoust. Am. 124, 851-858 (2008).

[41]I. Farikhah, S. Ristanto, H. Idrus, U. Kaltsum, A. Faisal,''Thermoacoustic design using stem of goose down stack '', AIP Conf. Proc, 2012.

[42]G. W. Swift, D. L. Gardner, and S. A. Backhauss, ''Thermoacoustic Stirling engine'', Nature, **399**, 335-338 (1999).

[43]T**.** Biwa, Y. Tashihiro, M. Ishigaki, Y. Ueda, T. Yazaki, ''Measurements of acoustic streaming in a looped tube thermoacoustic engine with a jet pump,'' J. Appl. Phys. **101**, 093519 (2007).

[44]M. E. H. Tijani, J. C. H. Zeegers, A. T. A. M de Waele, ''The optimal Stack Spacing for Thermoacoustic Refrigeration'', J. Acoust. Soc. Am. **112**, 128-133 (2002).

[45]K. De Blok,''Multi-stage travelling wave thermoacoustic in practice,'' In The 19th International congress of sound and vibration. Vilnius, Lithuania: International Institute of Acoustics and vibration and Vilnius University; 1-8, 2012.

[46]Y. Cengel, M. A. Boles, *Thermodynamics*, (Mc Graw-Hill, New York, 2008).

[47]M. E. H Tijani, S. Spoelstra, ''A High performance thermoacoustic engine'', J. Appl. Phys.,**110**, (2011).

[48]D. L. Gardner, G. W. Swift, ''A cascade thermoacoustic engine'', J. Acoust. Soc. Am. **114 (**2003**)**.

[49]I. Farikhah, Y. Ueda, ''Numerical Calculation of the Performance of a Thermoacoustic System with Engine and Cooler Stacks in a looped tube'', Applied Sciences, **7**,672-1-14 (2017).

[50]I. Farikhah, Y. Ueda, ''The effect of the porosity of regenerators on the performance of a heat-driven thermoacoustic cooler'', ICSV24, London, 23-27 July 2017.

[51]Y. Ueda, T. Kato, and C. Kato, **''**experimental evaluation of the acoustical properties of stacked-screens regenerators**,''** J. Acoust. Soc. Am**,** 125, 780-786 (2009).

[52]M. Tanaka, ''Flow and heat transfer characteristics of Stirling-engine regenerator in oscillating flow'', Trans Japan Soc. Mech. Eng. Swr. B **55**, 2478-2485 (1989).

[53]A. Obayashi A, S. Hsu, T. Biwa, ''Amplitude dependence of thermoacoustic properties of stacked-screen wire meshes'', TEION KOGAKU, **47**, 562-567 (2012).

[54]S. Hasegawa S, Ashigaki Y, Senga M, ''Thermal diffusion effect of a regenerator with complex flow channels'', Applied Thermal Engineering, **104**, 237-242 (2016).

[55]Y. Ueda, I. Farikhah, ''Calculation of the energy conversion efficiency of a stacked-screen regenerator using thermoacoustic theory,'' TEION KOGAKU, **51**, 8, (2016).
[56]Y. Ueda, '' Method for calculating the performance of thermoacoustic devices using thermoacoustic theory'', TEION KOGAKU, **47**, 3-10 (2012).